Durham E-Theses

Simulating hydrates in shallow marine sediments

Hardwick, Jack

How to cite:

Hardwick, Jack (2018) *Simulating hydrates in shallow marine sediments*, Durham theses, Durham University. Available at Durham E-Theses Online: http://etheses.dur.ac.uk/12775/

Simulating hydrates in shallow marine sediments

Jack Spendlove Hardwick

A thesis submitted for the degree of Doctor of Philosophy

Department of Earth Sciences, Durham University

August 2018

ABSTRACT

With global energy needs growing alongside a drive to reduce carbon emissions, there is a demand for cleaner, alternative energy. Methane hydrates are one such resource that is being investigated with the goal of future potential exploitation. 99 % of this resource is found within marine environments where, particularly in shallow marine sediments, there is a concern that rising ocean temperatures may lead to widespread methane release as hydrate dissociates.

Multi-component, multi-phase (MCMP) modelling can be used to forecast the behaviour of methane hydrate dissociation in these contexts. However, there is a lack of agreement across literature on how best to numerically solve and mathematically describe the hydrate dissociation problem. The objective of this PhD is to develop new numerical models from first principles using the Method of Lines (MOL) approach. The MOL is attractive because it takes advantage of widely available high quality, ordinary differential equation solvers. However, a significant challenge is that the MOL requires formulating the problem in terms of persistent primary dependent variables.

A kinetic model was developed and used to simulate experimental data from a well-studied hydrate dissociation experiment. This study improved on previous work by reconciling more of the dataset. A three-phase permeability model was developed for this purpose, which invokes a critical threshold whereby permeability is dramatically reduced in the presence of very small hydrate saturations.

Due to numerical instability associated with upscaling the hydrate kinetics, the MOL is challenging to solve for regional scale problems using the kinetic model. An alternative model which maintains phases in equilibrium by removing the hydrate kinetics was therefore developed. Preliminary work applied this equilibrium model to a regional scale ocean warming driven hydrate dissociation problem.

Permeability in the presence of hydrate is a strong function of pore morphology as hydrate grows within porous media. Constraining this relationship can lead to better estimations of methane emissions driven by ocean warming and methane recovery in economically attractive hydrate deposits.

CONTENTS

LIST OF TABLES

LIST OF FIGURES

NOMENCLATURE

Component subscripts, *i*

h   Hydrate

m   Methane

R   Rock

s   Salt

w   Water

Phase subscripts, *j*

a   Aqueous

E   Effective

g   Gaseous

h   Hydrate

R   Rock

Dimensions

t   Time, [T]

k   index location in the direction *x*, [-]

L   Length of the domain in the *x* direction, [L]

n   Time index, [-]

r   Radial direction, [L]

R   Length of the domain in the *r* direction, [L]

x   Length direction, [L]

z   Elevation, [L]

Z   Height of the domain in the *z* direction, [L]

Latin symbols

a Advection rate. $[LT^{-1}]$. Pg. 94.

A Scaling parameter used in Ψ_P. [-]. Pg. 100.

A_{hs} Specific surface area of hydrate per particle volume. $[L^{-1}]$. Pg. 32

A_s Surface area to volume ratio of hydrate. $[L^{-1}]$. Pg. 29.

b Dispersion rate. $[L^2T^{-1}]$. Pg. 94.

B Scaling parameter used in Ψ_{zm}. [-]. Pg. 100.

C_p Specific heat capacity at constant pressure. $[L^2T^{-2}\Theta^{-1}]$. Pg. 39

C_v Specific heat capacity at constant volume. $[L^2T^{-2}\Theta^{-1}]$. Pg. 43.

E Energy per unit volume. $[ML^2T^{-2}]$. Pg. 37.

E_A Activation energy. $[L^2T^{-2}]$. Pg. 30.

F Bulk mass per unit volume. $[ML^{-3}]$. Pg. 73.

F   Mass flux. $[ML^{-2}T^{-1}]$. Pg. 22.

g   Gravity. $[LT^{-2}]$. Pg. 23.

G Mass per unit volume. $[ML^{-3}]$. Pg. 22

h_D Enthalpy of dissociation. $[L^2T^{-2}]$. Pgs. 39, 40.

h Enthalpy per unit mass. $[L^2T^{-2}]$. Pg. 39.

H Enthalpy per unit volume. $[ML^2T^{-2}]$. Pg. 38.

J   Jacobian matrix. $[LT^{-1}]$. Pgs. 50, 64.

k Bulk permeability. $[L^2]$. Pg. 24.

k_0 Permeability of the medium in the absence of hydrate, $[L^2]$. Pgs. 24, 26, 27.

k_d Dissociation rate constant. $[L^{-1}T]$. Pg. 29.

k_{d0} Intrinsic dissociation rate constant. $[L^{-1}T]$. Pg. 30.

k_{rj} Relative permeability of phase j. [-]. Pgs. 24, 27, **??**.

k_c Critical permeability. $[L^2]$. Pg. 27.

m_i Mass of component i. [M]. Pg. 103.

m_{iP} Mas of component i produced. [M]. Pg. 103.

m_{mhI} Mass of methane initially present in hydrate within the pore space. [M]. Pg. 78.

m_{whI} Mass of water initially present in hydrate within the pore space. [M]. Pg. 78.

m_{aI} Mass of liquid water initially present within the pore space. [M]. Pg. 78.

m_{gI} Mass of gas initially present within the pore space. [M]. Pg. 78.

m_{a0} Mass of water at the end of the experiment. [M]. Pg. 78.

m_{g0} Mass of gas at the end of the experiment. [M]. Pg. 78.

m_{aP} Mass of water produced by the end of the experiment. [M]. Pg. 78.

m_{gP} Mass of gas produced by the end of the experiment. [M]. Pg. 78.

m_v van-Genuchten parameter. [-]. Pg. 139.

n_v van-Genuchten paramter. [-]. Pg. 139.

$\dot{M}$ Mass source/sink. [$ML^{-3}T^{-1}$]. Pgs. 21, 29.

M_i Molar mass of component i. [-]. Pg. 29.

$\vec{n}$ Normal vector. [-]. Pg. 23.

n_j Relative permeability exponent for phase j. [-]. Pgs. 24, 27, **??**.

N_c Number of components considered. [-]. Pg. 57.

N_H Ratio of water to methane moles in a hydrate lattice. [-]. Pg. 29.

N_{PDV} Number of primary dependent variables. [-]. Pg. 64.

N_r Number of nodal points in the r direction. [-]. Pg. 76.

N_t Number of nodal points used in the top 5 m of the hydrater. [-]. 125.

N_w Number of nodal points used in the water layer below the hydrate. [-]. 125.

N_x Number of nodal points in the x direction. [-]. Pg. 76.

N_z Number of nodal points in the z direction. [-].

P Pressure. [$ML^{-1}T^{-2}$]. Pgs. 23, 29, 38.

P_0 Boundary pressure at the fluid outlet. [$ML^{-1}T^{-2}$]. Pg. 72

P_c Capillary pressure. [$ML^{-1}T^{-2}$]. Pg. 139.

P_{c0} Capillary entry pressure. [$ML^{-1}T^{-2}$]. Pg. 139.

P_e Three-phase equilibrium pressure. [$ML^{-1}T^{-2}$]. Pg. 29.

P_I Initial pressure [$ML^{-1}T^{-2}$]. Pgs. 72, 122.

P_{WD} Pressure acting at the sea floor. [$ML^{-1}T^{-2}$]. Pg. 120

$\mathbf{q}$ Darcy's flow rate. [LT^{-1}]. 22

Q Heat per unit volume. [ML^2T^{-2}]. Pg. 37.

Q_0 Heat flux from the outside the sandstone core. [ML^2T^{-3}]. Pg. 74

Q_H Basal heat flow. [MT^{-3}]. Pg. 120.

R Gas constant. [$L^{-2}T^{-2}\Theta^{-1}$]. Pg. 30.

s Entropy per unit mass. [$L^2T^{-2}\Theta^{-1}$]. Pg. 39.

S Saturation. [-]. Pg. 22.

S_{jI} Initial saturation of phase j. [-]. Pgs. 72, 122.

S_c Control surface. [L^2]. Pg. 23.

S_e Effective water saturation. [-]. Pg. 139.

S_{hc} Critical hydrate saturation. [-]. Pgs. 24, 27.

$S_j{}^*$ Effective phase saturation. [-]. Pg. 139.

S_{jr} Residual saturation of phase j. [-]. Pgs. 24, 27.

t_{rs} Thickness of a rubber sleeve. [L]. Pg. 74.

T Temperature. [Θ]. Pgs. 30, 35,38.

T_I Initial Temperature. [Θ]. Pgs. 72, 122.

T_{sf} Temperature of the sea floor. [Θ]. Pg 120.

T_0 Temperature of the air-bath. [Θ]. Pg. 72.

T_1 Temperature probe location from the outlet: 225 mm. [L]. Pg. 78.

T_2 Temperature probe location from the outlet: 150 mm. [L]. Pg. 78.

T_3 Temperature probe location from the outlet: 75 mm. [L]. Pg. 78.

U Internal energy per unit volume. [ML^2T^{-2}]. Pg. 37.

v velocity. [LT^{-1}]. Pg. 21.

V Volume. [L^3]. Pg. 21.

$\mathbf{V}$ Vector input into MATLAB's ODE solver. Pg. 64.

V_{gP} Volume of gas produced at standard conditions. [L^3]. Pg. 79.

V_{aP} Volume of water produced at standard conditions. [L^3]. Pg. 79.

V_T Total pore volume. [L^3]. Pg. 79.

W Work per unit volume. [ML^2T^{-2}]. Pg. 37.

x_{ij} mole fraction of component i in phase j. [-]. Pg. 35.

$x_{ij,ref}$ Reference mole fraction of component i in phase j. [-]. Pg. 35.

X_{ij} Mass fraction of component i in phase j. [-]. Pg. 22.

z_i Mass fraction of component i. [-]. Pg. 57.

z_{WD} Water depth. [L]. Pg. 120.

Greek symbols

α   Isothermal compressibility. $[M^{-1}LT^2]$. Pgs. 43, 101.

β   Volumetric expansivity. $[\Theta^{-1}]$. Pgs.43, 40.

γ   Convective heat transfer coefficient. $[MT^{-3}\Theta^{-1}]$. Pg.74.

Γ_w Thickness of water saturated layer beneath the hydrate reservoir. $[L]$. Pg 125.

Γ_t Thickness of the top 5 m of the hydrate saturated reservoir. $[L]$. 125.

δ   Absolute normalised component error. $[-]$. Pg.103.

Δ   Distance between two nodal points in a dimension. $[L]$. Pgs. 50, 52, 59, 125.

Δz_t Distance between the shallowest two nodal points of the hydrate. $[L]$. Pg. 125.

Δz_w Distance between the deepest two nodal points in the hydrate. $[L]$. Pg. 125.

Δz_h Discrete thickness used to discretise the hydrate saturated layer. $[L]$. Pg. 127.

$\bar{\delta}$ Mean absolute normalised component error. $[-]$. Pg.103.

ε_y RMS error of data y. $[-]$. Pg. 81.

ζ   Continuous part of mass flux. F. Pg.62.

η_t Constant used to scale Δ_{zt} through the top 5 m domain. $[-]$. 125.

η_w Constant used to scale Δ_{zw} through the water below the hydrate. $[-]$. 125.

κ   Thermal conductivity. $[MLT^{-3}\Theta^{-1}]$. Pg.38.

κ_{EI} Initial effective thermal conductivity. $[MLT^{-3}\Theta^{-1}]$. Pg.120.

κ_{rs} Thermal conductivity of a rubber sleeve. $[MLT^{-3}\Theta^{-1}]$. Pg.74.

λ_j Mobility group. $[ML^3T^{-1}]$. Pg. 24.

μ_j Dynamic viscosity. $[ML^{-1}T^{-1}]$. Pg.24.

μ_{JT} Joule-Thomson coefficient. $[M^{-1}LT^2\Theta]$. Pg.43.

∇   Parital derivative operator in 3D space. $[L^3]$. Pg. 21.

ν   Specific volume. $[M^{-1}L^2]$. Pg.39.

ρ   Density. $[ML^{-3}]$. Pg.21.

ρ_{jI} Initial phase density. $[ML^{-3}]$. Pg. 79.

ρ_{a0} Density of brine water at standard conditions. $[ML^{-3}]$. Pg.79.

ρ_{g0} Density of gas at standard conditions. $[ML^{-3}]$. Pg.79.

ρ_{sw} Density of se water. $[ML^{-3}]$. Pg. 120.

σ_{yx} Observed experimental data point x of data set y. Pg.81.

φ   Porosity. $[-]$. Pg.21.

χ   Peclét number. $[-]$. Pg. 94.

Ψ_P Smooth approximation across the equilibrium boundary. $[ML^{-1}T^{-2}]$. Pg. 100.

Ψ_{zm} Smooth approximation between hydrate limting cases. $[ML^{-1}T^{-2}]$. Pg.100.

DECLARATION

I declare that this thesis, presented for the degree of Doctor of Philosophy at Durham University, is the result of my own original research and has not been previously submitted to Durham University or any other institution.

The copyright to the material within this thesis belongs to the author and any information or quotation taken from it, should be acknowledged and published only if prior consent has been given.

Jack Hardwick

Durham University

August 2018

ACKNOWLEDGEMENTS

First and foremost, I must thank my supervisor, Prof. Simon Mathias. Thank you for giving me the opportunity to take on this challenge which has developed me immeasurably both academically and personally. Throughout this PhD, I appreciate the patience you have shown and the experience to know when to step in when I have struggled. As a mentor and a consistent source of intriguing knowledge, I could not have asked for a better supervisor. Thank you to you and your family for your hospitality over the years.

I must now thank Ines. You have been the Robin to my Batman throughout this PhD and it would be fair to say I couldn't have finished it without you. Over the past few years you have kept my head above water and pushed me to take this PhD seriously. As a friend, you have always been there, to talk with and to moan to but most crucially, be an all-round idiot with. Thanks for keeping me sane.

Further thanks must also be extended to Salim for being a good friend and always being available to ask the stupid questions it was too awkward to ask Simon. To Helena, for all our non-academic chatter over the years and the endless hypothesising of what it really means to be residually saturated, amongst other topics. Thanks to Charlotte for proof reading some of my chapters and generally being good value and also to Ayodeji, Fran and Katharine for many a good discussion. Thanks also to the friends and colleagues within the earth sciences department for the memories over the years: Pavlos, Dimitris, Bansri, Simon, Nico, Ben, Giacomo, Alex, Nuno, Ana, Valentina and Roberto. And to those outside of the department who have made the last 3 years bearable: Jamie, Dan, Lou, Sid, Finn, Pierre-Yves, Matt and everyone associated with Butler C Darts. And to Grace, who has put up with the last year with a smile and has been a real rock during my write-up, thank you.

Last but not least, I must thank my family. In particular to my Mum and Dad who, despite all the difficulties, has given me more support than you could shake a stick at. Thank you for having always provided me with the environment to pursue my goals. It would not have been possible without you.

1. INTRODUCTION

1.1   What are methane hydrates?

Gas hydrates (*gas clathrates*) are solid, crystalline compounds resembling packed ice and are composed of water and gas stable under certain thermodynamical conditions. A clathrate is defined as a substance where the lattice hosts a guest molecule. Typically, the host component is an interlocking cage of water molecules and the guest component is gas. Methane hydrates are one such gas hydrate, where the host component is water and the guest molecule is methane (Sloan & Koh, 2007).

Global need for energy continues to grow and drive the need for exploitable energy sources. Methane hydrates are one such resource expected to play an important role to meet this energy demand in the future. One m^3 of methane hydrate can hold 164 m^3 of natural gas at standard temperature and pressure conditions (0 ^oC, 0.1014 MPa) giving the compound the nickname "Fire Ice" (Kvenvolden, 1993). Methane hydrates are therefore increasingly considered as a future energy resource. Also, methane hydrates are viewed as a cleaner resource given that methane has a lower carbon content than conventional fuels such as coal (Englezos & Lee, 2005). However, methane is still a potent greenhouse gas and decomposition of methane hydrates have been theorised to play an important role in climate change events (Kennett et al., 2003).

1.2   Methane hydrate occurence
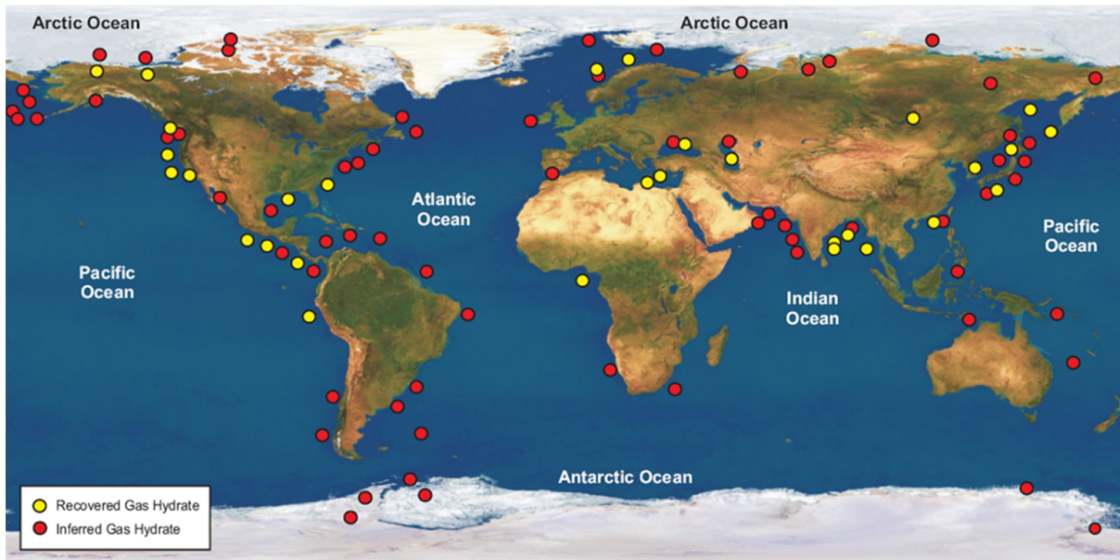
Fig. 1.1: Global distribution of recovered and inferred gas hydrates in 2008. Image taken from (Krey et al., 2009).

From the first recorded discovery by Priestley (1778), hydrates were thought of as a phenomenon only observable in laboratories and hypothesised not to naturally exist on Earth. Research into hydrates was of little significance until the 1930s when Hammerschmidt (1934) was commissioned to investigate what could be done to alleviate U.S. gas pipelines clogging up over winter and impeding distribution. He discovered that the observed ice was composed of methane hydrate and not frozen water. However, it was not until the late 1960's that research into gas hydrates accelerated, when their natural presence was first detected in an Eastern Siberian hydrocarbon field - The Messoyakha gas field (Sapir & Beniaminovich, 1973). The significance of this discovery led to a global search for gas hydrates based upon the analysis of the conditions of the Messoyakha field. It was assumed that methane hydrates could exist elsewhere in the natural world where similar pressure and temperature conditions to that observed at Messoyakha prevail (Vasilev et al., 1970; Makogon, 2010).

Methane hydrates have been recovered or inferred in numerous places around the world as illustrated in Fig. 1.1, and are understood to exist where necessary hydrate stability conditions are satisfied. These conditions include an abundance of methane and water, and favourable pressure and temperature conditions. Hydrate stability can also be affected by the presence of inhibitors and volatiles, such as salt in pore waters, and can vary considerably depending on the sedimentary framework in which the hydrate resides (Makogon, 1997; Wright et al., 1999; Sloan & Koh, 2007). Methane hydrates exist
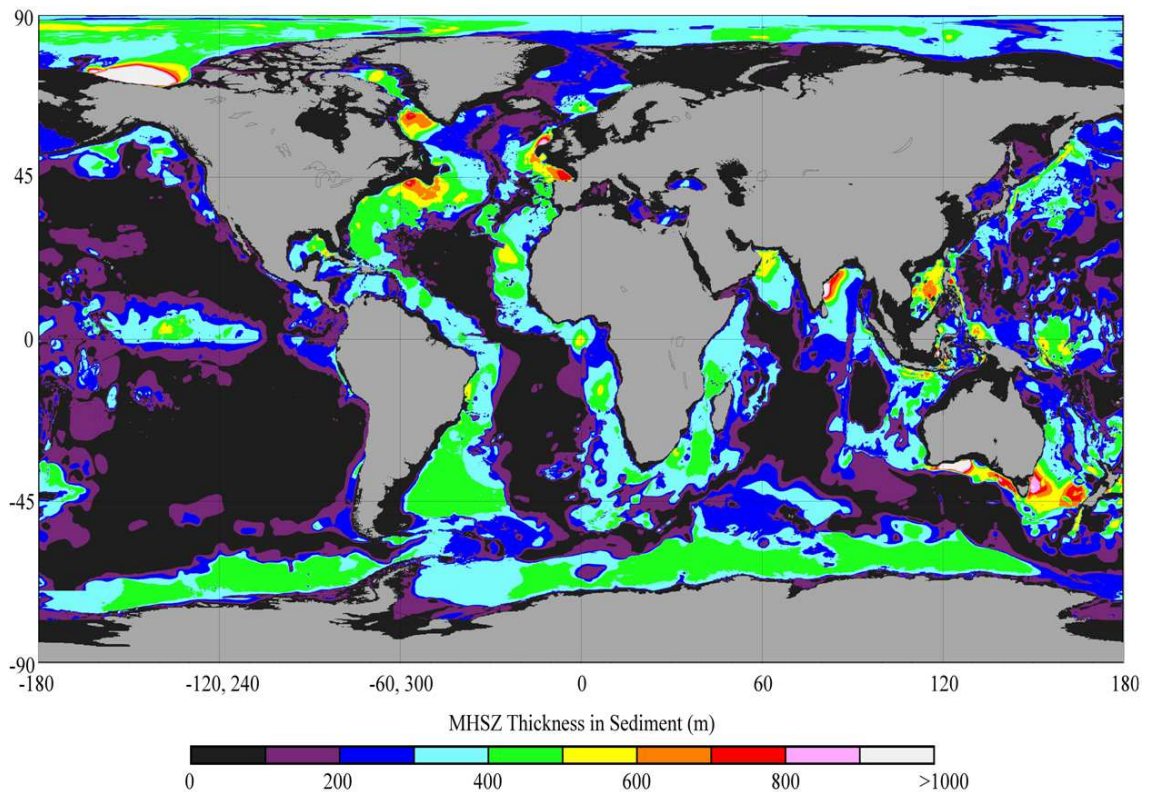
Fig. 1.2: Global distribution of gas hydrate stability zone thickness. Note that the thickest regions surround passive margins. Distribution does not disclose anything about the accumulation of hydrate as other factors such as the availability of methane, are not considered. Image taken from Krey et al. (2009).

when pressures are high, and temperatures are low, but there is a trade-off between the two. For example, hydrates are stable at shallower water depths in higher, cooler latitudes compared with temperate latitudes. The depths of favourable pressure and temperature conditions is known as the "gas hydrate stability zone" (GHSZ). Its thickness varies significantly across the globe, as shown in Figure 1.2. The top of the GHSZ is limited by the lithostatic and pore fluid pressure, geothermal gradient and if water is present, salinity. The base of the GHSZ (BGHSZ) is limited by the geothermal gradient which increases with depth. Hydrate forms within sediment void spaces and can act to significantly reduce the permeability. As such, it is common to find free gas underlying hydrate due to the inability of gas to migrate upwards (Kvenvolden, 1993; Li et al., 2017). High pressure and low temperature conditions describe the vast majority of the ocean bottoms. However, hydrate does not necessarily occupy the entire GHSZ as its occurrence is limited by the abundance of gas.

Most methane hydrate deposits are found in two major environments: (1) "permafrost-associated" methane hydrates onshore and subsea offshore towards the polar latitudes where low temperatures and thick permafrost exist; (2) marine settings where thick columns

of water stabilise hydrate. Higher saturations of methane hydrate in marine environments are found in proximity to continental margins, due in part to the high concentrations of organic carbon in these settings and fast sedimentation rates needed to accumulate and preserve the organic carbon to form a source rock (Muller & Suess, 1979). This contrasts with deep ocean accumulations beyond the continental shelf where poor organic accumulation and slow sedimentation inhibits the amount of hydrate that may form within the GHSZ.

In permafrost-associated deposits, gas hydrates are trapped in the shallow offshore and onshore sediments towards the base of the permafrost zone due to the significant weight of the overburden and a dampened geothermal gradient. Gas hydrates can form within the permafrost or beneath permafrost where gas is typically fed from an underlying thermogenic gas source (Ruppel, 2014). These deposits are understood to be formed by structural trapping of in situ water and thermogenic gas at depth undergoing a sustained change in the climate system. Glacial periods for instance would increase the overburden through formation of ice and also act to reduce the local geothermal gradient (Majorowicz et al., 2008). Permafrost-associated hydrate deposits account for less than 1 % of the global methane hydrate inventory (Ruppel, 2014). Estimates by Ruppel (2014) suggest around 20 Gt C of methane hydrates may exist in these permafrost-associated sites whereas McIver (1981) estimated closer to 11.2 Gt C. By comparison, 13.5 Gt C of greenhouse gas was emitted over the course of the year 2010 (IPCC, 2013). Permafrost-associated hydrate deposits are located around the Arctic Circle and assumed to be linked to existing hydrocarbon plays in areas such as the Arctic North America and West Siberian Basins (Dallimore & Collett, 1995; Collet et al., 2011; Ruppel, 2014).

The vast majority (around 99 %) of the global methane hydrate inventory exists in offshore marine sediments. The BGHSZ is often identified in marine sediments through a distinguishing seismic reflection marker known as a bottom simulating reflector (BSR) (Hyndman & Spence, 1992; Kvenvolden, 1993). These are laterally extensive, strong reverse polarity reflections that cross-cut sedimentary layers and represent the strong impedance contrast between the base of the hydrate and the underlying sediment or free gas zone (Hyndman & Spence, 1992). Given favourable pressure and temperature conditions, methane hydrates in marine sediments are understood to be formed directly from exsolved methane from water, provided methane is in excess of its solubility limit in water and/or at the gas-water interface (Zatsepina & Buffett, 1998). Whereas permafrost hydrates are generally associated with a thermogenic gas source, the methane in marine

natural gas hydrates is mainly derived by microbial reduction of carbon dioxide (Kvenvolden, 1995). Volatiles present in pore water, such as salt, can also affect the formation of hydrate in marine sediments whereby increasing the salinity of pore water reduces the amount of hydrate that can be formed (Husebø et al., 2009).

One well studied example of a hydrate bearing marine sediment is the mid continental slope region of the Cascadia Margin. By interpreting BSRs, wireline logs and borehole samples, this region was found to host gas hydrate at depths of between 72 and 240 metres below the sea floor. The host rocks lie within accretionary prisms and some hydrate concentrations in the interval sandy-rich layers exceed 50 % of the pore volume (Riedel et al., 2006). In contrast, the Gulf of Mexico hosts low saturation, stratigraphic gas hydrate accumulations disseminated across the broad Northern Gulf of Mexico basin subsurface (Boswell et al., 2012). Estimates of the gas hydrate in place are between 120 - 680 tcm (trillion cubic metres) of gas with approximately a third of this occurring in higher saturation sand rich layers (Klauda & Sandler, 2003; Frye, 2008; Hutchinson et al., 2011; Boswell et al., 2012).

The variability in hydrate distribution and sparse known deposits make it difficult to accurately estimate the global methane hydrate inventory. Much research has been done to constrain the global hydrate bearing gas reserves without clear convergence through time. Global estimates range from as low as 500 Gt C up to as high as 56,000 Gt C (Buffett & Archer, 2004; Milkov, 2004; Klauda & Sandler, 2005; Archer et al., 2009; Boswell & Collett, 2011; Burwicz et al., 2011; Wallmann et al., 2012; Piñero et al., 2013; Kretschmer et al., 2015).

While there is discrepancy in the global methane hydrate inventory, that there are significant reserves is a persistent viewpoint. Given this, methane hydrates have gained a lot of interest amongst industry, research and media communities alike for two reasons: (1) as an exploitable future energy resource; (2) as potentially contributing to climate change, given that methane is a greenhouse gas.

1.3   Methane hydrates as a future energy resource

The International Energy Outlook for 2016 (IEA, 2016) projects world energy consumption to increase by 48% from 2012 to 2040, with the most significant growth in non-OECD (Organisation for Economic Cooperation Development) countries. Despite the growth in renewable energy, encouraged by climate change awareness and carbon emission agreements such as the Kyoto Protocol and the Paris Climate agreement, fossil fuels are still expected to be the dominant source of energy in the 21st century (Shafiee & Topal, 2009; Mohr et al., 2015; Covert et al., 2016). Nonetheless, there is a global drive for cleaner energy alternatives but also ways to extend the life of existing conventional fields. As such, it is projected that natural gas consumption will grow from 28.3 tcm (trillion cubic metres) in 2012 to 47.9 tcm in 2040 (IEA, 2016).

Natural gas hydrate deposits that have high hydrate saturations, located in sand units of good reservoir quality, and are in proximity to existing petroleum industry infrastructure, have been targeted as an attractive energy resource that could be exploitable for natural gas (Moridis, 2008; Collet et al., 2014). However, production of methane from hydrate reservoirs is not yet widespread due to the technical difficulties and uncertainties associated with extraction. Methane production from hydrates occurs by moving the hydrate out of its stability regime and can be achieved in three main ways which are conducive to existing well-based technologies (Sloan & Koh, 2007; Ruppel, 2007; Moridis, 2008; Boswell & Collett, 2011; Collet et al., 2014). One method is to depressure the hydrate by pumping from the hydrate directly or from an underlying thermogenic gas layer. The gas produced upon dissociation can incur a natural decrease in pressure that helps develop a pressure gradient which drives the gas to the wellbore. Another method is to thermally stimulate the hydrate by injection of hot fluid or steam. The injection of fluids can also lead to hydrofracturing, which can further enhance gas flow to the wellbore. Hydrate break-up is an endothermic process and a steady transfer of heat can overcome the local temperature reduction incurred by this latent heat loss. Inhibitors, such as methanol, can also be injected to chemically destabilise the hydrate as the inhibitor competes with the methane as the guest molecule in the hydrate lattice (Sloan & Koh, 2007).

The first field to produce methane indirectly from an in situ hydrate was the Messoyakha field (Sapir & Beniaminovich, 1973). This field sits within an anticlinal trap and is overlain by a thick (420-480 m) permafrost layer. On discovery, the hydrate layer was 70-80 m thick and underlain by a free gas zone (Makogon et al., 1971). Natural gas is

extracted from this free gas zone and depressurisation of the reservoir leads the hydrate to decompose, replenishing the extracted gas. The Mallik field in Northern Canada is the first field where the depressurisation technique was successfully applied directly to the hydrate within permafrost conditions (Dallimore et al., 2005). This method was then tested for the first time in marine hydrate deposits in the Eastern Nankai Trough, located off the Pacific coast of Japan as a part of the national gas hydrate research project - MH21(Yamamoto et al., 2014). Pre-production analysis by Fuji et al. (2008) suggested that this resource may hold 1.13 tcm of methane, half of which is accommodated in units considered economically viable for extraction. After six days, hydrate had dissociated up to 25 m away from the well bore. Production was killed due to severe sand recovery and consequent back pressure build up in the reservoir. A steady gas flow of 20,000 Sm^3 (standard cubic metres), approximately 100 times that of water, was achieved (Yamamoto et al., 2014). The relatively warm reservoir temperatures helped to inhibit hydrate reformation that may occur due to the latent heat loss when hydrate decomposes.

1.4   Methane hydrates and climate change

While carbon dioxide is broadly perceived as the prevalent greenhouse gas, the Intergovernmental Panel on Climate Change (IPCC) claims that methane is about 25 times more potent than carbon dioxide as a greenhouse gas over a century on a per unit mass basis (IPCC, 2013). IPCC (2013) assessed the global methane budget and estimated the total sources to be 678 Tg yr^{-1}. Of that, 331 Tg yr^{-1} were from anthropogenic sources. The remaining 347 Tg yr^{-1} were from natural sources, with wetlands the most dominant source (217 Tg yr^{-1}) and hydrates-associated sources estimated at a mere 7 Tg yr^{-1}. However, bubble flux analysis by Shakova et al. (2014) showed that approximately 17 Tg yr^{-1} of methane is released to the atmosphere annually from the East Siberian Arctic Shelf alone. While this discovery is not representative of global methane emissions from hydrate sources it may suggest that IPCC (2013) underestimated its significance. It is also feared that the contribution to this budget due to methane hydrate decomposition may increase as a response to increasing surface and ocean temperatures. Furthermore, gas hydrate decomposition has been associated with paleoclimate change.

The study of past major hydrate dissociation events and their interaction with paleoclimate change may provide a comparison for the anthropogenic led climate change expected for the 21st century and beyond. One such analogous paleoclimatic event that has been widely discussed occurred during the late Neoproterozoic ($\sim$ 1000 to 541 Ma), post-Snowball Earth glaciation which brought ice to low latitudes (Hoffman et al., 1998; Sohl et al., 1999). Warming following the Marinoan glaciation event ($\sim$ 635 Ma) is thought to have been sped up by the release of methane from both permafrost and marine hydrates (Jiang et al., 2006; Kennedy et al., 2008; Shields, 2008). Bjerrum & Canfield (2011) investigated a more recent climate event ($\sim$ 551 Ma) thought to have led to widespread methane release by hydrate destabilisation under an anoxic ocean. Such events may have instigated the climate conditions for the Cambrian explosion (Kennedy et al., 2008).

Another event, the Palaeocene-Eocene Thermal Maximum (PETM) ($\sim$ 55.5 Ma) was a period of sudden warming that increased temperatures by 5 ^{o}C (Zachos et al., 2007). Coring records of the PETM boundary show a significant (2.5-5 %) negative excursion in marine $\delta^{13}C$, indicative of increases in atmospheric and ocean carbon concentration (McCarren et al., 2008). While there are several explanations as to its occurrence, widespread methane hydrate release proposed by Dickens et al. (1995) is the most prominent. However, the triggering mechanism needed for upwards of 10^3 Gt C to be released across

short geological time-scales remains unclear (Dickens et al., 1997; Thomas et al., 2002; Dickens, 2011). Recent analysis by Frierling et al. (2016) indicates that initial warming and dissociation of hydrate occurred 10 kyr prior to the PETM and gas hydrate decomposition acted as a positive carbon cycle feedback. However, mathematical modelling work suggests that methane release from hydrates under ocean warming for various PETM scenarios is low and delayed by 100 kyrs (Minshull et al., 2016). Zeebe et al. (2016) constrained the release rate of Carbon to be ≤ 1.1 Pg yr^{-1} during the PETM from carbon isotope data. Interestingly, this value is within the range of modern seafloor methane release rates (0.016-3.2 Pg yr^{-1}), suggesting the present day seafloor regime is analogous to the PETM (Ruppel and Kessler, 2017).

The concerns surrounding the relationship between methane hydrate and climate change can be best summarised when considering the widely debated "Clathrate Gun Hypothesis" (Kennett et al., 2003). This hypothesis proposes that late Quaternary (~ 2.58 Ma to present) climate change was in part driven by periodic release of methane from hydrate, as follows. Increases in surface and intermediate water temperatures during glacial periods, called Dansgaard-Oeschger (D/O) events, caused methane hydrate to destabilise and flux methane to the atmosphere in the process. The methane hydrate reservoir is then thought to have re-equilibrated and reaccumulated during cyclical Quaternary stadial (colder) periods. Methane, as previously mentioned, is a potent greenhouse gas and would act to warm the Earth further, leading to continued dissociation of hydrate. In the extreme case, this positive feedback process could continue in perpetuity until all the hydrate is dissociated or re-stabilised by cooling periods or sufficient sea level increase. Such a process would lead to dramatic global warming across geologically short timescales. Large negative $\delta^{13}C$ excursions in benthic and planktonic foraminifera found at the Southern California Margin, Gulf of California, Amazon Fan and East Greenland are evidence of an increased atmospheric methane concentration during the late Quaternary. Such observations in ice core data correlated with the beginning of D/O episodes and at the terminations of glacial and stadial events. However, more recent research through hydrogen isotope analysis of the Greenland ice cores suggested at least two of these D/O events are instead attributed to wetlands (Bock et al., 2010). Similar conclusions have been found by correlating the Greenland ice core records of light deuterium (associated with wetland release) and heavy deuterium (associated with deep ocean release) methane in the Pleistocene-Holocene (Sowers, 2006) and during the Younger Dryas event (Petrenko et al., 2009). The Clathrate Gun Hypothesis also propounds that widespread

submarine failure, as is well recorded in Quaternary core data by turbidite deposits, could be the efficient transport mechanism required for large volumes of methane to reach the atmosphere at these D/O events and such a mechanism has been postulated elsewhere by some researchers (Nixon & Grozic, 2007; Bangs et al., 2010; Crutchley et al., 2016). However, for the Quaternary period in question, Maslin et al. (2004) suggested that submarine slope failure instead coincided with Heinrich events and not D/O events. Heinrich events are depositions of coarse grained terrigenous sediment attributed to iceberg break-off and rafting before melting and depositing their load (Heinrich, 1988). Although it is realistic to think that methane hydrate dissociation has played a role in shaping the Earth's past climate, it is uncertain how methane release by hydrate dissociation is likely to affect present day climate as surface temperatures continue to rise.

1.5 Why are we interested in shallow marine sediments?

While much of the global methane hydrate inventory is found within oceanic gas hydrate-bearing sediments, most concern, in the context of climate change, has been directed toward hydrate deposits of the upper continental slopes and rises (Riedel et al., 2006; Thatcher et al., 2013; Marín-Moreno et al., 2013; Berndt et al., 2014; Skarke et al., 2014; Weinstein et al., 2016; Stranne et al., 2016a). In these regions, concentrated methane hydrate vanishes upslope as the top of the GHSZ moves out of the stability region (Ruppel and Kessler, 2017). These regions are under scrutiny because their shallow water depths make hydrates in these environments more susceptible to climate change. Ruppel (2011) estimated that $\sim$ 3.5 % of the global gas hydrate inventory (based on an inventory of 1800 Gt C) may be prone to climate change on a centuries scale with some upper continental margins interpreted at a less than century scale (Thatcher et al., 2013). Given the broad range of estimates for the global methane hydrate inventory, there may be significantly more than 63 Gt C (Ruppel, 2011) susceptible to modern climate change.

The characteristics of shallow marine regions only act to draw further attention for this reason. For instance, as thermal diffusion of surface temperature changes takes time to be felt by the marine hydrate reservoirs (Thatcher et al., 2013; Minshull et al., 2016), hydrate deposits on the continental slopes would have comparatively shorter delays compared to deep marine hydrate settings. In fact, such metastable hydrate deposits are continually undergoing dissociation and reformation as a response to Earth's natural cycles on tidal to Milankovitch scales (Ruppel and Kessler, 2017).

When considering release of methane from marine sediments into the atmosphere, there is a tendency to underestimate the significance of potential sinks that may inhibit methane flux to the surface. In particular the so-called "sulphate reduction zone" (SRZ), which is a thin zone of intense anaerobic oxidation of methane (Borowski et al., 1997; Boetius & Wenzhöfer, 2013). The efficiency of this biofilter to consume methane fluxing through it varies considerably depending on the methane flux rate with estimates between 20 and 80 % for fast and slow regimes respectively (Boetius & Wenzhöfer, 2013).

Despite methane's low solubility in sea water, the concentrations of methane in most ocean waters are low enough that methane bubbles rising through the water column diffuse rapidly and are replaced by oxygen and nitrogen (Vielstädte et al., 2015). Methane bubbles with bigger diameters may prevent all of this methane being stripped away, however, increasingly larger bubbles are required with greater water depth to prevent complete

oxidation (Chen et al., 2014). Environments like shallow slopes of continental shelves have higher methane flux rates due to the increased organic concentration found at these margins and shallower water columns between the seep point and the sea surface. These regions are where methane emissions would most likely be able to bypass much of these potential sinks and reach the surface (Boetius & Wenzhöfer, 2013).

This said, one of the fundamental controls on methane release rates for any methane hydrate reservoir is that of the hydrate-bearing porous media (Stranne et al., 2016a,b; Ruppel and Kessler, 2017). For instance, low reservoir permeability will impede the ability for gas to flow away from the hydrate, sometimes preventing migration altogether (Reagan & Moridis, 2008, 2009; Stranne et al., 2016b). Grain size distribution can also affect hydrate stability, where smaller pores are less likely to be sites for hydrate growth than larger pores (Uchida et al., 2002; Turner et al., 2005). Sediment properties such as thermal conductivity and specific heat capacity influence heat flow through the porous media and therefore the dissociation rate. Many investigations ignore the effect of the endothermic heat loss which occurs during dissociation when attempting to quantify methane release rates (Biastoch et al., 2011). However, not constraining this process within sediment may lead to an overestimation of release rates (Ruppel and Kessler, 2017). Consequently, before researchers consider the amount of methane produced by hydrate saturated reservoirs or reaches the oceans and atmosphere driven by climate change, the dynamics between hydrate-associated phases and the host sediment must be adequately assessed. This interaction ultimately determines whether methane will be released or not and at what rate.

1.6 Investigative approaches to the hydrate dissociation problem

A number of approaches are used by researchers to investigate the mechanics behind methane release rates from hydrate dissociation in porous media. One method is to form or dissociate hydrate samples under experimental conditions and interpret the data. Some experiments aim to retrieve whole data sets from the hydrate dissociation process (Yousif et al., 1991; Masuda et al., 1999; Kneafsey et al., 2007; Mekala et al., 2014; Wang et al., 2016), whilst others focus on particular aspects such as permeability (Ahn et al., 2005; Jaiswal et al., 2009; Johnson et al., 2011; Kneafsey et al., 2011; Konno et al., 2013, 2015), stability conditions (Dickens & Quinby-Hunt, 1994; Wright et al., 1999; Uchida et al., 2002; Turner et al., 2005), endothermic heat loss (Anderson, 2004; Gupta et al., 2008) or the intrinsic mechanics behind dissociation (Englezos et al., 1987; Kim et al., 1987; Clarke & Bishnoi, 2001a,b). Due to the difficulty in bringing samples to the surface without dissociating them, many researchers use synthetic samples developed in a laboratory.

Collecting data is time-consuming and expensive, therefore a large proportion of researchers use mathematical models to corroborate the limited experimental observations. Modelling can be undertaken in two distinct ways: analytical and numerical modelling. Analytical models are mathematical models where the changes in the system are characterised wholly by closed-form mathematical equations and provide exact solutions. This approach has been used for the hydrate dissociation problem (Ji et al., 2001; Goel et al., 2001; Tsypkin, 2007; Ahmadi et al., 2007; Li et al., 2015). Problematically, analytical models often require overly simplifying assumptions to the problem to be solved exactly. Complex problems that cannot be solved analytically must instead be solved numerically. Numerical modelling uses approximations of the problem to provide an approximate solution. In transient systems, each variable in the numerical model has a value with a time and space co-ordinate. Transient numerical modelling is widely used to investigate the hydrate dissociation problem at both laboratory (Masuda et al., 1999; Sun & Mohanty, 2006; Nazridoust & Ahmadi, 2007; Gamwo & Liu, 2010; Liang et al., 2010; Ruan et al., 2012a,b; Zhao et al., 2012a,b; Shin, 2014; Chen et al., 2016, 2017; Hardwick & Mathias, 2017) and regional scales (Xu et al., 2001; Reagan & Moridis, 2008, 2009; Kurihara et al., 2010; Anderson et al., 2011; Biastoch et al., 2011; Reagan et al., 2011; Hunter et al., 2013; Thatcher et al., 2013; Marín-Moreno et al., 2013, 2015a,b; Kretschmer et al., 2015; Stranne et al., 2016a,b). Despite numerous publications, few models can fully comprehend multiple facets of the hydrate dissociation process. In a regional setting, there is

significant uncertainty surrounding estimating the volume of hydrate in place, handling the methane sinks such as the SRZ and general reservoir properties such as permeability (Ruppel and Kessler, 2017).

Failure to incorporate the effect of hydrate on porous media processes such as relative permeability and endothermic heat loss can lead to overestimations of methane release due to climate driven dissociation of several hundred percent (Stranne et al., 2016b). Furthermore, despite significant uncertainty in sediment properties, a number of studies use the same parameterisation as one another for reservoir controls, including relative permeability, across different study areas (Reagan et al., 2011; Thatcher et al., 2013; Marín-Moreno et al., 2015a,b; Stranne et al., 2016a,b).

A suite of commercial and open source numerical codes are available that can handle MCMP mass and energy transfer in porous media in conjunction with hydrate dissociation. Some examples include FLUENT (Nazridoust & Ahmadi, 2007), MH-21 (Fuji et al., 2008), HydrateResSim (Gamwo & Liu, 2010) and TOUGH+HYDRATE (T+H) (Moridis, 2012). T+H builds on the original TOUGH2 code for fluid, heat and mass transfer in porous media by including processes related to hydrate (Pruess et al., 1999). This code is widely used for numerical modelling by researchers investigating hydrate dissociation at both the core and regional scale (Kowalsky & Moridis, 2007; Reagan et al., 2011; Thatcher et al., 2013; Marín-Moreno et al., 2013; Birkedal et al., 2014; Marín-Moreno et al., 2015a,b; Stranne et al., 2016a). The model provides users with a broad choice of inputs for all aspects of the hydrate dissociation problem. However, through literature there appears to be a lack of consensus on how to constrain certain processes related to hydrate dissociation. Alternatively, some researchers, particularly at the core scale, choose to develop MCMP models from first principles (Sun & Mohanty, 2006; Gamwo & Liu, 2010; Liang et al., 2010; Ruan et al., 2012b; Chen et al., 2016; Hardwick & Mathias, 2017). The benefit of this is that through building the model, the user can develop a deeper understanding of the mechanics behind hydrate dissociation in porous media. Furthermore, this can lead to greater experimentation with mathematical descriptions of the hydrate dissociation processes and allow the user to give more attention to the dominating functions and less to those which seem to have a minor influence on the results, thus streamlining the model.

The treatment of time in MCMP numerical models comes down to deciding whether to use an explicit or an implicit time-stepping scheme. These schemes can be found by expanding out a Taylor series for an incremental time-step, Δt [T], around a function,

$f(t)$, to a desired order of accuracy. Explicit schemes step forward in time and although they are simpler to implement, they can end up being computationally expensive due to necessarily very small time-steps required to ensure numerical stability. Implicit schemes use information ahead of the current time and on the contrary are unconditionally stable with time but are more challenging to solve and for first order approaches, more diffusive with larger time-steps (Goudarzi et al., 2016). Implicit schemes solve by applying an inverse matrix. This matrix is found by linearising the governing equations, often by determining the Jacobian matrix. Furthermore, non-linear problems such as the hydrate dissociation problem are also more computationally expensive by virtue of the fact that they must be solved iteratively.

A popular approach for the MCMP hydrate dissociation problem, employed by T+ H, is to employ a 1st order accurate implicit time-stepping scheme in conjunction with a Newton-Raphson root finding algorithm used to iteratively find the Jacobian matrix (Sun & Mohanty, 2006; Gamwo & Liu, 2010; Moridis, 2012). This algorithm makes successively improved guesses of the solution by reducing the time step to solve the conservation statement until the difference between the $(n+1)^{\text{th}}$ and n^{th} iteration is within an acceptable tolerance. Other approaches such as semi-implicit IMPES schemes, whereby pressure is implicitly solved but mass concentration is explicitly solved, have also been employed (Liang et al., 2010; Zhao et al., 2012a).

Alternatively, multi-step, multi-order schemes have been presented before for MCMP problems (Mallison et al., 2005; Mathias et al., 2014; Goudarzi et al., 2016). Here, error propagation is controlled by comparing solutions of different orders (Shampine & Reichelt, 1997). Only Hardwick & Mathias (2017) have utilised such higher order schemes in the context of hydrate dissociation. Mass and energy conservation statements for MCMP problems are typically formulated as a set of partial differential equations (PDEs). MATLAB contains a built in suite of solvers that use multi-step multi-order schemes to solve ordinary differential equations (ODEs) (Shampine et al., 2003). In order to utilise these ODE solvers it is necessary to convert the PDEs into a set of ODEs. One way this is done is through the Method of Lines (MOL) approach which approximates the spatial derivatives but not the temporal derivative (Schiesser, 2012). The MOL has recently been applied to a number of problems (Wouwer et al., 2005; Haq et al., 2012; Mathias et al., 2014; Goudarzi et al., 2016; Hardwick & Mathias, 2017). Haq et al. (2012) performed numerical simulation of the Burger's equation using a meshless method of lines approach and a 4th order Runge-Kutta scheme to integrate their ODEs. Alternatively, Wouwer et

al. (2005), Mathias et al. (2014) and Goudarzi et al. (2016) applied the method of lines using MATLAB's suite of ODE solvers - namely ode15s, which uses a 5th order version of the backwards differentiation formula. Mathias et al. (2014) and Goudarzi et al. (2016) have utilised the MOL previously for MCMP problems to great effect. In this study, MATLAB's ODE15s is also used but differs from the previous studies in two key ways. Firstly, through the selection of the primary dependent variables (PDVs) from which all variables in the system are dependent upon and secondly, the spatial derivatives apply a first order Godunov upwinding scheme. Greater detail surrounding application of the MOL approach and utilising MATLAB's ODE solvers can be found in Chapter 3.

1.7   Objectives

The main objectives of this project are to:

- Develop a Method of Lines formulation for the hydrate dissociation problem.

- Investigate the dynamics behind the hydrate dissociation problem and the controls on methane release rates.

- Forecast methane release rates as a response to climate change for hydrate-bearing shallow marine sediments.

1.8   Structure of the thesis

In Chapter 2, the mathematical equations to describe the different processes associated with MCMP hydrate dissociation problem are presented. This chapter first outlines the mass conservation statement. Next, the conservation of momentum is discussed with a focus on permeability. Following on from this, a kinetic hydrate dissociation theory is introduced. The energy conservation statement is then derived including the latent heat loss term. Finally, a methodology for obtaining the relevant thermophysical properties for water, methane and hydrate are presented.

Chapter 3 develops and presents the numerical solution scheme employed. The Method of Lines approach is explained. Numerical integration is discussed with the aim to utilise MATLAB's ODE solvers. This section also discusses the phenomenon of numerical stiffness. Numerical stiffness occurs in a coupled set of ODEs where one part of the solution can be solved quickly while another part is solved much slower and can lead to error and computational inefficiency. Following on from this, a methodology to reformulate the mass and energy conservation statements in terms of primary dependent variables which are persistent throughout the simulation is then described. This is a necesary requirement to use the ODE solvers. The chapter then goes on to explain how the spatial derivatives are approximated using finite differences with discontinuities, handled using Godunov's 1st order upwinding scheme.

Chapter 4 presents a set of numerical simulations for the hydrate dissociation core-scale experiment of Masuda et al. (1999). The problem is treated as 2D radially symmetric. The numerical model is calibrated to the experimental data using three unknown parameters. Two parameters control the relative flow of gas and water. The core sits

within a constant temperature air-bath such that another parameter controlling this rate of heat transfer is also used for calibration. The resulting calibrated parameters are then used as forecasts for the remainnig runs of the experiment. Comparisons between 1D and 2D modelling are also made.

The kinetic model is too difficult to numerically solve at regional scales. Therefore, in Chapter 5, an alternative equilibrium model is developed and compared to the kinetic model under scenarios based on the experimental work discussed in Chapter 4.

Chapter 6 summarises the findings in this study. Chapter 6 also includes preliminary regional scale modelling where the equilibrium model developed in Chapter 5 is used to estimate ocean warming induced methane release rates from shallow marine sediments. Conditions for this regional scale model are taken from literature of the West Svalbard area but with parameterisaion taken from the model calibration to Masuda's experimental data (described in Chapter 4). Modelling studies for the West Svalbard area from the literature are used for initial comparisons (Reagan et al., 2011; Thatcher et al., 2013; Marín-Moreno et al., 2013). Finally, recommendations for further work are discussed.

2. GOVERNING EQUATIONS

2.1   Objective

- Outline the thermodynamic conceptual model and the assumptions used in this study.

- Compare and contrast existing mathematical functions used to describe the hydrate dissociation process.

- Present the thermophysical properties used in this study.

2.2   Highlights

- The mass, momentum and energy conservation statements are outlined in the context of hydrate dissociation.

- A new permeability model, the so-called "Critical Threshold" model, is introduced based upon the work in Chapter 4.

- An energy conservation statement in terms of pressure and temperature is derived.

- The Clapeyron equation is used to derive a thermodynamical expression handling the latent heat loss on dissociation.

2.3   Introduction

When representing real world problems mathematically, it is important to recognise that while all dynamics of the system should be considered to occur concurrently, individual processes of the problem can at first be independently assessed. Such processes described by mathematical functions are typically coupled together through a set of conservation statements to be solved. Mass, momentum and energy are such classical conservation statements so named because, for an isolated system or a system in equilibrium with its surroundings, these measurable quantities do not change as the system evolves with time. Instead, these quantities are redistributed within the system, and in the case of energy and momentum, may change form. This chapter will outline these conservation statements in the context of the hydrate dissociation problem. Parameterisations are discussed with reference to literature.

A number of assumptions are made throughout this thesis. Capillary pressure is not included. During core scale modelling in Chapter 4 it was found that incorporating capillary pressure through the widely used van-Genuchten model (van Genuchten, 1980) had no impact on the simulation results (see Appendix A). The regional scale model in Section 6.1 is built upon the core scale model in Chapter 4 and therefore, for simplicity, the formulation for the regional scale model presented in Chapter 5 also ignores capillary pressure. As methane solubility in sea water is very low (Wiesenburg & Guinasso, 1979) and following Masuda et al. (1999), Nazridoust & Ahmadi (2007), Liang et al. (2010), Ruan et al. (2012b) and Chen et al. (2016, 2017), it is assumed that methane in a mobile state can only occupy the gas phase. Salinity becomes diluted as hydrate dissociates and produces fresh water therefore salt is assumed never to precipitate, remaining always in the aqueous phase. Ice is considered not to form. Materials are assumed isotropic. The rock medium is assumed to be static and rigid and unable to dissolve into the pore fluids.

The following subscripts for components (i) and phases (j) are used: Methane, water, hydrate, salt and rock components are represented by the subscripts m, w, h, s and R respectively; Gaseous, aqueous, hydrate and rock phases are represented by the subscripts g, a, h and R respectively.

2.4 Conservation of mass

The fundamental concept of mass conservation implies that: *mass can neither be created nor destroyed*. Therefore, the total mass at any point of time is the same unless mass is added to or taken from the system:

$$\text{Final Mass} = \text{Original Mass} + \text{Mass Added} - \text{Mass Removed} \tag{2.1}$$

Subsequently, it must be said that

$$\text{Rate of Change of Mass} = \text{Net Flux of Mass} \tag{2.2}$$

Consider the flow of mass through a control volume:

$$\frac{\partial}{\partial t} \int_V \rho dV = - \int_V \nabla \cdot (\rho v) dV \tag{2.3}$$

where t [T] is time, V [L^3] is volume, ρ [ML^{-3}] is density and v [LT^{-1}] is velocity. ∇ is the gradient operator in 3D space, here given as

$$\nabla = \frac{\partial}{\partial x} + \frac{\partial}{\partial y} + \frac{\partial}{\partial z} \tag{2.4}$$

Assuming a fixed control volume leads to

$$\int_v \left(\frac{\partial \rho}{\partial t} + \nabla \cdot (\rho v) \right) dV = 0 \tag{2.5}$$

For any constant control volume, it is therefore universally said that

$$\frac{\partial \rho}{\partial t} + \nabla \cdot (\rho v) = 0 \tag{2.6}$$

where mass is added to or taken from the system, a mass source/sink rate term per unit volume, $\dot{M}$ [MT^{-1}], is included, where $\dot{M} < 0$ would be a removal of mass and $\dot{M} > 0$ is a generation of mass.

$$\frac{\partial \rho}{\partial t} = -\nabla \cdot (\rho v) + \dot{M} \tag{2.7}$$

Consider a rock medium with porosity ϕ [-], where porosity is defined as the volume fraction of void space of the total rock volume. The porosity is filled at all times with material where S_j [-] is the volume fraction of pore-space occupied by material phase j,

hereafter referred to as the saturation of phase j.

$$\sum_j S_j = 1, \qquad j = g, a, h \tag{2.8}$$

The mass of phase j per unit volume of rock, G_j [ML^{-3}], can be found from

$$G_j = \phi \rho_j S_j \tag{2.9}$$

Invoking a system where components can transfer between phases, the mass of component i per unit volume, G_i [ML^{-3}], will follow as the proportionate mass per unit volume across all available phases comprised of that component as follows:

$$G_i = \sum_j \phi X_{ij} \rho_j S_j, \qquad j = g, a, h \tag{2.10}$$

and

$$\sum_j X_{ij} = 1, \qquad j = g, a, h \tag{2.11}$$

where X_{ij} [-] is the mass fraction of component i in phase j. Taking $\boldsymbol{v}_j$ [LT^{-1}] to be the velocity of phase j, mass flux of component i, $\mathbf{F}_i$ [ML^{-2}T^{-1}], can be taken as

$$\mathbf{F}_i = \sum_j \phi X_{ij} \rho_j S_j \boldsymbol{v}_j, \qquad j = g, a \tag{2.12}$$

Phase flow occurs in bulk and only within the porous network and can be related to Darcy's flow rate of phase j, $\mathbf{q}_j$ [LT^{-1}], by

$$\boldsymbol{v}_j = \frac{\mathbf{q}_j}{\phi S_j}, \qquad j = g, a \tag{2.13}$$

so that

$$\mathbf{F}_i = \sum_i X_{ij} \rho_j \mathbf{q}_j, \qquad j = g, a \tag{2.14}$$

From Eqs. (2.7), (2.10) and (2.14), the mass conservation statement within porous media for a multi-component, multi-phase system can be written as

$$\frac{\partial G_i}{\partial t} = -\nabla \cdot \mathbf{F}_i + \dot{M}_i \tag{2.15}$$

2.5   Conservation of momentum

The fundamental statement of the conservation of momentum is an extension of Newton's third law of motion and states that: *Every action has an equal and opposite reaction.* When two objects collide, momentum is conserved as one object will lose the momentum that the other object will gain. Considering the actions that transfer momentum, it can be said that

$$\text{Rate of Change of Momentum} = \text{Flux of Momentum} + \text{Body Forces} + \text{Surface Forces} \tag{2.16}$$

Body forces are forces that act on the fluid within the control volume, such as the force acting on the fluid under gravitational acceleration, $\mathbf{g}$ [LT^{-2}] (= 9.81 ms^{-2}). Surface forces exert a normal force on the control surface that encloses the control volume, such as pressure, P [$ML^{-1}T^{-2}$] and deformation where $\mathbf{D}$ [T^{-1}] is the deformation tensor.

Momentum per unit volume is given as mass per unit volume multiplied by velocity: ρv. Taking the flux of momentum entering the control volume as +*ve* and occurring normal, $\overrightarrow{n}$ [-], to the control surface, S_c [L^2], the relevant conservation of momentum takes the following integral form (Tryggvason, 2011):

$$\frac{\partial}{\partial t} \int_V \rho v dV = -\underbrace{\oiint_{S_c} \overrightarrow{n} \cdot (\rho v^2) dS_c}_{\text{Flux of Momentum}} + \underbrace{\int_V \rho \mathbf{g} dV}_{\text{Body Forces}} + \underbrace{\oiint_{S_c} \overrightarrow{n} \cdot (P - 2\mu\mathbf{D}) dS_c}_{\text{Surface Forces}} \tag{2.17}$$

Where μ [$ML^{-1}T^{-1}$] is the dynamic viscosity. The application of the divergence theorem leads to

$$\frac{\partial(\rho v)}{\partial t} = -\nabla \cdot (\rho v^2) + \nabla \cdot (P - 2\mu\mathbf{D}) + \rho \mathbf{g} \tag{2.18}$$

While it is possible to solve a set of momentum conservation equations for phase velocity as above, the solution of the resulting Navier-Stokes equations for the detailed velocity distributions would be unnecessarily complicated. Instead, an averaged version of the momentum equation can be used to calculate the fluid velocity that takes the form of Darcy's law. Taking an average of the surface forces over the control volume leads to the capillary forces in the air-water-hydrate system to cancel out such that stress tensors can be ignored. Darcy's law is appropriate in the context of laminar flow in porous media due to the low fluid velocities realised of which the square of the velocity becomes negligible. Darcy's law also assumes that the local fluid velocity is proportional to the pressure

gradient. Flow of more than one phase is always assumed to be similarly related to the pressure gradient (Orr, 2007). Assuming that capillary pressure is negligible, the Darcy's flow rate of phase j, $\mathbf{q}_j$, is given by

$$\mathbf{q}_j = -\lambda_j(\nabla P + \rho_j \mathbf{g}), \qquad j = g, a \tag{2.19}$$

where λ_j is a term representing the mobility of phase j given as

$$\lambda_j = \frac{k k_{rj}}{\mu_j}, \qquad j = g, a \tag{2.20}$$

k [L^2] is the permeability of the rock flushed with a single fluid phase, k_{rj} [-] is the relative permeability of phase j, μ_j [ML^{-1}T^{-1}] is the dynamic viscosity of phase j and P_j [ML^{-1}T^{-2}] is the pressure of phase j. Note that $\mathbf{q}_h = 0$ as hydrate is treated as a static phase. Greater velocities can not be described adequately by Darcy's law as inertial effects will become more important. In this case, the Forchheimer equation would be better (Bear, 2018). In this study, fluid velocities within pore volumes are expected to be low due to the relatively low velocities associated with ambient fluid movement in porous media.

2.5.1 Relative permeability

Permeability is a measure of the ability of a porous medium to transmit fluids through its porous network. Relative permeability is defined as the proportional consumption of permeability by a phase with respect to the total permeability of the rock. Increasing the permeability of the rock and/or the relative permeability of a mobile phase leads to greater phase mobility (see Eq. (2.20)). Consequently, handling relative permeability in porous media saturated with hydrate is a major consideration for the hydrate dissociation problem. For consistency with terminology, literature commonly refers to single phase flow in a medium saturated by hydrate relative to the medium absent of hydrate (also referred to as the intrinsic permeability, k) as relative permeability (Daigle, 2016). Many experiments have investigated how relative permeability reduces with increasing hydrate saturation and it is generally accepted that the variation in relative permeability is largely attributed to the hydrate morphology (Buffet & Zatsepina, 2000; Kleinberg et al., 2003; Waite et al., 2004; Ahn et al., 2005; Spangenberg et al., 2005; Minagawa et al., 2009; Kerkar et al., 2009; Jaiswal et al., 2009; Priest et al., 2009; Kumar et al., 2010; Kneafsey
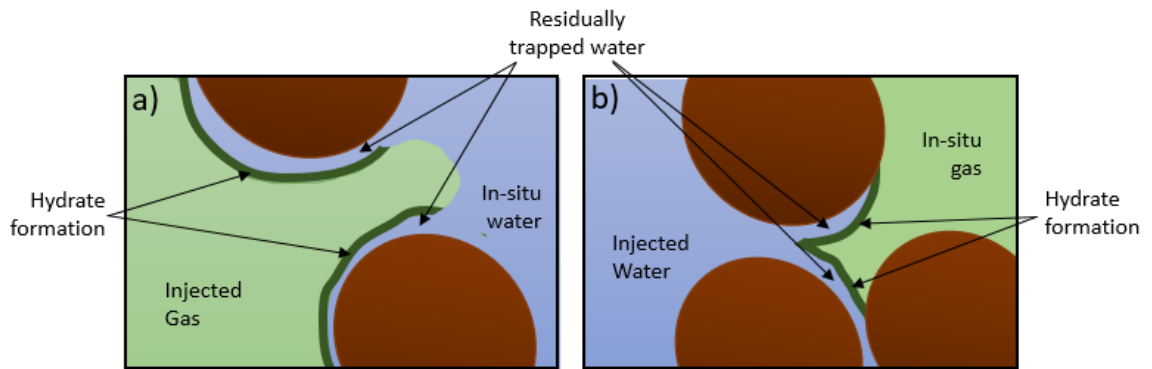
Fig. 2.1: Schematics of the two main ways that hydrate will grow within porous media. (a) Hydrate exhibiting grain coating behaviour as wetting behaviour forces hydrate to form at the sites of residually trapped water in contact with the injected gas. (b) Hydrate exhibiting pore-filling behaviour as the imbibing water, by flow through the residual pathways, surrounds and eventually isolates the in-situ gas in the centre of the pores.

et al., 2011; Johnson et al., 2011; Li et al., 2018).

It has been observed that the sites for hydrate growth in porous media varies depending upon the abundance of the hydrate forming components, the phase each component is in and capillary effects associated with interfacial tension (Clennell et al., 1999; Delli & Grozic, 2013). Hydrate growth is generally observed either within the centre of the pores or as a coating around the surface of the rock grains. When hydrate is formed by injecting gas into water, it grows around the grains and within the pore throats, cementing the grains together (Waite et al., 2004; Minagawa et al., 2009; Priest et al., 2009). In contrast, when hydrate is formed by injecting water into gas, water (as the wetting phase) preferentially migrates close to the grains and hydrate forms around the accumulated gas in the centre of the pores (Kleinberg et al., 2003; Spangenberg et al., 2005; Priest et al., 2009; Kneafsey et al., 2011). Furthermore, forming hydrate directly from water with dissolved gas also exhibits pore-filling behaviour and although higher saturations can be grown, the growth rate is slower (Buffet & Zatsepina, 2000; Spangenberg et al., 2005; Kerkar et al., 2009; Li et al., 2018). At regional scales, a hydrate saturated reservoir with heterogeneous porosity and permeability would likely exhibit pore filling and grain coating behaviour concurrently.

There are a range of mathematical approaches to handling permeability reduction due to hydrate formation. One widely used approach was interpreted from experimental observations and subsequent modelling of hydrate dissociation within a Berea sandstone core by Masuda et al. (1999). In an attempt to reconcile the observed slow pressure decline at the opposing end of the core with respect to the outlet with a quick gas production, they

employed a power-law relationship. The so-called "University of Tokyo" model relates permeability to the pore geometry as follows :

$$k_{rj} = \frac{k_j}{k} = (1 - S_h)^N, \qquad j = g, a \qquad (2.21)$$

where k_j [L^2] is the effective permeability of the phase in the presence of hydrate and N [-] is a permeability reduction exponent. In the model by Masuda et al. (1999) a value of $N = 15$ was used. However, while Masuda et al. (1999) were able to sustain the pressure decline in the core, the simulated gas production was significantly delayed compared to the experimental data (see Fig. 7 of Masuda et al. (1999)). Nonetheless, many subsequent publications have used this function to calibrate experimental permeability data or in multi-phase flow simulations. The exponent N varies significantly from as low as 3 to as high as 38 but without a clear distinction as to whether pore filling (or grain coating) is best characterised by lower or higher values for N (Masuda et al., 1999; Minagawa et al., 2009; Kumar et al., 2010; Liang et al., 2010, 2011; Ruan et al., 2012a,b; Konno et al., 2013; Li et al., 2013).

Alternatively, Daigle (2016) assumed that hydrate growth follows a fractal pattern whereby hydrate will preferentially form in the largest available pores first. Considering hydrate formation in this way removes the need to understand whether hydrate was formed in an imbibing or draining environment because the site of hydrate formation and by extension, the effect on permeability, is interpreted as solely dependent upon the pore size distribution and therefore the same in either scenario. The concept of a critical threshold was also introduced, where, beyond a critical hydrate saturation, permeability drops to zero and flow terminates. Daigle (2016) reasoned that as there exists an irreducible saturation for mobile phases, at which there is no flow for saturations below the irreducible saturation, conversely there must exist an upper limit for hydrate. Through calibration, Daigle (2016) was able to simulate several relative permeability curves with his model.

However, it is important to recognise here that all the relative permeability studies mentioned which use the University of Tokyo model and the data sets used by Daigle (2016) considers just one mobile phase. Indeed, there is limited three-phase relative permeability data, in a hydrate context, that can be utilised (Ahn et al., 2005; Jaiswal et al., 2009; Johnson et al., 2011).

A three-phase relative permeability model that is widely used for regional scale MCMP modelling is the so-called "modified version of Stone's first three-phase relative perme-

ability" model or "Modified Stone" model (Stone, 1970; Moridis, 2012). This particular model is popular when using the open source numerical code, TOUGH+HYDRATE, for regional scale modelling. Following Moridis (2012), it can be expressed as follows:

$$k_{rg} = \max\left[0, \min\left(\left[\frac{S_g - S_{gc}}{1 - S_{ar}}\right]^{n_g}, 1\right)\right] \tag{2.22}$$

and

$$k_{ra} = \max\left[0, \min\left(\left[\frac{S_a - S_{ar}}{1 - S_{ar}}\right]^{n_a}, 1\right)\right]$$

S_{gc} [-] is a critical gas saturation, S_{ar} [-] is a residual aqueous saturation and n_g [-], n_a [-] are relative permeability exponents for the gas and aqueous phase respectively. Hydrate is accounted for given that $\sum_j S_j = 1$.

An alternative three phase relative permeability model was derived in this study to reconcile the fast gas production with the slow pressure decline in the aforementioned experiment by Masuda et al. (1999) (see Fig. 7 of Masuda et al. (1999)) This was a necessary requirement to adequately simulate the set of experiments which forms the basis of much of the work in Chapter 4. Incorporating the ideas discussed by Daigle (2016) with the so-called Corey curves (Corey, 1954), this model can be described mathematically by

$$k_{ra} = k_{rf}\left(\frac{S_a - S_{ar}}{1 - S_{ar} - S_{gc}}\right)^{n_a}, \qquad S_{ar} \le S_a \le 1 - S_{gc} \tag{2.23}$$

$$k_{rg} = k_{rf}\left(\frac{S_g - S_{gc}}{1 - S_{ar} - S_{gc}}\right)^{n_g}, \qquad S_{gc} \le S_g \le 1 - S_{ar}$$

$$kk_{rf} = \begin{cases} k_c, & S_h > S_{hc} \\ k_c + (k - k_c)\left(\frac{S_{hc} - S_h}{S_{hc}}\right), & 0 \le S_h \le S_{hc} \end{cases}$$

where k_{rf} [-] is the total relative permeability available to the fluid phases such that it could be said that $k_{rh} = 1 - k_{rf}$. S_{hc} [-] is a critical hydrate saturation, beyond which the permeability is reduced to a value of k_c [L^2]. This model assumes that even a small amount of hydrate can have a significant effect on the permeability provided it is grown in a particular location, such as within a pore throat crucial to the connectivity of the permeable network. With this in mind, ideally, S_{hc} should be set to zero. However, it is found that stable numerical simulation requires $S_{hc} > 0$. A value of $S_{hc} = 10^{-4}$ is found to be sufficiently small so as not to significantly affect simulation results. The reduced permeability, k_c, is assumed to be 100 times less than k_0 in order to emphasise the sudden
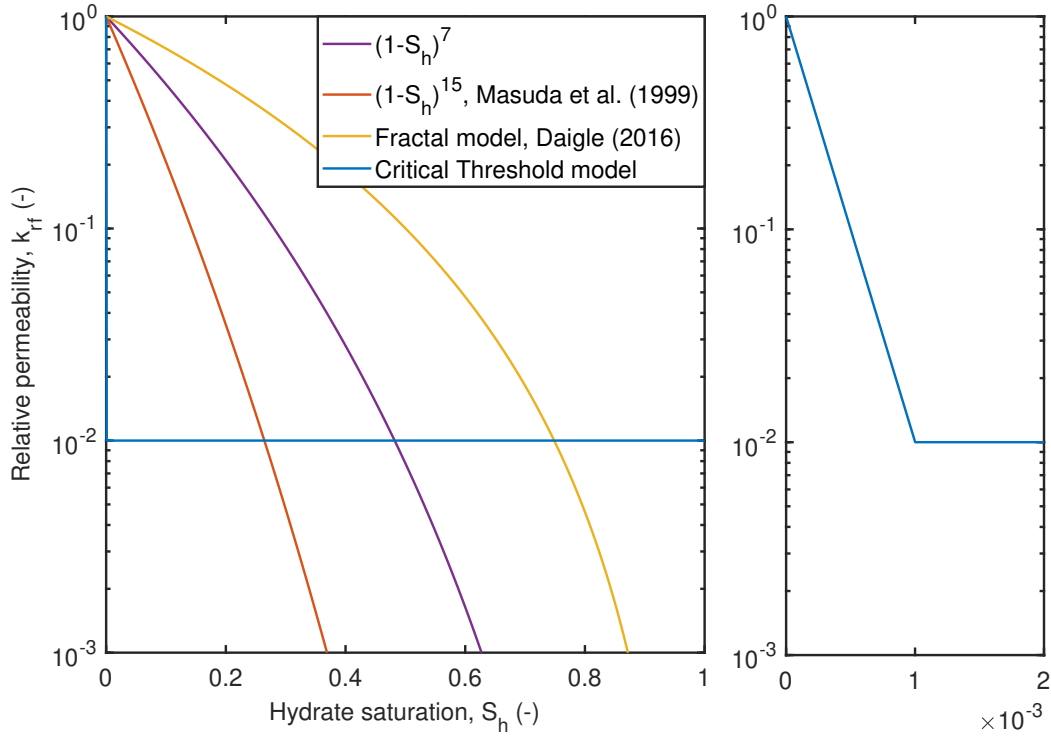
Fig. 2.2: Comparison between relative permeability models for a single mobile phase in the presence of hydrate. (a) Comparison between the Critical Threshold model in Eq. (2.23), the University of Tokyo model for $N = 7$ and $N = 15$ (Masuda et al., 1999) and the Fractal model (Daigle, 2016). (b) The critical point in the Critical Threshold model.

release of methane as hydrate is completely removed from the pore throats.

Herein, this proposed model is referred to as the "Critical Threshold" model. A comparison is made in Fig. 2.2 between the Critical Threshold model to the previously discussed two phase relative permeability models. From Fig. 2.2, there is a distinctive difference in functional form between the Critical Threshold model and the University of Tokyo and Fractal models. The University of Tokyo model which uses $N = 15$ has a significantly lower relative permeability response than the Fractal or University of Tokyo model using $N = 7$ for a given hydrate saturation. Both the Fractal model and University of Tokyo model when $N = 7$ were applied to two-phase relative permeability data and are therefore not applicable to this study where a three-phase relative permeability model is required. Masuda et al. (1999) applied the University of Tokyo model using $N = 15$ alongside a typical two-phase relative permeability function, however was inadequate at simulating multiple facets of their experiment (see Figs. 3-8 of Masuda et al. (1999)). The Critical Threshold model was developed by considering the data in the Masuda experiment directly and is therefore most relevant to this study.

2.6 Kinetic dissociation theory

To understand how methane is produced from hydrates, it is necessary to understand the intrinsic dissociation process. A relevant kinetic model proposed by Kim et al. (1987) conjectures that the production of methane from hydrate follows a two-step process: (1) destruction of the hydrate host lattice at the solid surface of a particle; (2) desorption of the methane molecule from the solid surface. The hydrate is assumed invariant in composition and the dissociation process is assumed proportional to a driving force, $(f_g - f_e)$ $[ML^{-1}T^{-2}]$, which represents the difference between the fugacity of methane gas at the three-phase-equilibrium boundary and the fugacity of methane gas at the solid hydrate surface. The above ideas can be written mathematically as follows:

$$\dot{M}_m = -M_m k_d A_s (f_g - f_e) \tag{2.24}$$

where M_m [-] is the molar mass of methane, k_d $[L^{-1}T]$ is the dissociation rate constant and A_s $[L^{-1}]$ is the surface area to volume ratio of hydrate. Given that fugacity is a partial pressure, it is common to approximate $f_g - f_e$ as being equal to $P_g - P_e$. As capillary pressure is not included, P_g is in turn replaced with pressure, P.

Hydrate formation and dissociation can be represented by the following reaction equation (Sloan & Koh, 2007):

$$CH_4 \text{ (gas)} + N_H H_2 O \text{ (water or ice)} \Longleftrightarrow CH_4 + N_H H_2 O \text{ (hydrate)} \tag{2.25}$$
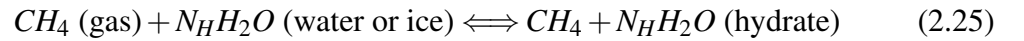
where N_H[-] is the number of molecules of water per methane molecule in the hydrate lattice, known as the hydration number. Consequently, from Eq. (2.24) it can be said that the production rate of water is given by

$$\dot{M}_w = \frac{\dot{M}_m}{M_m} N_H M_w \tag{2.26}$$

where M_w [-] is the molar mass of water. The dissociation of hydrate can then be expressed as

$$\dot{M}_h = -\frac{\dot{M}_m}{M_m} M_h \tag{2.27}$$

where M_h [-] is the molar mass of hydrate. Given that $\mathbf{F}_h = 0$, the mass conservation

statement from Eq. (2.15) for hydrate reduces to

$$\frac{\partial G_h}{\partial t} = \dot{M}_h \qquad (2.28)$$

Considering the reaction equation for formation/dissociation of methane hydrate in Eq. (2.25), the kinetic model covers the disequilibrium pathway between a hydrate in stable equilibrium, to a gas and water system in equilibrium absent of hydrate. An alternative approach to the kinetic model is to always maintain components in equilibrium which is discussed further in Chapter 5.

2.6.1   Reaction rate constant for hydrate dissociation

A reaction rate constant describes the rate of a reaction when the concentration of each reactant is taken as unity. Each reaction has a definitive value of the rate constant at a fixed temperature. How the reaction rate varies with temperature can generally be represented by the Arrhenius equation as follows:

$$k_d = k_{d0} \exp\left(\frac{-E_A}{RT}\right) \qquad (2.29)$$

where k_{d0} [L^{-1}T] is an intrinsic reaction rate constant, E_A [L^{2}T^{-2}] is the activation energy required to initiate the reaction, R [L^{-2}T$^{-2}\Theta^{-1}$] (=8.314 J K^{-1} mol $^{-1}$) is the gas constant and T [Θ] is temperature. Depending on the lattice structure and composition of the hydrate, k_{d0} and E_A may vary. Structure I and II hydrates are the only two stable structures with a single guest molecule of methane (Sloan & Koh, 2007). Kim et al. (1987) determined k_{d0} to be 12.4×10^4 mol m^{-2}Pa^{-1} s^{-1} and E_A to be 78 kJ mol^{-1} for structure I hydrate and 99.999 % pure methane, assuming each particle was of the same diameter. Clarke & Bishnoi (2001b) improved on the parameters from Kim et al. (1987) by incorporating particle size distribution to better estimate the particle surface area available for reaction and determined a k_{d0} of 3.6×10^4 mol m^{-2}Pa^{-1} s^{-1} and an E_A of 81 kJ mol^{-1} in significant contrast to Kim et al. (1987) as shown in Fig. 2.3. For this study, the values given by Clarke & Bishnoi (2001b) are used.
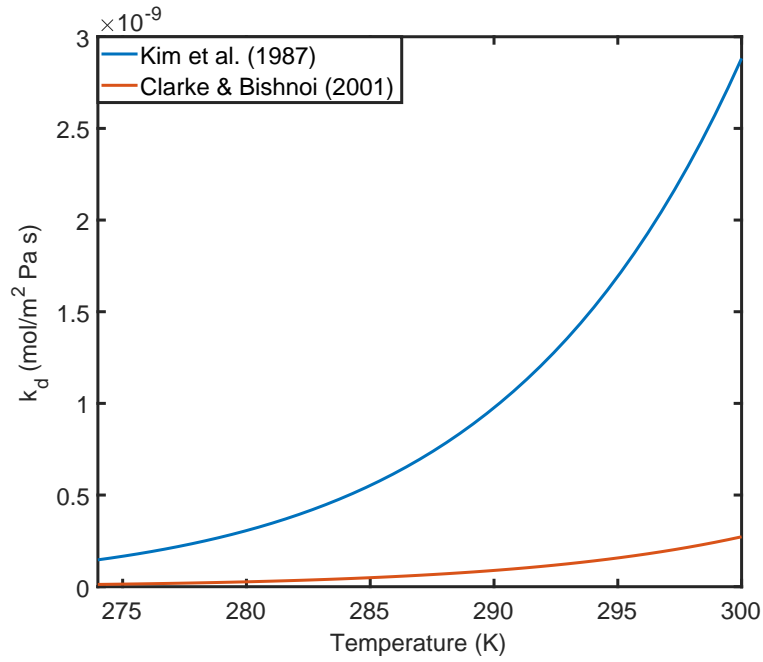
Fig. 2.3: A comparison of the dissociation rate for Structure I hydrate.

2.6.2 Reaction surface area of hydrates

Methane is released at the surface of hydrate. The surface area to volume ratio of hydrate available to dissociation, A_s [L^{-1}], is an important consideration in the dissociation process. Nakayama et al. (2007) performed numerical simulations against experiments to produce an empirical expression relating A_s to particle radius, porosity and hydrate saturation. By matching to gas production and temperature data from a core scale experiment, Kumar et al. (2013) suggested that the surface area of hydrate would vary according to the initial hydrate saturation and introduced a shape coefficient dependent on saturation and porosity. Both approaches introduce additional degrees of freedom to calibrate their data. A Kozeny-Carman model has also been used to determine A_s (Yousif et al., 1991; Sun et al., 2005; Sun & Mohanty, 2006; Liang et al., 2010; Zhao et al., 2012b) such that it can be said that:

$$A_s = \sqrt{\frac{\phi_E{}^3}{2k}} \tag{2.30}$$

where ϕ_E [-] is an effective porosity defined as the porosity available to mobile fluids in the presence of hydrate. A number of researchers combine the Kozeny-Carman model with the permeability function shown in Eq. (2.21) (Sun & Mohanty, 2006; Liang et al., 2010; Zhao et al., 2012b). Increasing N will cause A_s to increase by several orders of magnitude with hydrate saturation as depicted in Fig. 2.4. Taking a different approach could better describe how the surface area of hydrate available to dissociation evolves with
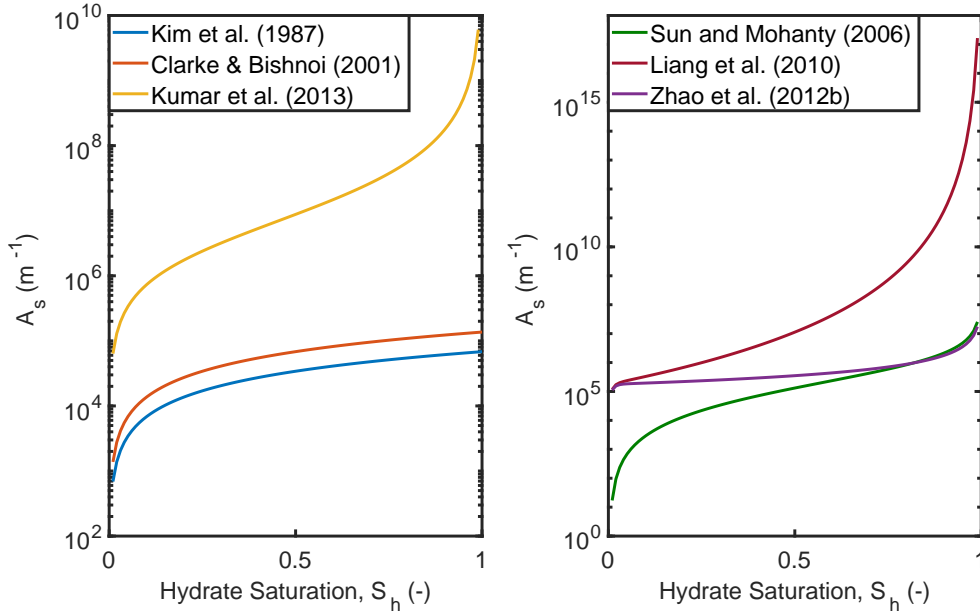
Fig. 2.4: Comparisons of the surface area to volume ratio of hydrate available to dissociation, A_s. Kim et al. (1987): $A_{hs} = 3.75 \ \mu\text{m}^{-1}$ in Eq. (2.31); Clarke & Bishnoi (2001b): $A_{hs} = 7.5 \ \mu\text{m}^{-1}$ in Eq. (2.31); Kumar et al. (2013): applies a shape coefficient of 250 and $A_{hs} = 7.5 \ \mu\text{m}^{-1}$; Sun & Mohanty (2006): permeability, k, uses the kozeny-carmen power-law model from Civan (2001) and A_s in Eq. (2.30); (Liang et al., 2010): $N = 15$ in Eq. (2.21) and A_s in Eq. (2.30); (Zhao et al., 2012b): $N = 5$ in Eq. (2.21) and A_s in Eq. (2.30)

hydrate saturation. One theory which assumes that hydrate forms within the pore space lets A_s behave non-monotonically such that at very low and very high hydrate saturations, A_s becomes smaller. Alternatively, if hydrate forms around the grain surfaces at very low hydrate saturations, it could lead A_s to be large, whereas for high saturations, A_s would be small. Given the discussion in Section 2.5.1, associating relative permeability with hydrate formation morphology, it could suggest that the surface area to volume ratio of hydrate available to dissociation is also a function of hydrate morphology.

Without experimentation it cannot be concluded which model is most appropriate and as such a simpler approach is preferred. Following the holistic experimental work on hydrate dissociation by Kim et al. (1987), by assuming a uniform saturation of hydrate within a pore volume of porous media, A_s can be represented by

$$A_s = \phi S_h A_{hs} \tag{2.31}$$

Kim et al. (1987) calculated that the specific surface area of hydrate per particle volume, A_{hs} [L^{-1}], equated to 3.75 μm^{-1} for a constant hydrate particle diameter of 16 μm. Clarke & Bishnoi (2001b) incorporated particle size distribution and improved the estimated mean diameter to 8 μm and therefore $A_{hs} = 7.5 \ \mu\text{m}^{-1}$ is used in this study.

2.6.3 Three-phase equilibrium pressure

Consider a system where solid, liquid and gaseous phases co-exist. An equilibrium between these phases can exist when there are no unbalanced potentials. A system in equilibrium experiences no changes when it is isolated from its surroundings (Cengel & Boles, 2002). For phases to exist in equilibrium, they must be in thermal, mechanical, chemical and phase equilibrium. "Thermal equilibrium" implies the temperature is the same throughout the system. "Mechanical equilibrium" is when there are no changes in potential in the system. "Phase equilibrium" suggests the components dispersed between the phases are at an equilibrium level and do not change. "Chemical equilibrium" suggests that there is no change in chemical composition and no reactions are occurring. It therefore follows that thermodynamics may describe the relationship between pressure, temperature and state of a system in equilibrium but also the deviation of the system from equilibrium through work done (Cengel & Boles, 2002). Methane hydrates can reach a state of equilibrium when they exist under the appropriate pressure and temperature regimes. The equilibrium pressure is the pressure, at a given temperature, at which methane, water and hydrate can theoretically co-exist in phase and chemical equilibrium.

Handa & Stupin (1992) first noted that the three-phase equilibrium pressure of hydrates may depend on the water activity, where water activity can be considered as the amount of water available to hydrate a material. In this context, a water activity of unity means that all water is available for hydration whereas a water activity of zero means no water is available for hydration. In a gas-water-hydrate system, water is the wetting phase. In smaller pores, such as is in silts and clays, the water activity can be reduced due to the capillary effects of the grains such as interfacial tension (Clennell et al., 1999). Uchida et al. (2002) experimented on the relationship between water activity and hydrate stability over a large range of pore sizes and showed that for a given temperature, the equilibrium pressure is higher for smaller pores. For pore radii greater than 600 Å (angstroms), the effect of pore size on hydrate stability becomes negligible (Turner et al., 2005). This difference between the effect on hydrate stability in large and small pore radii is illustrated by Wright et al. (1999) who compared the calculated three-phase equilibrium curves for sands and silts as shown in Fig. 2.5. In the kinetic model, as described in the previous subsections, the driving force for dissociation is given as $(P - P_e)$ where P is pressure and P_e is the three-phase equilibrium pressure. Researchers tend to fit empirical relationships to experimental data to describe P_e in terms of temperature for a fixed composition (Dick-
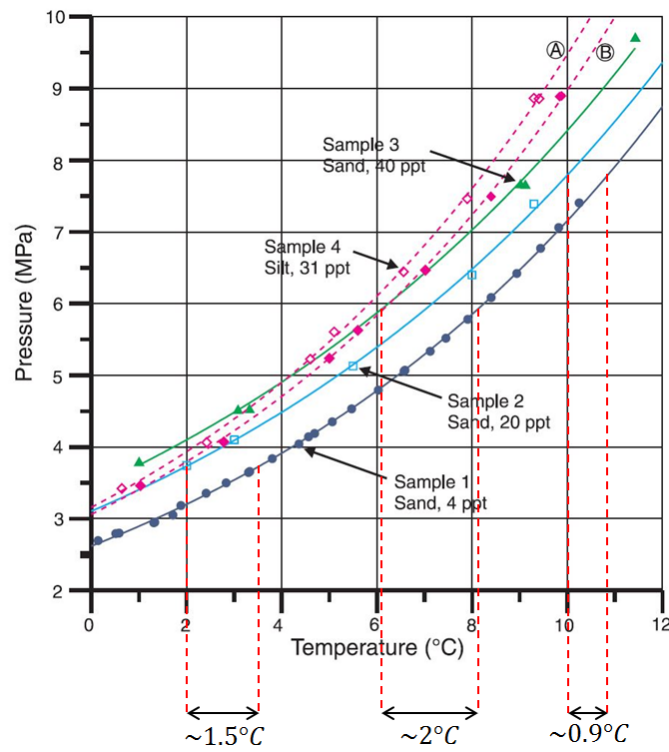
Fig. 2.5: The effect of pore-size (fine (silts) vs coarse (sands)) on three-phase equilibrium pressure. Graph adapted from Wright et al. (1999). Also illustrated is how $T_{d,ref}$ can vary under different pressures for a given salinity (Section 2.6.3.1)
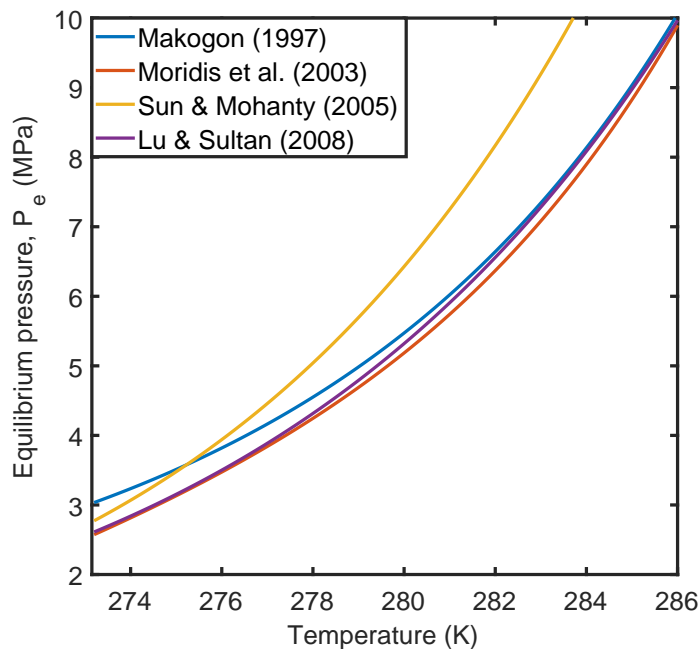
Fig. 2.6: Comparisons between different empirical three-phase equilibrium functions. Variation is likely due to the porous media used, however, the approximation taken by Sun & Mohanty (2006) contrasts significantly to the other expressions.

ens & Quinby-Hunt, 1994; Makogon, 1997; Wright et al., 1999; Moridis, 2003; Sun et al., 2005; Lu & Sultan, 2008). Some relevant empirical equations are compared in Fig. 2.6. For this study, it was found that the most appropriate mathematical expression for P_e

was due to Moridis (2003):

$$P_e = \sum_{n=0}^{5} a_n T^n \qquad (2.32)$$

where P_e is in MPa, T is in K and:

$$
\begin{aligned}
a_0 &= -1.94138504464560 \times 10^5 & a_1 &= 3.31018213397926 \times 10^3 \\
a_2 &= -2.25540264493806 \times 10^1 & a_3 &= 7.67559117787059 \times 10^{-2} \\
a_4 &= -1.30465829788791 \times 10^{-4} & a_5 &= 8.86065316687571 \times 10^{-8}
\end{aligned}
\qquad (2.33)
$$

2.6.3.1 Effect of salt on hydrate stability

Solutes including salts such as sodium chloride can have a significant effect on the thermodynamic stability of methane hydrates. The occurrence of salt in water acts to reduce the chemical potential of the solution where increasingly saline waters would preferentially be stable as a liquid than as hydrate. With reduced chemical potential, the equilibrium temperature reduces relative to that of pure water (Husebø et al., 2009). As hydrate stability is intrinsically linked to temperature, a corresponding shift in equilibrium pressure is also realised. In order to dissociate hydrate amongst saline water, a greater drop in the local pressure is required. Furthermore, salt is not incorporated into the hydrate structure such that as hydrate forms, the surrounding pore waters become more saline, acting to further inhibit hydrate formation (Sloan & Koh, 2007; Husebø et al., 2009). On the contrary, as hydrate dissociates, the production of pure water dilutes the local saline pore waters and enhances dissociation as the equilibrium pressure is raised.

This shift in equilibrium temperature can be addressed in the following manner (Moridis, 2003):

$$T_d = T_{d,ref} \frac{\log(1 - x_{sa})}{\log(1 - x_{sa,ref})} \qquad (2.34)$$

where T_d [Θ] is the salt induced temperature depression, x_{sa} [-] is the mole fraction of salt in the aqueous solution and $T_{d,ref}$ [Θ] is a reference dissociation temperature for a corresponding reference mole fraction of salt in the aqueous solution, $x_{sa,ref}$ [-]. where x_{sa} can be found from X_{sa} by

$$x_{sa} = \frac{X_{sa}}{M_s} \left(\frac{X_{sa}}{M_s} + \frac{(1 - X_{sa})}{M_w} \right)^{-1} \qquad (2.35)$$

This temperature depression is incorporated into the equilibrium pressure from Eq. (2.32)

as follows:

$$P_e = \sum_{n=0}^{5} a_n (T + T_d)^n \tag{2.36}$$

From Fig. 2.5, it can be seen that the reference points, $T_{d,ref}$ and $x_{sa,ref}$, may vary. The temperature depression, T_d between Sample 1 (sand, 4 ppt) and Sample 2 (sand, 20 ppt) at 3.75 MPa is 1.5 ^{o}C whereas at 7.75 MPa it is 0.9 ^{o}C. Therefore, care must be taken to choose appropriate reference values. The reference values taken from the dataset given by Wright et al. (1999) used in this study vary between the core scale modelling in Chapter 4 and the regional scale modelling in Section 6.1 and are outlined therein.

2.7   Conservation of energy

The first law of thermodynamics states that: *Energy cannot be destroyed or created during a process; it can only change form.* Thermodynamics can deal with the change in energy within a system between equilibrium states due to the work or heat that is applied from outside the system. The first law of thermodynamics can be expressed as

$$\Delta E = Q + W \tag{2.37}$$

where E [ML^{2}T^{-2}] is energy per unit volume, Q [ML^{2}T^{-2}] is heat per unit volume and W [ML^{2}T^{-2}] is work per unit volume.

Energy can take many forms. The total microscopic energy per unit volume is better known as the internal energy per unit volume, U [ML^{2}T^{-2}], and represents the intrinsic kinetic and potential energies of the molecules. Thermal energy is one such form of internal energy where heat describes the flow of this energy by virtue of a temperature gradient. The work done to transport a fluid can be described as the mechanical energy. Mechanical energy includes the macroscopic energies of kinetic energy, the relative energy given to an object in motion, and potential energy, the relative energy of an elevated object. Following on from Eq. (2.37) it can be stated that

$$E = \overbrace{U}^{\text{internal}} + \overbrace{KE}^{\text{kinetic}} + \overbrace{PE}^{\text{potential}} \tag{2.38}$$

where, for an individual phase, j,

$$E_j = U_j + \frac{1}{2}G_j v_j^2 + \rho_j \mathbf{g}z \tag{2.39}$$

where z [L] is the elevation above a reference datum. As velocities in porous media is typically low in this work, the square of the flow velocities become negligible such that kinetic energy can be ignored to leave

$$E_j = U_j + \rho_j gz \tag{2.40}$$

Consider an outlet for which mass can be added or removed. Work can be done on a flowing system by invoking a differential pressure at the outlet. This pressure gradient acts to distribute mechanical energy through the system. Following Cengel & Boles (2002), it

is necessary to incorporate this flow energy into an energy conservation statement:

$$\frac{\partial E_j}{\partial t} = -\nabla \cdot (\boldsymbol{v}_j E_j) - \nabla \cdot \overbrace{(\boldsymbol{v}_j P_j)}^{\text{flow}} \tag{2.41}$$

Substituting Eq. (2.40) into Eq. (2.41) and applying mass conservation $\frac{\partial \rho_j}{\partial t} + \nabla \cdot (\boldsymbol{v}_j \rho_j) = 0$ leads to

$$\frac{\partial U_j}{\partial t} = -\nabla \cdot (\boldsymbol{v}_j U_j) - \nabla \cdot (\boldsymbol{v}_j P_j) \tag{2.42}$$

Further, introducing the definition for enthalpy of phase j per unit volume, H_j [ML^{2}T^{-2}] defined as

$$H_j = U_j + P_j \tag{2.43}$$

and applying it to Eq. (2.42) simplifies the expression to

$$\frac{\partial U_j}{\partial t} = -\nabla \cdot (\boldsymbol{v}_j H_j) \tag{2.44}$$

Assuming that phases are in thermal equilibrium, and thermal conductivity, which does not perform work but instead distributes thermal energy from outside the system, is included as an additional term, it can be said that

$$\frac{\partial U}{\partial t} = -\nabla \cdot (\boldsymbol{v}H) + \overbrace{\nabla \cdot (\kappa_E \nabla \cdot T)}^{\text{conduction}} \tag{2.45}$$

where it is assumed that

$$\kappa_E = \phi(S_g \kappa_g + S_a \kappa_a + S_h \kappa_h) + (1-\phi)\kappa_R \tag{2.46}$$

where κ_j [MLT$^{-3}\Theta^{-1}$] is the thermal conductivity of phase j. Subscript E herein represents "effective" and is assumed proportional to phase saturation.

Re-invoking the available phases in the hydrate dissociation problem and expanding out Eq. (2.45):

$$\frac{\partial U}{\partial t} = h_g \frac{\partial G_g}{\partial t} + G_g \frac{\partial h_g}{\partial t} + h_a \frac{\partial G_a}{\partial t} + G_a \frac{\partial h_a}{\partial t} + h_h \frac{\partial G_h}{\partial t} + G_h \frac{\partial h_h}{\partial t} + h_R \frac{\partial (1-\phi)\rho_R}{\partial t} \tag{2.47}$$

$$+(1-\phi)\rho_R \frac{\partial h_R}{\partial t} - \frac{\partial P}{\partial t} = -\mathbf{F}_g \cdot \nabla h_g - h_g \nabla \mathbf{F}_g - \mathbf{F}_a \cdot \nabla h_a - h_a \nabla \mathbf{F}_a + \nabla \cdot (\kappa_E \nabla \cdot T)$$

where h_j [L^{2}T^{-2}] is enthalpy on a per unit mass basis.

Applying the mass conservation in Eq. (2.10) and considering the available phases therein, noting that $X_{mh} = \frac{M_m}{M_h}$ and $X_{wh} = \frac{M_w N_H}{M_h}$, and assuming the rock is incompressible: $\frac{\partial (1-\phi)\rho_R}{\partial t} = 0$, Eq. (2.47) simplifies to

$$\frac{\partial U^*}{\partial t} = G_g \frac{\partial h_g}{\partial t} + G_a \frac{\partial h_a}{\partial t} + G_h \frac{\partial h_h}{\partial t} + (1-\phi)\rho_R \frac{\partial h_R}{\partial t} - \frac{\partial P}{\partial t} \qquad (2.48)$$

$$= -\mathbf{F}_g \cdot \nabla h_g - \mathbf{F}_a \cdot \nabla h_a + \nabla \cdot (\kappa \nabla \cdot T) + h_D \frac{\partial G_h}{\partial t}$$

where

$$h_D = X_{mh}(h_g - h_h) + X_{wh}(h_a - h_h) \qquad (2.49)$$

It is useful to recast the energy conservation statement in Eq. (2.48) in terms of more recognisable properties such as temperature and pressure.

Firstly take $h = f(T, P)$ such that by partial differentiation it can be said that

$$dh = \left(\frac{\partial h}{\partial T}\right)_P dT + \left(\frac{\partial h}{\partial P}\right)_T dP \qquad (2.50)$$

Substituting in the definition of constant pressure specific heat capacity, C_p [$L^2 T^{-2} \Theta^{-1}$], it follows that

$$dh = C_p dT + \left(\frac{\partial h}{\partial P}\right)_T dP \qquad (2.51)$$

From the following Gibbs relation (Cengel & Boles, 2002):

$$dh = T ds + \nu dP \qquad (2.52)$$

$$\left(\frac{\partial h}{\partial P}\right)_T = T \left(\frac{\partial s}{\partial P}\right)_T + \nu \qquad (2.53)$$

where s [$L^2 T^{-2} \Theta^{-1}$] is entropy per unit mass and ν [$M^{-1}L^3$] is specific volume. From the Gibbs relations, Maxwell relations can be derived and one such useful relationship is outlined here:

$$\left(\frac{\partial s}{\partial P}\right)_T = -\left(\frac{\partial \nu}{\partial T}\right)_P \qquad (2.54)$$

and applying the definition for volumetric expansivity, β [Θ^{-1}]:

$$\beta = \frac{1}{\nu}\left(\frac{\partial \nu}{\partial T}\right)_P \qquad (2.55)$$

and substituting into Eq. (2.53) draws a form in terms of temperature and pressure:

$$dh = C_p dT + \nu(1 - T\beta)dP \qquad (2.56)$$

It can then be shown that for a single phase that

$$\frac{\partial h_j}{\partial t} = C_{pj}\frac{\partial T}{\partial t} + \nu(1 - T\beta)\frac{\partial P_j}{\partial t} \qquad (2.57)$$

and

$$\nabla \cdot h_j = C_{pj}\nabla \cdot T + \nu(1 - T\beta_j)\nabla \cdot P_j \qquad (2.58)$$

which when substituted into Eq. (2.48), given that $\rho_j = \frac{1}{\nu_j}$ and recalling that capillary pressure is not included, produces the following energy conservation statement in terms of pressure, temperature and composition:

$$\frac{\partial U^*}{\partial t} = (\rho C_p)_E \frac{\partial T}{\partial t} - T\beta_E \frac{\partial P}{\partial t} - h_D \frac{\partial G_h}{\partial t} \qquad (2.59)$$

$$= -(F_g C_{pg} + F_a C_{pa})\nabla T + q_g(1 - T\beta_g)\nabla \cdot P + q_a(1 - T\beta_a)\nabla \cdot P + \nabla \cdot (\kappa_E \nabla \cdot T)$$

where

$$(\rho C_p)_E = \phi(S_g \rho_g C_{pg} + S_a \rho_a C_{pa} + S_h \rho_h C_{ph}) + (1 - \phi)\rho_R C_{pR} \qquad (2.60)$$

$$\beta_E = \phi(S_g \beta_g + S_a \beta_a + S_h \beta_h) + (1 - \phi)\beta_R \qquad (2.61)$$

2.7.1 Enthalpy of dissociation

Depending on the phase change, energy can be taken in endothermically, or released exothermically. Hydrate dissociation takes in energy endothermically to break apart the lattice. This process coincides with a drop in temperature. The opposite can be said for hydrate formation. The dissociation process is for some part, self-stabilising, because a reduction in the local temperature may restabilise hydrate through a reduction in the equilibrium pressure. Ignoring this process would lead to overestimations in the gas produced as hydrate decomposes (Ruppel and Kessler, 2017).

In previous studies by Anderson (2004) and Gupta et al. (2008), the Clapeyron equation was used to determine the enthalpy of dissociation, h_D [$L^2 T^{-2}$]. It was remarked by both authors that the simplified Clausius-Clapeyron was inadequate at predicting the

latent heat loss upon dissociation. From Eq. (2.49), h_D can also be recast in terms of pressure, temperature and composition. Consider the following Maxwell relation:

$$\left(\frac{\partial P}{\partial T}\right)_v = \left(\frac{\partial s}{\partial v}\right)_T \tag{2.62}$$

Phase changes occur at equilibrium and as such it follows that the pressure is at the equilibrium (saturation) pressure for a given temperature only. Therefore, it can be said that

$$\left(\frac{dP_e}{dT}\right)_{sat} = \frac{s_j - s_h}{v_j - v_h}, \qquad j = g, a \tag{2.63}$$

which is the well-known Clapeyron equation. Substituting in the Gibbs relation from Eq. (2.52) and because phase changes occur at constant pressure (i.e $dP = 0$), it follows that

$$h_j - h_h = T\left(\frac{dP_e}{dT}\right)\left(\frac{1}{\rho_j} - \frac{1}{\rho_h}\right), \qquad j = g, a \tag{2.64}$$

Substituting into Eq. (2.49) leaves an expression for the enthalpy of dissociation, h_D:

$$h_D = T\left(\frac{dP_e}{dT}\right)\left[\left(\frac{1}{\rho_g} - \frac{1}{\rho_h}\right)X_{mh} + \left(\frac{1}{\rho_a} - \frac{1}{\rho_h}\right)X_{wh}\right] \tag{2.65}$$

where $\frac{dP_e}{dT}$ can be derived directly by differentiating the empirical three-phase equilibrium equation in Eq. (2.36):

$$\frac{dP_e}{dT} = P_e \sum_{n=1}^{5} na_n(T + T_d)^{n-1} \tag{2.66}$$

The function in Eq. (2.65) is used in this study to determine h_D because it was derived intrinsically from the conservation of energy and accounts for compositional change. This formulation is compared to the enthalpy of dissociation data obtained experimentally by Anderson (2004) and Gupta et al. (2008) in Fig. 2.7.
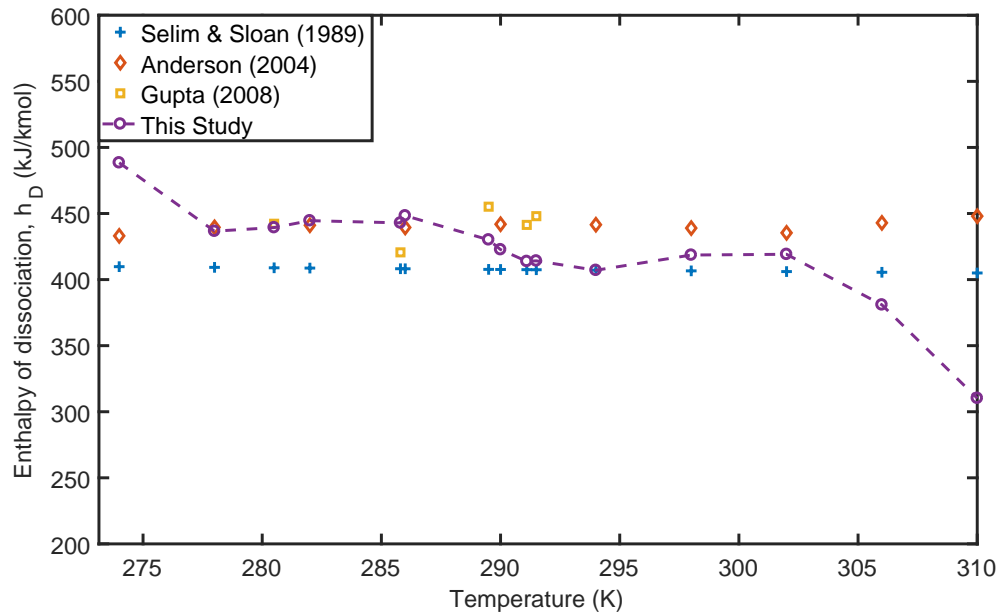
Fig. 2.7: A comparison of the enthalpy of dissociation determinations. The pressures and temperatures input into Eq. (2.65) are taken from Anderson (2004) and Gupta et al. (2008).

2.8 Thermophysical properties

Solutions to the governing equations require thermophysical properties for the numerous phases within the system at any given pressure, temperature and where applicable, composition. These properties include: density, ρ, viscosity, μ, specific heat capacity at constant pressure, C_{pj}, thermal conductivity, κ, Joule-Thomson coefficient, μ_{JT}, volumetric expansivity, β, and isothermal compressibility, α [$M^{-1}LT^2$].

2.8.1 Gaseous and aqueous phases

For pure methane and pure water components, interpolation tables were produced from the thermophysical properties of fluid systems in the Chemistry WebBook feature provided by NIST (Lemmon et al., 2013). A range of properties can be downloaded here including: temperature, pressure, density, volume, internal energy, enthalpy, entropy, specific heat capacity at constant volume and constant pressure, sound speed, Joule-Thomson coefficient, dynamic viscosity and thermal conductivity. Information on the phase can also be retrieved. β_j can be found from the following:

$$\beta_j = \frac{\rho_j C_{pj} \mu_{JTj} + 1}{T} \tag{2.67}$$

and α_j can be found from the "Mayer relation" as follows:

$$\alpha_j = \frac{T\beta_j^2}{\rho_j(C_{pj} - C_{vj})} \tag{2.68}$$

Salinity can act to retard the flow of the aqueous phase. The thermophysical properties of the aqueous phase therefore need to account for the presence of salt. Brine density, brine viscosity and brine specific heat capacity at constant pressure are determined by empirical expressions. For simplicity, the remaining thermophysical properties for brine are assumed to be equal to that of pure water because, for the salinity range of 0 to 35 ppt (sea water), preliminary work showed the deviation from pure water to not significantly impact the modelling results. Phase density for brine, ρ_a, takes the empirical form from Batzle & Wang (1992) as follows and is depicted in Fig. 2.8:

$$\rho_a = \rho_{H_20} + X_{sa}(0.668 + 0.44X_{sa} + 10^{-6} \cdot \tag{2.69}$$

$$(300P - 2400PX_{sa} + T(80 + 3T - 3300X_{sa} - 13P + 47PX_{sa}))), \qquad \text{g/cm}^3$$
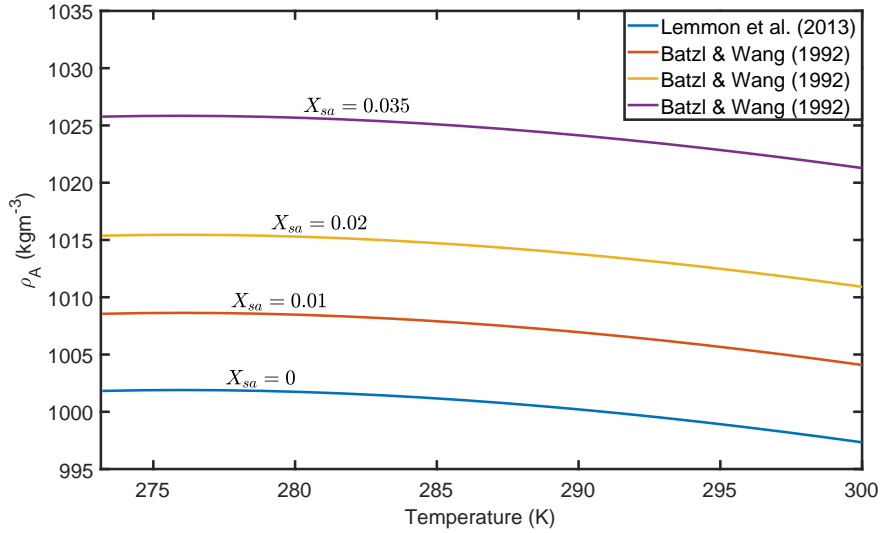
Fig. 2.8: Aqueous phase density variation with increasing salinity ($P = 4$ MPa).

where $\rho_{H_2 0}$ [ML^{-3}] is the density of pure water, in this case provided by the NIST look-up table (Lemmon et al., 2013). Note, P is in MPa and T is in ^{o}C. Similarly, brine viscosity is also taken from Batzle & Wang (1992) as follows and is shown in Fig. 2.9:

$$\mu_a = 0.1 + 0.333 X_{sa} + \tag{2.70}$$

$$(1.65 + 91.9 X_{sa}{}^3) \exp[-(0.42(X_{sa}{}^{0.8} - 0.17)^2 + 0.045)T^{0.8}], \qquad \text{mPa s}$$

Specific heat capacity of brine varies with salinity. The expression provided by Sharqawy et al. (2010) does not factor in pressure, however the range of pressures in this study does not deviate C_p as significantly as salt. It is calculated as follows and shown in Fig. 2.10:

$$C_{pa} = A(X_{sa}) + B(X_{sa})T + C(X_{sa})T^2 + D(X_{sa})T^3, \qquad \text{kJ/kg/K} \tag{2.71}$$

where

$$
\begin{aligned}
A &= 5.328 - (9.76 \times 10^{-2})X_{sa} + (4.04 \times 10^{-4})X_{sa}{}^2 \\
B &= -6.913 \times 10^{-3} + (7.351 \times 10^{-4})X_{sa} - (3.15 \times 10^{-6})X_{sa}{}^2 \\
C &= 9.6 \times 10^{-6} - (1.927 \times 10^{-6})X_{sa} + (8.23 \times 10^{-9})X_{sa}{}^2 \\
D &= 2.5 \times 10^{-9} + (1.666 \times 10^{-9})X_{sa} - (7.125 \times 10^{-12})X_{sa}{}^2
\end{aligned}
\tag{2.72}
$$
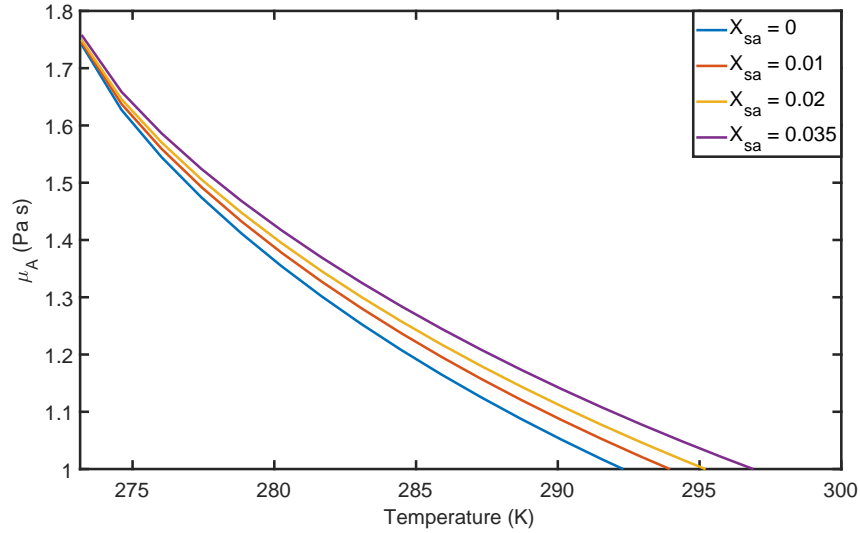
Fig. 2.9: Aqueous phase viscosity variation with increasing salinity ($P = 4\text{MPa}$).
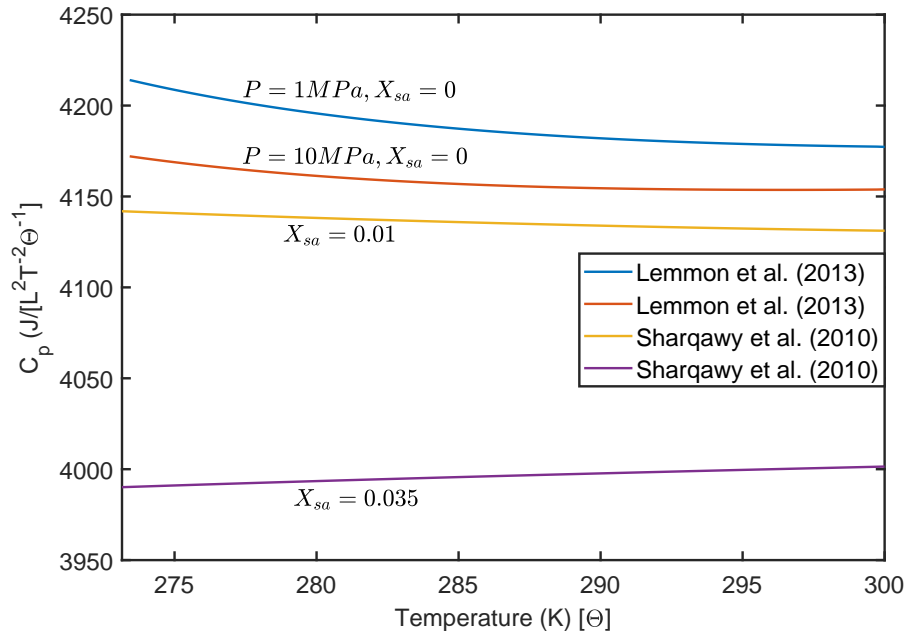
Fig. 2.10: Aqueous phase specific heat capacity constant pressure with increasing salinity. Note the greater dependence of C_p on salinity than on pressure.

2.8.2 Hydrate and rock medium

A constant density for structure I hydrae is taken from Selim & Sloan (1989) and is $\rho_h = 913\text{kgm}^{-3}$. As the experiment performed by Masuda et al. (1999) is a key focus to this thesis, many of the thermophysical properties for the hydrate are taken to be the same, such as thermal conductivity of hydrate, $\kappa_h = 0.393\text{Wm}^{-1}\text{K}^{-1}$, and specific heat capacity of hydrate, $C_{ph} = 2010\text{Jkg}^{-1}\text{K}^{-1}$. Following Masuda et al. (1999), hydrate is assumed incompressible: $\alpha_h = \beta_h = 0$. Rock properties vary with the study area in Chapter 4 and Section 6.1. However, rock is also assumed to be incompressible, such that $\alpha_R = \beta_R = 0$.

3. NUMERICAL SOLUTION

3.1 Objective

- Outline the Method of Lines approach and the necessary requirements for implementation.

- Present MATLAB's ODE solvers.

- Introduce the finite differencing scheme used in this study to discretise in space and integrate with time.

3.2 Highlights

- Numerical stiffness is a significant consideration for the hydrate dissociation problem.

- Mass and energy conservation statements in Chapter 2 are recast in terms of primary dependent variables which are persistent throughout the simulation.

- Discontinuities in the flowing phases can be resolved using an exact Riemann solver - Godunov's 1st order upwinding scheme.

3.3   Introduction

Evaluating mass and heat transfer through time and space regularly requires solving partial differential equations (PDEs) of the kind described by the mass and energy conservation statements in Chapter 2 (see Eqs. (2.15), (2.28) and (2.45)). These equations have the same order of spatial dimensions as for time and therefore can be considered to form a set of quasi-hyperbolic PDEs. The equations are not completely hyperbolic because the spatial derivatives contain further derivatives (recall the pressure gradient in Darcy's law).

Assumptions such as incompressible flow, negligible capillary pressure and homogeneity can enable the problem to be solved analytically using the method of characteristics (Orr, 2007). Problems involving compressible flow (i.e. density change with pressure) generally require numerical methods, whereby spatial and temporal derivatives are replaced by approximate algebraic expressions across a domain discretised into a set of cells.

The Finite Element Method (FEM) is one such approach that solves PDEs in an integral form for cells with a fixed volume. Properties are interpolated across each cell using polynomials of a given order of accuracy. The Finite Volume Method (FVM) is similar to FEM but with piecewise properties for each cell. Whereas FEM integrates across the volume, FVM balances mass between adjacent control volumes through discretised surface integrals at the boundaries. Both methods are considered integral methods and can more readily handle irregular geometries. Alternatively, a differential method can be employed, namely the Finite Difference Method (FDM), which assumes that the properties of the cell is instead concentrated at the centre of the cells. The FDM is considered the easiest to implement on static grids by readily replacing derivatives of the conservation equations with algebraic expressions in the form of finite differences. The FDM works best across simple control volume shapes which makes it easy to increase the resolution for improved accuracy. While both FVM and FDM methods employ truncated expansions of the Taylor series, care must be taken with FDM because the accuracy of the scheme is limited by the precision (order) of the Taylor series expansion unlike FVM which by its very nature is conservative. This study uses the FDM.

In this chapter, the finite difference numerical approach is developed. Firstly, the Method of Lines (MOL) approach is introduced, describing how a set of hyperbolic PDEs can be approximated by a set of ordinary differential equations (ODE). Following on from this, time integration is discussed, with a focus on MATLAB's ODE solver, ode15s, which

will be used in this study (Shampine et al., 2003). Typically, when solving MCMP problems numerically, the governing equations are solved in terms of a set of primary dependent variables (PDVs) such as pressure, temperature and concentration (mass density or saturation) (Amaziane et al., 2012). This chapter will outline an appropriate selection of PDVs for the hydrate dissociation problem. Finally, the spatial discretisation schemes are then evaluated including how to handle fluxes across discontinuities during simulation.

3.4   Formulating the problem
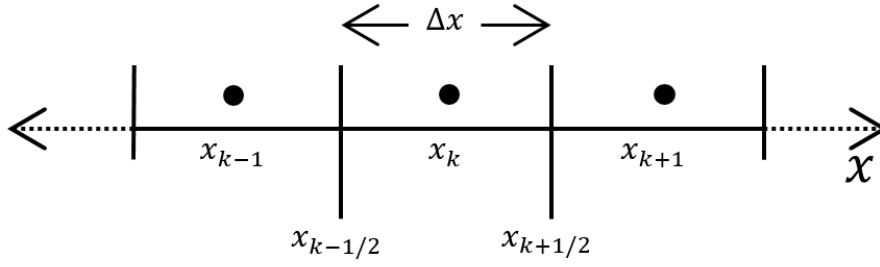
Fig. 3.1: Schematic of the discretised numerical grid.

Let x [L] be a spatial dimension and k be the spatial location of a node on the grid as shown in Fig. 3.1, where a node is defined as the centre of a cell. Each cell is Δx wide.

Consider the following 1D PDE spatially discretised by N number of nodal points to form a set of N PDEs similar in form to the mass conservation equation described in Eq. (2.15):

$$\frac{\partial \boldsymbol{G}}{\partial t} = \frac{\partial \mathbf{F}}{\partial x} \tag{3.1}$$

where $\boldsymbol{G}$ is defined as

$$\boldsymbol{G} = [G_1, G_2, ..., G_N] \tag{3.2}$$

of which the initial condition is

$$\boldsymbol{G}(t = t_0) = \boldsymbol{G}_0 \tag{3.3}$$

and

$$\mathbf{F} = [\mathrm{F}_1(\boldsymbol{G}), \mathrm{F}_2(\boldsymbol{G}), ..., \mathrm{F}_N(\boldsymbol{G})] \tag{3.4}$$

Through the chain rule, it can also be shown that

$$\frac{\partial \boldsymbol{G}}{\partial t} = \mathbf{J}\frac{\partial \boldsymbol{G}}{\partial x} \tag{3.5}$$

where $\mathbf{J}$ is the jacobian matrix defined as

$$\mathbf{J} = \frac{\partial \mathbf{F}}{\partial \boldsymbol{G}} = \begin{bmatrix} \frac{\partial \mathrm{F}_1}{\partial G_1} & \cdots & \frac{\partial \mathrm{F}_1}{\partial G_N} \\ \vdots & \ddots & \vdots \\ \frac{\partial \mathrm{F}_N}{\partial G_1} & \cdots & \frac{\partial \mathrm{F}_N}{\partial G_N} \end{bmatrix} \tag{3.6}$$

The Jacobian matrix describes the dependency of $\mathbf{F}$ on $\boldsymbol{G}$ and is discussed in more detail in Section 3.8.

3.5 The method of lines

The Method of Lines (MOL) is a common method used to solve PDEs (Schiesser, 2012; Wouwer et al., 2005; Haq et al., 2012) and has previously been applied for multi-component, multi-phase problems in porous media (Mathias et al., 2014; Goudarzi et al., 2016; Hardwick & Mathias, 2017). In essence, the MOL replaces all the derivatives (generally all the spatial derivatives) in the set of PDEs with algebraic approximations, bar one (generally the temporal derivative). Furthermore, with only one remaining continuous independent variable, the problem now becomes a system of ODEs that approximates the original PDE as an initial value problem (IVP). The MOL is an attractive approach to take because of this simple implementation and the wide availability of high quality ODE solvers designed for IVPs (Wouwer et al., 2005). One such high quality ODE solver used in this study is MATLAB's ode15s while another, used less minimally in this study, is ode45. In order to utilise the MOL approach in this way, two aspects must be evaluated:

- How to handle time integration and implement the ODE solvers.

- How to approximate the spatial derivatives with algebraic expressions.

3.6 Numerical integration

Projecting the value G_k from a point in time, n, to a time of interest $n+1$, where Δt is the step in time given by $\Delta t = t(n+1) - t(n)$, can be expressed by the expansion of a Taylor series. Numerical integration involves discretising a continuous function, such that the Taylor series is truncated for a desired order, M. Higher order terms including and greater than $M+1$, are considered as "truncation error" - the difference between the exact (a Taylor series of infinite order) and the approximation. This can be understood as follows:

$$G_k(t+\Delta t) = G_k(t) + \sum_{m=1}^{M} \frac{\Delta t^m}{m!} \frac{\partial^m G_k(t)}{\partial t^m} + O(\Delta t^{M+1}) \qquad (3.7)$$

Truncating Eq. (3.7) to a 1st order approximation ($M = 1$) and replacing the terms with index notation leaves

$$G_k^{n+1} = G_k^n + \Delta t \frac{\partial G_k^n}{\partial t} + O(\Delta t^2) \qquad (3.8)$$

The above equation is commonly referred to as an explicit time-stepping scheme, or, Forward Euler scheme. It is so named because it takes the information explicitly from the current time and uses it to find the information at the next time. Explicit schemes are relatively simple to implement but often have limiting stability constraints. Excessively large time-steps, Δt, will violate the Courant-Friedrichs-Lewy condition leading to numerical instability which manifests itself as unstable oscillations in the solution. On evaluation of G_k at time $n+1$, this condition states that Δt must be lower than the time taken for a propagating wave to travel to adjacent nodes $k+1$ and $k-1$ (Leveque, 1992). Alternatively, a so-called implicit time-stepping scheme, or Backward Euler, can be used. Here, information from the next time-step is included into the formulation. Implicit schemes are subsequently more difficult to implement but are stable for all time-steps at the cost of being more diffusive (Goudarzi et al., 2016). Similar to Eq. (3.7), by expanding a Taylor series about $G_k(t - \Delta t)$, an implicit scheme can be derived as follows:

$$G_k(t-\Delta t) = G_k(t) + \sum_{m=1}^{M} \frac{(-\Delta t)^m}{m!} \frac{\partial^m G_k(t)}{\partial t^m} + O(\Delta t^{M+1}) \qquad (3.9)$$

From which, truncating to the 1st order, it can be seen that

$$G_k^{n+1} = G_k^n + \Delta t \frac{\partial G_k^{n+1}}{\partial t} + O(\Delta t^2) \qquad (3.10)$$

Note that the implicit scheme has the unknown time, $n+1$, on both sides of the equation. Mixed implicit-explicit schemes such as IMPES (Implicit Pressure - Explicit Saturation) which try to incorporate the advantages of both schemes, are also popular for MCMP numerical modelling (Chen et al., 2006) and have been used to solve the hydrate dissociation problem (Liang et al., 2010; Zhao et al., 2012a). However, the stability of IMPES schemes are still limited by the time-step when solving for saturation. This can become computationally expensive as more steps are required when dealing with higher resolution problems (Chen et al., 2006).

In all cases, integration error can be reduced by truncating the Taylor series at higher orders, therefore enabling a larger Δt to be employed without significantly compromising accuracy. However, using a smaller Δt decreases the importance of the higher order terms and allows earlier truncation of the Taylor series whilst maintaining an acceptable level of error. Therefore, choosing the degree of accuracy becomes a trade-off between using a computationally more expensive higher order approximation for the time derivatives or reducing the size of the time-step, which will, in turn, require more time-steps to complete the simulation (Cellier & Kofman, 2006).

3.6.1   Numerical stiffness

Instability caused by numerical stiffness can become of significant concern when dealing with a set of coupled differential equations when incorrectly handling the time-step. A solution may be considered stiff when there are two or more very different scales of the independent variable (i.e., space or time) on which the dependent variables are changing (Press, 2007). An example taken from Davis (2013) is herein outlined.

Consider the reaction pathway:

$$A \underset{k_2}{\overset{k_1}{\rightleftharpoons}} B \overset{k_3}{\rightarrow} D$$
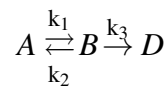
Let C_A [-] and C_B [-] be concentrations of their respective substances. Let the reaction constants k_1 [T^{-1}], k_2 [T^{-1}] and k_3 [T^{-1}] be 1000, 1 and 1, respectively. The independent variable here is time, t, and the following initial conditions apply:

$$C_A(t=0) = C_{A0}, \qquad C_B(t=0) = 0 \tag{3.11}$$
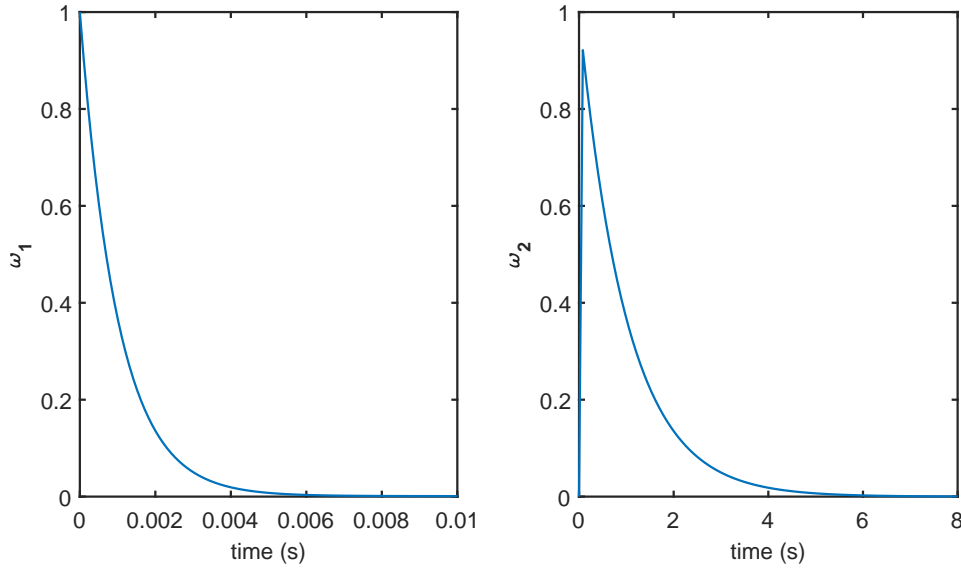
Fig. 3.2: Results from Eq. (3.15)

The associated governing differential equations are as follows:

$$\frac{dC_A}{dt} = -k_1C_A + k_2C_B \tag{3.12}$$

$$\frac{dC_B}{dt} = k_1C_A - (k_2 + k_3)C_B \tag{3.13}$$

which can be written in a compact form as

$$\frac{d\omega}{dt} = \mathbf{Q}\omega = \mathbf{f}, \quad \omega(t=0) = [1,0]^T \tag{3.14}$$

where T is transpose and

$$\omega = \begin{bmatrix} C_A/C_{A0} \\ C_B/C_{A0} \end{bmatrix}, \qquad \mathbf{Q} = \begin{bmatrix} -k_1 & k_2 \\ k_1 & -(k_2+k_3) \end{bmatrix}, \qquad \mathbf{f} = \begin{bmatrix} f_1 \\ f_2 \end{bmatrix}$$

Through separation of variables, the solution to Eq. (3.14) is

$$\omega_1 = \frac{1000}{1001}e^{-1001t} + \frac{1}{1001}e^{-t} \tag{3.15}$$

$$\omega_2 = -\frac{1000}{1001}e^{-1001t} + \frac{1000}{1001}e^{-t}$$

These solutions are plotted against time in Fig. 3.2 to emphasise the diference in time-scale dependency of ω_1 and ω_2. With increasing t, ω_1 decays very rapidly whereas ω_2 decays orders of magnitude slower. The maximum time step that could be utilised when

integrating Eq. (3.14) using an explicit time-stepping scheme and maintain numerically stability is

$$\Delta t_{max} < \frac{1}{1001} \tag{3.16}$$

This is very small despite the fact that the time taken for full evolution of the solution is controlled by the slower decay rate in ω_2 as shown in Fig. 3.2.

Generally there are two solutions to this problem that may be taken. One solution would be to reformulate the problem in order to remove the term that generates stiffness in the integration scheme, e^{-1001t}. Another option is to use an implicit rather than an explicit scheme.

3.6.2 MATLAB's ODE solvers

MATLAB provides the user with a selection of higher order solvers using an array of methods of varying accuracies and time-stepping schemes. They are able to solve IVPs across a finite interval of $a \leq t \leq b$ (Shampine et al., 2003).

3.6.2.1 ode45

One such solver using higher order integration methods is ode45. This solver uses an explicit Runge-Kutta method, truncating to 5 orders of accuracy. The Runge-Kutta is an improved approximation to the Euler method that uses a recurrence formula but adjusts the time-step size based on evaluations of the Taylor series truncation error at intermediate steps. It is a single step method because it only requires the solution of the immediately preceding point (i.e. solving G_k^{n+1} from G_k^n).

3.6.2.2 ode15s

In this study, the mass conservation equations used to describe the hydrate dissociation problem contain a flux term and a source term as shown in Eq. (2.15). In the kinetic model, the source term controls the dissociation and is rate dependent. The kinetic model is considered a stiff problem because dissociation is slow compared to the propagation of the pressure wave associated with fluid movement. Subsequently, an implicit solver should be utilised.

MATLAB recommends using their built-in implicit solver designed for stiff problems, ode15s, where the "s" denotes "stiff". Rather than use a one-step Runge-Kutta method, a

5th order variation of a linear multi-step method called the backward differentiation formula (BDF) is used (Shampine et al., 2003). Here, G_k^n is determined by a polynomial $P(n)$ of order M that interpolates G_k^{n+1} in conjunction with the previous evaluations at G_k^n, G_k^{n-1},..., G_k^{n-M}. The polynomial is to satisfy the ODE at time $n+1$ and then used to estimate a value for G_k^{n+1}. The 1st order backwards Euler scheme expressed in Eq. (3.10) is the simplest case of a BDF called BDF1. Higher order BDFs provide greater accuracy as they incorporate more of the previous terms. ode15s uses an expansion on the BDF called the numerical differentiation formula (NDF) whereby, for higher order BDFs ($M > 2$), the NDF approach uses the information at previous times to refine the stability for a given step (Shampine & Reichelt, 1997). The NDF is the default setting for ode15s.

The solver ode45 calculates the truncation error from the 4th order approximation and compares this with the truncation error of the 5th order. In this routine, if the truncation error lies above an acceptable tolerance (MATLAB default error $tol = 10^{-3}$) the time-step is reduced. In a similar manner, ode15s uses the truncation error of the 1st and 5th orders respectively. A point to make here is that by controlling the error in the solution and reducing Δt accordingly, the stability of the scheme is also maintained.

3.6.3   Primary dependent variables

As material phases appear and disappear, such as is the case with hydrate formation and dissociation, the primary dependent variables (PDV) solved for in the system may change. In this context, many simulators, including TOUGH+HYDRATE, handle this by using a variable substitution algorithm called the "primary variable switch method" (PVSM) according to some "switching criteria" (Sun & Mohanty, 2006; Gamwo & Liu, 2010; Moridis, 2012; Bourgeat et al., 2013). In the context of hydrate dissociation, the mass and energy conservation equations are solved for different phase saturations, S_j, phase pressures, P_j, and temperature, T, across the domain depending upon whether hydrate is stable, dissociating or dissociated (see Table 3 in Gamwo & Liu (2010)). Alternatively, the need to switch PDVs can be bypassed by choosing a different set of PDVs that are persistent throughout the simulation (Amaziane et al., 2012; Bourgeat et al., 2013; Goudarzi et al., 2016). This is especially important if MATLAB's ODE solvers are to be used because these do not allow the user to switch PDVs during simulation.

3.6.3.1 Recasting in terms of the primary dependent variables

An appropriate choice of PDVs which are persistent throughout the simulation are pressure, P, temperature, T, and mass fraction of component, z_i [-]. where

$$z_i = \frac{G_i}{F} \qquad (3.17)$$

G_i is the mass of component i per unit volume in Eq. (2.10) and F [ML^{-3}] is the bulk mass per unit volume given as

$$F = \sum_{i=1}^{N_c} G_i \qquad (3.18)$$

where N_c is the number of components considered. Furthermore, note that

$$\sum_{i=1}^{N_c} z_i = 1 \qquad (3.19)$$

Previous studies have also shown that G_i can be an effective PDV (Amaziane et al., 2012; Bourgeat et al., 2013). However, an advantage of using z_i over G_i is that z_i is independent of P and T. For a given mass of fluid mixture, z_i will not change with pressure and temperature.

Partially differentiating Eq. (3.17) with respect to time gives

$$\frac{\partial z_i}{\partial t} = \frac{1}{F}\left(\frac{\partial G_i}{\partial t} - z_i\frac{\partial F}{\partial t}\right) \qquad (3.20)$$

where from Eq. (3.18):

$$\frac{\partial F}{\partial t} = \sum_{i=1}^{N_c} \frac{\partial G_i}{\partial t} \qquad (3.21)$$

and $\frac{\partial G_i}{\partial t}$ is easily retrievable from Eq. (2.15).

Given that P, T and z_i have been chosen as the PDVs, it can also be said that

$$\frac{\partial F}{\partial t} = \frac{\partial F}{\partial P}\frac{\partial P}{\partial t} + \frac{\partial F}{\partial T}\frac{\partial T}{\partial t} + \sum_{i=1}^{N_c-1} \frac{\partial F}{\partial z_i}\frac{\partial z_i}{\partial t} \qquad (3.22)$$

Note that, due to Eq. (3.19), there are $N_c - 1$ time derivatives of z_i to account for. The derivatives, $\frac{\partial F}{\partial P}$, $\frac{\partial F}{\partial T}$ and $\frac{\partial F}{\partial z_i}$ will vary with formulation in Chapter 4 and Chapter 5 and are derived therein.

Recall from Section 2.7, the energy conservation statement in Eq. (2.45) for a flowing

system involving hydrate was recast in terms of P T and z_i to give the following:

$$\frac{\partial U^*}{\partial t} = (\rho C_p)_E \frac{\partial T}{\partial t} - T\beta_E \frac{\partial P}{\partial t} - h_D \frac{\partial G_h}{\partial t} \tag{3.23}$$

The expressions in Eqs. (3.20), (3.22) and (3.23) are important because they directly relate the time derivatives of the PDVs with the original conservation statements (Goudarzi et al., 2016).

3.7 Algebraic approximations to the spatial derivatives

3.7.1 Finite differencing schemes

The simplest way of algebraically approximating the spatial derivatives is to use the finite difference method. Finite differences take a continuous domain and discretises it into N number of points. For a grid of fixed size, increasing N leads to a closer approximation to the original continuum function.

Recall Eq. (3.1). As in Eqs. (3.7) and (3.9), the Taylor series can be used to expand around $F(x + \Delta x)$ where Δx is the distance between two adjacent points. Note that $F(x + \Delta x) = F_{k+1}$ when $F(x) = F_k$.

$$F(x + \Delta x) = F(x) + \sum_{m=1}^{M} \frac{\Delta x^m}{m!} \frac{\partial^m F(x)}{\partial x} + O(\Delta x^{M+1}) \tag{3.24}$$

By truncating for $M = 1$, the 1st order forward difference derivative can be found as

$$\frac{\partial F}{\partial x} = \frac{F_{k+1} - F_k}{\Delta x} + O(\Delta x) \tag{3.25}$$

Similarly, a backward differencing scheme can be derived by expanding a Taylor series about $F(x - \Delta x)$:

$$F(x - \Delta x) = F(x) + \sum_{m=1}^{M} \frac{(-\Delta x)^m}{m!} \frac{\partial^m F(x)}{\partial x} + O(\Delta x^{M+1}) \tag{3.26}$$

Again truncating to $M = 1$, the 1st order backwards difference is stated as follows:

$$\frac{\partial F}{\partial x} = \frac{F_k - F_{k-1}}{\Delta x} + O(\Delta x) \tag{3.27}$$

Adding Eq. (3.24) to Eq. (3.26) and truncating to $M = 2$, with some rearrangement, gives an approximation to the 2nd order derivative:

$$\frac{\partial^2 F}{\partial x^2} = \frac{F_{k-1} - 2F_k + F_{k+1}}{\Delta x^2} + O(\Delta x^2) \tag{3.28}$$

3.7.2   Riemann Problem

Consider an enclosed domain fully saturated with hydrate held at a pressure above the equilibrium pressure. If pressure reduces or heat is input at one end of the domain, a front emerges separating the dissociated and undissociated regions. Depending upon the front velocity and/or the observational scale, this front can appear smooth or sharp in numerical simulations.

Problems that involve conservation equations and a single, sharp discontinuity are often termed "Riemann problems". When solving PDEs, it is sometimes necessary to resolve fluxes at half points. Indeed, the spatial derivatives in Eq. (3.25) and (3.27) could be considered to occur at $k + 1/2$ and $k - 1/2$ respectively. However, when crossing a sharp discontinuity, problems can arise when including half points into the fluxes. From Fig. 3.3, as a wave propagates from left to right, the flux F at $x_{k+1/2}$ does not include detail about the propagating wave unlike $x_{k-1/2}$. Thus, for a sharp discontinuity, improving the resolution causes G_k to tend to infinity (Leveque, 1992). Riemann solvers are used to determine the fluxes $F_{k\pm1/2}$. One such Riemann solver is the Godunov scheme (Leveque, 1992).
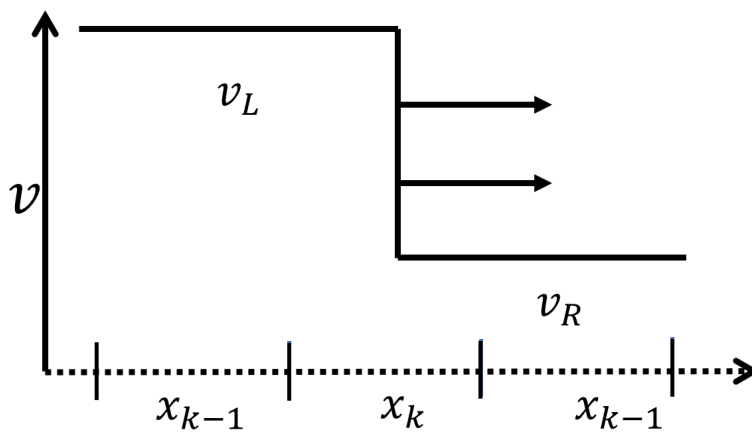
Fig. 3.3: Propagation of a wave through a grid in direction *x*. Notice that the direction of travel moves from high velocity to low velocity. v_L is the velocity on the left of the front and v_R is the velocity on the right of the front.

3.7.2.1 Godunov's method

When faced with a sharp discontinuity in an initial value problem, the Godunov method assumes a constant piecewise data distribution over the spatial grid as shown in Fig. 3.4.
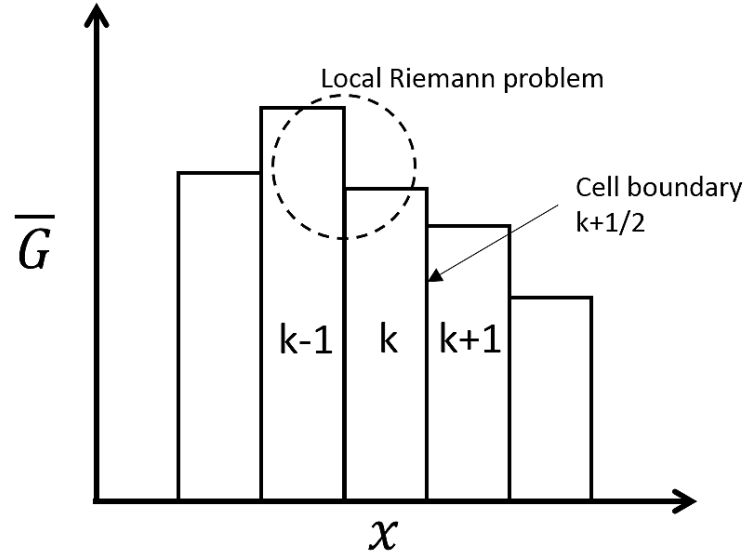
Fig. 3.4: Schematic showing the piecewise distribution for $\bar{G}$ Eq. (3.31). The Riemann problem is highlighted where at $x_{k-1/2}$, $\bar{G}_i$ can pose two solutions.

Godunov's method for solving Riemann problems involves integrating Eq. (3.1) with respect to space:

$$\frac{d}{dt}\int_{x_{k-1/2}}^{x_{k+1/2}} G(x,t)dx = -[F(G(x_{k+1/2},t)) - F(G(x_{k-1/2},t))] \tag{3.29}$$

and then integrating with respect to time:

$$\int_{x_{k-1/2}}^{x_{k+1/2}} G(x,n+1)dx = \int_{x_{k-1/2}}^{x_{k+1/2}} G(x,n)dx + \int_{n}^{n+1} F(G(x_{k-1/2},t))dt - \int_{n}^{n+1} F(G(x_{k+1/2},t))dt \tag{3.30}$$

The above equations are then replaced by a piecewise distribution which is taken by averaging across the cells as follows:

$$\bar{G}_k{}^n = \frac{1}{\Delta x}\int_{x_{k-1/2}}^{x_{k+1/2}} G(x,n)dx \tag{3.31}$$

and

$$\bar{F}_{k\pm 1/2} = \frac{1}{\Delta t}\int_{n}^{n+1} F(x_{\pm 1/2},t)dt \tag{3.32}$$

such that Eq. (3.30) simplifies to

$$\bar{G}_k^{n+1} = \bar{G}_k^n + \frac{\Delta t}{\Delta x}(\bar{F}_{k-1/2} - \bar{F}_{k+1/2}) \tag{3.33}$$

It is important to recognise that Eq. (3.33) is not yet a numerical scheme but is instead an analytical solution of how G_k changes with time. At the boundary between two adjacent cells, $\bar{G}_k$ manifests a jump, generating a sequence of local Riemann problems to be solved simultaneously. $\bar{G}_k$ has two possible values. A numerical approximation of $\bar{F}_{k\pm1/2}$ is necessary to calculate the appropriate value for $\bar{G}_k^{n+1}$.

3.7.2.2   Godunov's upwinding scheme

A 1st order upwinding scheme complementary to the Godunov method can be employed to approximate $\bar{F}_{k\pm1/2}$ in Eq. (3.33). Consider a wave propagating from left to right towards $x_{k+1/2}$ as shown in Fig. 3.3. If $\bar{F}_{k+1/2}$ is to be replaced with a 1st order approximation, $\bar{F}_{k+1/2}$ has two possible solutions. The Godunov upwinding scheme requires the selection of the side with the largest velocity because this indicates the direction of travel. Fig. 3.3 depicts a propagating wavefront yet to reach x_{k+1}. In this case, taking $\bar{F}_{k+1/2} = F_{k+1}$ would ignore the presence of the wavefront and the values associated with it. Instead, the correct approximation is to choose F_k. This can be best summarised as follows:

$$\bar{F}_{k+1/2} = \begin{cases} F_k, & v > 0 \\ F_{k+1}, & v \leq 0 \end{cases} \tag{3.34}$$

Were the front not propagating, either case would be acceptable to choose, hence it is academic which choice includes the case for when $v = 0$.

It is worthwhile here to expand $\mathbf{F}$ in Eq. (3.1) for phase j in a 1D case in order to best illustrate how this is implemented for the mass conservation statements (Eq. (2.15)) in this problem. Expanding out $\mathbf{F}_j$ leads to

$$\mathbf{F}_j = \lambda_j(\mathbf{G}_j)\frac{\partial}{\partial x}\zeta_j(\mathbf{G}_j) \tag{3.35}$$

where

$$\lambda_j = \frac{\rho_j k k_{rj}}{\mu_j} \tag{3.36}$$

and ζ_j [$ML^{-2}T^{-2}$] is the smooth flowing gradient associated with the mass flux, **F**, given as

$$\zeta_j = \frac{\partial P_j}{\partial x} + \rho_j g \tag{3.37}$$

The propagating front is effectively a mobile phase point source/sink (line for 2D) as hydrate dissociates/forms. The jump in $\bar{G}_j|_k$ manifests due to a change in $\bar{\lambda}_j$ through relative permeability - recall $k_{rj}(S_j)$. Subsequently, the Godunov scheme needs to be applied to λ_j such that

$$\bar{\lambda}_j|_{k+1/2} = \begin{cases} \lambda_j|_k, & v > 0 \\ \lambda_j|_{k+1}, & v \leq 0 \end{cases} \tag{3.38}$$

where $v = \left.\frac{\partial \zeta_j}{\partial x}\right|_{k+1/2}$. It therefore concludes that

$$\bar{F}_j|_{k+1/2} = \begin{cases} \lambda_j|_k \cdot v, & v > 0 \\ \lambda_j|_{k+1} \cdot v, & v \leq 0 \end{cases} \tag{3.39}$$

3.8   The Jacobian matrix

From Eq. (3.6), for a set of N ODEs, there will be N^2 dependencies of $\mathbf{F}$ on $\mathbf{G}$ in the Jacobian matrix. By default, MATLAB's stiff solvers calculate the Jacobian matrix using a set of finite difference calculations. However, it is seldom the case that every point in $\mathbf{F}$ is dependent on every point in $\mathbf{G}$ so that the Jacobian matrix is actually very sparse. Identifying the locations of the non-zero points prior to simulation can lead to significant computational savings. The problem outlined thus far uses spatial derivatives up to the 2nd order. On inspection of Eq. (3.25), (3.27), (3.28) and (3.39), only index locations $k-1$, k and $k+1$ are used. At any given time, $\mathbf{F}$ at index k will only be dependent on $\mathbf{G}$ within the spatial range $[k-1, k, k+1]$. In summary, the following can be said:

$$\mathbf{J}|_p = \left.\frac{\partial \mathbf{F}}{\partial \mathbf{G}}\right|_p = 0, \qquad k-1 < p < k+1 \tag{3.40}$$

MATLAB enables the user to specify a Jacobian pattern as a sparse matrix of ones to tell the solver only to evaluate the finite difference calculation at the location denoted 1. For a single ODE of length, N, the Jacobian matrix would appear as a matrix of size $N \times N$ with three diagonals of ones where the leading diagonal represents location k. However, as discussed in Section 3.6.3, there are more than one PDV to solve for. While only one vector, $\mathbf{V}$, is input to the ODE solver and output for the times of interest, $\mathbf{V}$ has $N_{PDV} \times N$ number of elements, where N_{PDV} is the number of PDVs. After input to the ODE solver routine, $\mathbf{V}$ is reshaped for the length of the PDVs. In the case for the equilibrium model in Chapter 5, $\mathbf{V}$ is $3 \times N$ long:

$$\mathbf{V} = \begin{bmatrix} \boldsymbol{P} \\ \boldsymbol{T} \\ \boldsymbol{z}_m \end{bmatrix} \tag{3.41}$$

where

$$\boldsymbol{P} = [P_1, P_2, ..., P_N]^T \tag{3.42}$$

$$\boldsymbol{T} = [T_1, T_2, ..., T_N]^T \tag{3.43}$$

$$\boldsymbol{z}_m = [z_{m1}, z_{m2}, ..., z_{mN}]^T \tag{3.44}$$

In the kinetic model in Chapter 4, however, there are 5 PDVs. In each case, the tri-diagonal ones are still present. An example of the Jacobian pattern used for the equilibrium case is shown in Fig 3.5.
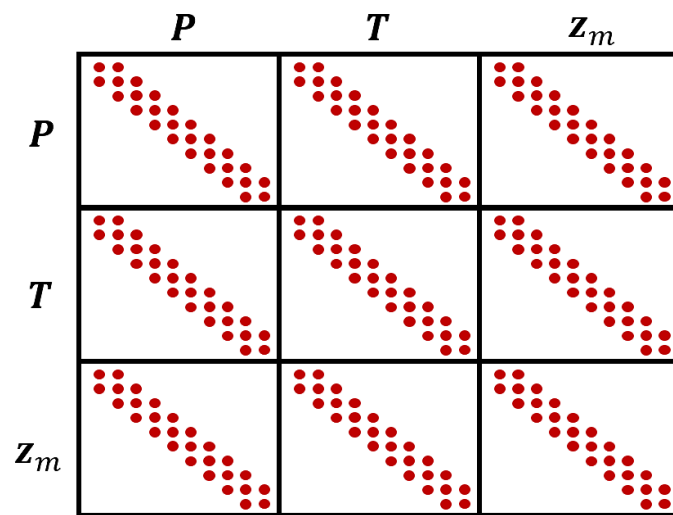
Fig. 3.5: Tri-diagonal Jacobian pattern to be given to the ODE solver for $N = 10$ and $N_{PDV} = 3$.

4. SIMULATING HYDRATE DISSOCIATION IN CORE-SCALE POROUS MEDIA

A version of this chapter is published in the following article:

Hardwick, J. S., & Mathias, S. A. (2018). Masudas sandstone core hydrate dissociation experiment revisited. Chemical Engineering Science, 175, 98-109.

This chapter is a modification of the paper presented above. In the above paper, the salinity induced temperature depression, T_d, is a calibratable parameter. In this chapter, temperature depression can vary with salinity as in Eq. (2.34). This is an improvement on the manuscript because it reduces the number of parameters to optimise for from four to three whilst achieving almost identical simulations to the manuscript.

4.1 Objective

- Simulate the core scale hydrate dissociation experiment presented by Masuda et al. (1999) to verify the kinetic model.

- Compare and contrast modelling results to previous simulation attempts.

- Retrieve real relative permeability parameters from the core scale experiment.

4.2 Highlights

- The numerical model is verified against the Masuda experiment.

- Mathematical material balances can be used to determine hydrate saturation based upon the volumes of gas and water produced.

- The multi-faceted effectiveness of the dataset from Masuda's experiment is clearly demonstrated for numerical simulation benchmarking in the future.

- The Masuda experiment can be simulated using a 1D model.

4.3   Introduction

Many relevant numerical and experimental studies are reported in the literature, but an article of particular significance is that of Masuda et al. (1999), which presents experimental results from four core-scale experiments whereby hydrate in a sandstone is dissociated by depressurization while the outer surface of the core is exposed to a constant temperature "air-bath".

Observed data from the experiments include time-series of gas production, water production, pressure at the core boundary far-field to the fluid outlet and temperature at three different points in the core. Masuda et al. (1999) also present results from one-dimensional numerical simulations of these data from their own numerical simulator. Their model results do a good job of capturing the observed pressure response from the experiments. However, their simulated gas production is significantly delayed as compared to the observed data. Furthermore, their simulated temperature distribution bears little resemblance to the observed data and simulated water production is not reported.

Interestingly, there are at least six published independent attempts to provide and/or improve numerical simulations of these experiments (Nazridoust & Ahmadi, 2007; Liang et al., 2010; Zhao et al., 2012a; Ruan et al., 2012a; Shin, 2014; Chen et al., 2016). In addition to these, there are several articles reporting to explicitly use the Masuda et al. (1999) study as a base case for numerical parameter sensitivity analysis (Gamwo & Liu, 2010; Ruan et al., 2012b; Zhao et al., 2014, 2015, 2016; Song et al., 2016).

Nazridoust & Ahmadi (2007) sought to improve on the numerical work of Masuda et al. (1999) by developing a two-dimensional axisymmetric simulation of the fourth experiment presented by Masuda et al. (1999), hereafter referred to as Run 4. Nazridoust & Ahmadi (2007) performed their simulations using the commercial CFD code, FLUENT. Their simulated results provided a much better match to the observed temperature time-series and gas production data, as compared to those of Masuda et al. (1999). However, their simulated far-field boundary pressure was found to decline much earlier than the observed data. Furthermore, their predicted water production volume was 3.3 times that observed from the experiment.

The differences between the simulated results of Masuda et al. (1999) and Nazridoust & Ahmadi (2007) are unlikely to be due to using a one-dimensional or two-dimensional spatial representation. Note that a two-dimensional representation would delay heat transport from the air-bath to the centre of the core, as compared to a one-dimensional repre-

sentation, suggesting that Nazridoust & Ahmadi (2007) should have forecasted slower gas production as opposed to faster.

Liang et al. (2010) attempted to simulate Masuda's Run 4 data using their own IMPES (implicit pressure-explicit saturation) numerical scheme based on the governing equations for hydrate dissociation simulation previously presented by Sun et al. (2005). Their presented numerical results were similar to those of Nazridoust & Ahmadi (2007). Interestingly, Liang et al. (2010) comment on the inconsistency of the Nazridoust's simulation with Masuda's observed pressure data, but do not present simulated pressure data of their own in this context.

Zhao et al. (2012a) present results from numerical simulations that should have provided identical results to those of Liang et al. (2010). However, their temperature time-series data is very different to both Masuda's observed data and the simulation results from Liang et al. (2010). Of interest is that Zhao et al. (2012a) forecasts an additional delay in the temperature decline due to the heat consumption associated with hydrate dissociation.

Another important aspect of the Masuda et al. (1999) study is that they derive, by calibrating their numerical model to their observed data, an empirical power law to describe permeability reduction as a function of hydrate saturation. The exponent of the power law was found to be 15. The numerical simulations of Nazridoust & Ahmadi (2007) and Liang et al. (2010) also adopted this empirical function. Ruan et al. (2012a) provide an additional attempt to simulate Masuda's Run 4, which yielded very similar results to those of Liang et al. (2010). However, Ruan et al. (2012a) used the same empirical function for permeability reduction but with an exponent of 11.

Shin (2014) attempted to simulate Masuda's Run 4 using an in-house finite element model. Shin (2014) only reports limited information with regards to model parameterization. However, it is clear form their presented results that their model underestimates the amount of gas produced during the experiment by around 3%.

Chen et al. (2016) present simulation results for Masuda's Run 4 but only for the temperature and pressure time-series data. They also compare their numerical results directly with those of Nazridoust & Ahmadi (2007) and Zhao et al. (2012a). All the numerical results look very different. The main difference between the simulation of Chen et al. (2016) and the other numerical studies discussed above is that Chen et al. (2016) applies a constant temperature boundary to the sides of the core whereas the other studies apply adiabatic boundary conditions, in conjunction with a heat production term

associated with heat transfer from the outer constant temperature air-bath.

Of particular interest is that, with the exception of Nazridoust & Ahmadi (2007), none of the numerical studies discussed above report results concerning simulated water production. Furthermore, with the exception of Masuda et al. (1999) and Nazridoust & Ahmadi (2007), none of the above studies comment on their ability to simulate the pressure data at the far-field boundary.

The original intention was to use one of the above modelling studies to benchmark our own numerical simulator for hydrate dissociation. It is possible to closely match the results of Ruan et al. (2012a). However, this can only be achieved by significantly increasing the convective heat transfer coefficient for the heat source associated with the constant temperature air-bath, as compared to the value originally specified by Masuda et al. (1999). Once this is achieved it is found that pressure at the far-field boundary decreases too fast and insufficient gas and water are produced at the outlet, as compared to the experimental observations of Masuda et al. (1999) (recall that Ruan et al. (2012a) does not report their simulated results for water production and pressure).

This chapter presents a set of numerical simulations that better match all facets of the Masuda et al. (1999) data set for benchmarking similar numerical models in the future. In particular, this chapter presents a unified set of governing equations and parameter values, which can be used to provide close correspondence to all the observed experimental data including gas production volume, water production volume, far-field boundary pressure and temperature at the three temperature observation points. This is achieved by designing a new permeability reduction model to account for the presence of hydrate and obtaining relative permeability parameters along with a convective heat transfer coefficient by direct calibration to the observed experimental data.

The outline of this chapter is as follows. First the mathematical equations, associated parameters and numerical solution procedure are presented. A summary of the experimental setup is provided. Calibrated model results are then presented and compared to the experimental data along with seven similar modelling studies from the literature.

4.4   Data and methods

4.4.1   Mathematical methods

Consider the presence of saline water, methane and hydrate in a Berea sandstone which is a classically homogenous and isotropic porous medium. The effects of gravity are assumed negligible. Conservation statements for methane, water and salt components take the form given in Eq. (2.15). This system of equations can be simplified to the following phase conservation statements:

$$\frac{\partial G_g}{\partial t} = -\nabla \cdot \mathbf{F}_g - X_{mh}\frac{\partial G_h}{\partial t} \tag{4.1}$$

$$\frac{\partial G_a}{\partial t} = -\nabla \cdot \mathbf{F}_a - X_{wh}\frac{\partial G_h}{\partial t} \tag{4.2}$$

where, from Eq (2.14):

$$\mathbf{F}_g = -\rho_g\lambda_g\nabla P \tag{4.3}$$

and

$$\mathbf{F}_a = -\rho_a\lambda_a\nabla P \tag{4.4}$$

Furthmore, $\frac{\partial G_h}{\partial t}$ is taken from Eq. (2.28):

$$\frac{\partial G_h}{\partial t} = M_h k_d A_s(P - P_e) \tag{4.5}$$

The accompanying heat transport equation is described by Eq. (2.45):

$$\frac{\partial U}{\partial t} = -\nabla \cdot (\boldsymbol{v}H) + \nabla \cdot (\kappa_E\nabla \cdot T) \tag{4.6}$$

The cylindrical geometry of the core along with the assumption of a homogenous and isotropic porous medium enables an assumption of axial symmetry such that the problem can be solved in terms of normal distance away from the gas outlet, x [L], and radial distance away from the central axis of the cylinder, r [L]. The core is assumed sealed on all sides except for the outlet, which releases fluid due to a fixed pressure. All boundaries are treated as adiabatic with the exception of a convective heat gain boundary due to the surrounding fixed temperature air-bath. Let L [L] and R [L] be the length and radius of the core respectively.

In this way, the system of equations described above can be appropriately constrained by the following initial and boundary conditions:

$$
\begin{array}{llll}
P = P_I, & 0 \le x \le L, & 0 \le r \le R, & t = 0 \\
T = T_I, & 0 \le x \le L, & 0 \le r \le R, & t = 0 \\
S_g = S_{gI}, & 0 \le x \le L, & 0 \le r \le R, & t = 0 \\
S_h = S_{hI}, & 0 \le x \le L, & 0 \le r \le R, & t = 0 \\
P = P_0, & x = 0, & 0 \le r \le R, & t > 0 \\
\dfrac{\partial T}{\partial x} = 0, & x = 0, & 0 \le r \le R,, & t > 0 \\
F_{g,x} = 0, & x = L, & 0 \le r \le R, & t > 0 \\
F_{w,x} = 0, & x = L, & 0 \le r \le R, & t > 0 \\
\dfrac{\partial T}{\partial x} = 0, & x = L, & 0 \le r \le R, & t > 0 \\
F_{g,r} = 0, & 0 \le x \le L, & r = 0, & t > 0 \\
F_{w,r} = 0, & 0 \le x \le L, & r = 0, & t > 0 \\
\dfrac{\partial T}{\partial r} = 0, & 0 \le x \le L, & r = 0, & t > 0 \\
F_{g,r} = 0, & 0 \le x \le L, & r = R, & t > 0 \\
F_{w,r} = 0, & 0 \le x \le L, & r = R, & t > 0 \\
\dfrac{\partial T}{\partial r} = \dfrac{\gamma(T_0 - T)}{\kappa_E}, & 0 \le x \le L, & r = R, & t > 0
\end{array}
\tag{4.7}
$$

where P_I [$ML^{-1}T^{-2}$], T_I [Θ], S_{gI} [-], S_{hI} [-] are the initial values of fluid pressure, temperature, gas saturation and hydrate saturation respectively. P_0 [$ML^{-1}T^{-2}$] is the boundary pressure at the fluid outlet, T_0 [Θ] is the temperature of the air-bath and γ [$MT^{-3}\Theta^{-1}$] is the convective heat transfer coefficient describing heat transfer from the constant temperature air-bath to the boundary of the sandstone core.

4.4.2   Recasting in terms of the primary dependent variables

The four PDEs to be solved for include Eqs. (4.1), (4.2), (4.5) and (4.6). Following Section 3.6.3, it is necessary to recast these equations in terms of fluid pressure, P, temperature, T, and the component mass fractions of water, salt and hydrate in the pore-space, z_w [-], z_s and z_h [-], respectively. The latter can be found from

$$
z_i = \frac{G_i}{F}
\tag{4.8}
$$

where

$$F = G_m + G_w + G_s \tag{4.9}$$

Due to the choice of PDVs, $F = f(P, T, z_w, z_s, z_h)$, it can also be said that

$$\frac{\partial F}{\partial t} = \frac{\partial F}{\partial P}\frac{\partial P}{\partial t} + \frac{\partial F}{\partial T}\frac{\partial T}{\partial t} + \frac{\partial F}{\partial z_a}\frac{\partial z_a}{\partial t} + \frac{\partial F}{\partial z_h}\frac{\partial z_h}{\partial t} \tag{4.10}$$

where

$$z_a = z_w + z_s \tag{4.11}$$

of which the total derivative can be said to be

$$dz_a = dz_w + dz_s \tag{4.12}$$

The necessary derivatives of z_i and F with respect to time are found from Eq. (3.20) and as in (3.21) respectively:

$$\frac{\partial z_i}{\partial t} = \frac{1}{F}\left(\frac{\partial G_i}{\partial t} - z_i\frac{\partial F}{\partial t}\right), \qquad j = w, s, h \tag{4.13}$$

$$\frac{\partial F}{\partial t} = \sum_i \frac{\partial G_i}{\partial t}, \qquad i = m, w, s, h \tag{4.14}$$

X_{sa} can also be found from the PDV's as follows:

$$X_{sa} = \frac{z_s}{z_a} \tag{4.15}$$

Substituting in Eqs. (2.10) and (4.8) into Eq. (4.9) and rearranging further leads to

$$F = \phi\left[\frac{1}{\rho_g} + \left(\frac{1}{\rho_a} - \frac{1}{\rho_g}\right)z_a + \left(\frac{1}{\rho_h} - \frac{1}{\rho_g}\right)z_h\right]^{-1} \tag{4.16}$$

from which it can be shown that the associated partial derivatives of F are obtained as follows:

$$\frac{\partial F}{\partial z_a} = -\frac{F^2}{\phi}\left(\frac{1}{\rho_a} - \frac{1}{\rho_g}\right) \tag{4.17}$$

$$\frac{\partial F}{\partial z_h} = -\frac{F^2}{\phi}\left(\frac{1}{\rho_h} - \frac{1}{\rho_g}\right) \tag{4.18}$$

$$\frac{\partial F}{\partial P} = \frac{F\alpha_E}{\phi} \tag{4.19}$$

$$\frac{\partial F}{\partial T} = -\frac{F\beta_E}{\phi} \tag{4.20}$$

where β_E can be found from Eq. (2.61) and

$$\alpha_E = \phi(S_a\alpha_a + S_g\alpha_g + S_h\alpha_h) + (1-\phi)\alpha_r \tag{4.21}$$

Recall from Section 2.7, the energy conservation statement in Eq. (4.6) can be recast in terms of pressure and temperature to leave

$$\frac{\partial U*}{\partial t} = (\rho C_p)_E \frac{\partial T}{\partial t} - T\beta_E\frac{\partial P}{\partial t} \tag{4.22}$$

$$= -(F_gC_{pg} + F_aC_{pa})\nabla T + (T\beta_g - 1)\nabla\cdot P + (T\beta_a - 1)\nabla\cdot P + \nabla\cdot(\kappa_E\nabla\cdot T) + h_D\frac{\partial G_h}{\partial t}$$

Combining Eqs. (4.10) and (4.22) yields the following pressure and temperature time derivatives:

$$\frac{\partial P}{\partial t} = \frac{\dfrac{\partial F}{\partial t} - \dfrac{\partial F}{\partial z_a}\dfrac{\partial z_a}{\partial t} - \dfrac{\partial F}{\partial z_h}\dfrac{\partial z_h}{\partial t} - \dfrac{1}{\rho_E C_{pE}}\dfrac{\partial F}{\partial T}\dfrac{\partial U^*}{\partial t}}{\dfrac{\partial F}{\partial P} + \dfrac{\beta_E T}{\rho_E C_{pE}}\dfrac{\partial F}{\partial t}} \tag{4.23}$$

and

$$\frac{\partial T}{\partial t} = \frac{1}{\rho_E C_{pE}}\left(\frac{\partial U^*}{\partial t} + \beta_E T\frac{\partial P}{\partial t}\right) \tag{4.24}$$

4.4.3   The convective heat transfer coefficient, λ

The need for a convective heat transfer coefficient, within the boundary conditions provided in Eq. (4.7), comes about due to the presence of a rubber sleeve around the sandstone core during the experiment (Masuda et al., 1999). Let Q_0 [ML^{2}T^{-3}] be the heat flux from the outside of the sandstone core, found from

$$Q_0 = -2\pi RL\kappa_E\frac{\partial T}{\partial r}\bigg|_{r=R} = 2\pi RL\gamma(T - T_0) \tag{4.25}$$

Assuming heat conduction within the rubber sleeve to be quasi-steady stae (Crank , 1975)

$$Q_0 = \frac{2\phi L\kappa_{rs}(T - T_0)}{\ln[(R + t_{rs})/R]} \tag{4.26}$$

where κ_{rs} [MLT$^{-3}\Theta^{-1}$] and t_{rs} [L] are thermal conductivity and the thickness of the rubber sleeve, respectively.

It follows that

$$\gamma = \frac{\kappa_{rs}}{R \ln[(R + t_{rs})/R]} \qquad (4.27)$$

According to Zarr et al. (2017) the thermal conductivity of rubber ranges between 0.016 and 2.3 W m^{-1} K^{-1}. Masuda et al. (1999) do not report the thickness of the rubber sleeve. However, for a different but similar set of experiments, Konno et al. (2008) state that they used a rubber sleeve of 10 mm thickness. Assuming a sleeve thickness of 10 mm leads to values ranging between 1.90 and 272.7 W m^{-2} K^{-1}, respectively. Masuda et al. (1999) report that they calculated a value of of 16.6 W m^{-2} K^{-1}. However, given the uncertainty about the thermal conductivity of rubber, it would be appropriate to treat it as a calibration parameter in this context. Note that Chen et al. (2016) applied values ranging between 80 W m^{-2} K^{-1} and 400 W m^{-2} K^{-1} for their sensitivity analysis in this context.

4.4.4 Relative permeability

A significant challenge for Masuda et al. (1999) was to find a model that produced most of the gas within 200 min whilst maintaining a significant pressure difference between the fluid outlet and the opposite end of the core throughout the experiment (see Fig. 7 of Masuda et al. (1999)). The boundary at the opposite end of the core (i.e., at $x = L$) is hereafter referred to as the far-field boundary. The model of Masuda et al. (1999) did a good job of sustaining pressure at the far-field boundary but the gas production takes an additional 120 min as compared to the observed data (see Fig. 7 of Masuda et al. (1999)). In contrast, the model of Nazridoust & Ahmadi (2007) produced all the gas on time but the far-field pressure time-series was completely different to that observed during the experiment (see Figs. 8 and 10 of Nazridoust & Ahmadi (2007)). The models of Liang et al. (2010), Ruan et al. (2012a), Zhao et al. (2012a) and Shin (2014) also did a good job of getting the time of gas production right. However, these studies do not report on simulated pressure. Chen et al. (2016) only report on simulated temperatures, in the context of Masuda's experiment. However, the far-field pressures reported from their associated sensitivity analysis were only able to simulate a sustained far-field boundary pressure difference for 125 min. The pressure at the far-field boundary is sustained throughout Masuda's experiment because this represents the final point at which all the hydrate is dissociated, which happens at the end of the gas production period. Subsequently, a step-wise relative permeability model was inferred which reconciled the observed slow pressure decline through the core with the fast gas production at the outlet. The so-named

Critical Threshold model was introduced in Section 2.5.1, Eq. (2.23):

$$k_{ra} = k_{rf} \left(\frac{S_a - S_{ar}}{1 - S_{ar} - S_{gc}} \right)^{n_a}, \qquad\qquad S_{ar} \leq S_a \leq 1 - S_{gc} \qquad (4.28)$$

$$k_{rg} = k_{rf} \left(\frac{S_g - S_{gc}}{1 - S_{ar} - S_{gc}} \right)^{n_g}, \qquad\qquad S_{gc} \leq S_g \leq 1 - S_{ar}$$

$$kk_{rf} = \begin{cases} k_c, & S_h > S_{hc} \\ k_c + (k - k_c)\left(\frac{S_{hc} - S_h}{S_{hc}} \right), & 0 \leq S_h \leq S_{hc} \end{cases}$$

4.4.5 Auxiliary parameters

Thermophysical properties of brine water, methane and hydrate are the same as described in Section 2.8. Rock properties are as follows: $\rho_R = 2600$ kgm^{-3}, $\kappa_R = 8.8$ W m^{-1} K^{-1} and $C_{pR} = 2010$ J kg^{-1}K^{-1}. All properties required to describe the dissociation kinetics in Eq. (4.5) are handled using the parameterisations set out in Section 2.6. In this study, a Berea sandstone is invoked which has a mean pore radius of 67200 Å (Shi et al., 2011). Following Turner et al. (2005), such radii lies greatly above the threshold (600 Å) at which pore geometry does not affect hydrate stability. It is therefore safe to assume that the gravely sand samples used by Wright et al. (1999) would also lie above this threshold. Therefore, in spite of a lack of salt induced temperature depression data for a Berea sandstone with saline water, the reference values are extracted from Fig. 2.5 where $T_{d,ref} = 1.5$ and $x_{sa,ref} = 0.005$.

Note that, following Masuda et al. (1999), Nazridoust & Ahmadi (2007), Liang et al. (2010), Ruan et al. (2012a), Zhao et al. (2012a), Shin (2014) and Chen et al. (2016), Knudsen diffusion is not explicitly considered. Such an effect is unlikely to be significant here because of the relatively high pressures associated with Masuda's experiments. However, for lower pressure scenarios further consideration should be given in this respect.

4.4.6 Numerical solution

The spatial domain is discretized into N_x equally-spaced points in the x direction and N_r equally-spaced points in the r direction using Godunov's method (Leveque, 1992). The numerical solution procedures presented in Chapter 3 are used. For all the simulations conducted in this article, $N_x = 20$ and $N_r = 10$. Axisymmetric problems often require extensive grid refinement in the radial direction at the origin when applying source terms

at $r = 0$. However, in this case, the $r = 0$ boundary is a zero flux boundary, which by its nature is very smooth. Consequently, the model quickly achieves numerical convergence with increasing grid resolution. Numerical convergence was verified by comparing results from additional simulations using $N_x = 40$ and $N_r = 10$, and $N_x = 20$ and $N_r = 20$. Results from the three sets of simulations were found to be virtually identical.

4.4.7 Summary of the experiments

The experiments of Masuda et al. (1999) involved emplacing a mixture of water, methane and hydrate within a cylindrical core of a Berea sandstone. A fixed pressure reduction was applied at one end of the core to form a fluid outlet. All other external surfaces were sealed. The core was heated during the experiment using a constant temperature air-bath. Pressure was monitored at the opposite end to the fluid outlet. Temperature was monitored at three different points within the core, T_1; T_2 and T_3. According to Fig. 1 of Masuda et al. (1999), T_1; T_2 and T_3 are located 225 mm, 150 mm and 75 mm from the fluid outlet. The volume of methane produced from the core was recorded throughout the experiment. The total volume of water produced was recorded at the end of the experiment. Masuda et al. (1999) repeated the experiment on the same core four times but with different initial and boundary pressures. The various measured parameters associated with these four runs are listed in Table 4.1. The length of the core was $L = 30$ cm. The cross-sectional area of the core was $\pi R^2 = 20.3$ cm^2. The absolute permeability of the core was $k_0 = 96.7 \times 10^{-15}$ m^2. The porosity of the core was $\phi = 0.182$. The methane gas was close to pure. The water had a salinity of 10 ppt. A schematic diagram of the experimental setup is presented in Fig. 4.1.

Run number	1	2	3	4
Air-bath temperature, T_0 (K)	275.15	275.15	275.15	275.15
Initial temperature, T_I (K)	275.45	275.45	275.45	275.45
Outlet pressure, P_0 (MPa)	3.28	3.14	2.99	2.84
Initial pressure, P_I (MPa)	3.75	3.70	3.57	3.75
Initial hydrate saturation, S_{hI} (-)	0.354	0.394	0.425	0.443
Initial water saturation, S_{aI} (-)	0.455	0.308	0.348	0.351
Volume of gas produced, V_{gP} (Scm^3)	7276	8096	8734	9106
Volume of water produced, V_{aP} (Scm^3)	6.3	6.5	12.0	11.7

Tab. 4.1: Summary of the four hydrate dissociation experiments according to Masuda et al. (1999). Note that the initial gas saturation, $S_{gI} = 1 - S_{aI} - S_{hI}$.
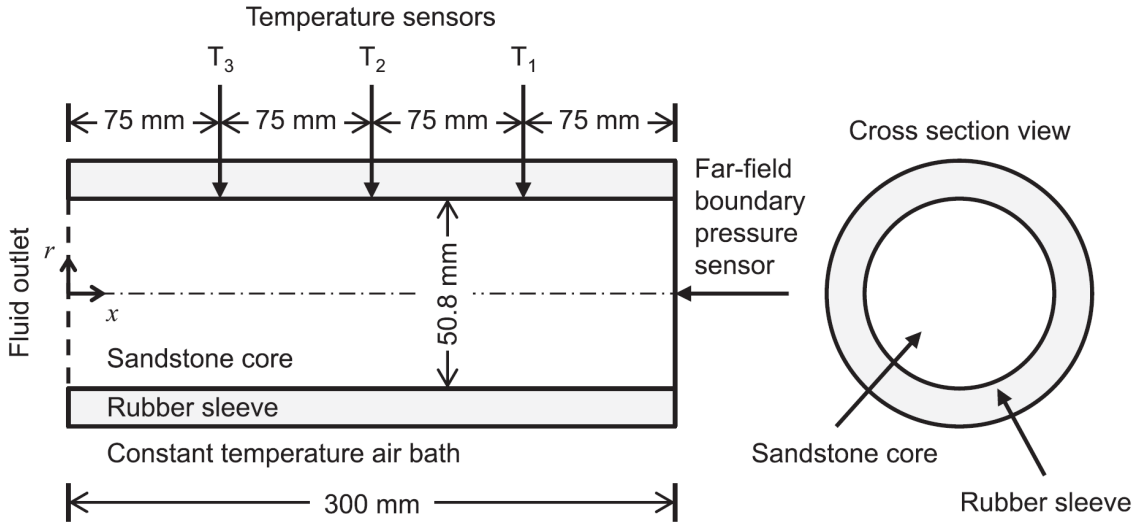
Fig. 4.1: Schematic diagram of experimental setup (adapted from Fig. 1 of Masuda et al. (1999)).

4.4.8   Initial hydrate saturations revisted

The initial saturations of water, gas and hydrate were determined by material balance. Of note is that Masuda et al. (1999) report that they were concerned that the estimated hydrate saturations were significantly underestimated. It is possible to explore this further by performing a material balance based on the data provided in Table 4.1. The following mass balance equations can be used to relate the mass of water and methane residing in the pore-space of the sandstone core at the beginning and end of the experiment with the masses of water and methane produced from the core by the end of the experiment:

$$m_{whI} + m_{aI} = m_{a0} + m_{aP} \tag{4.29}$$

$$m_{mhI} + m_{gI} = m_{g0} + m_{gP} \tag{4.30}$$

where m_{whI} [M] is the mass of water initially present in hydrate within the pore-space, m_{aI} [M] is the mass of liquid water initially present within the pore-space, m_{a0} [M] is the mass of liquid water present within the pore-space at the end of the experiment and m_{aP} [M] is the mass of liquid water produced from the core by the end of the experiment. The symbols in Eq. (4.30) represent identical items to those in Eq. (4.29) but for methane as opposed to water. Note that:

$$m_{whI} = \frac{(M_h - M_m)\rho_h V_T S_{hI}}{M_h} \tag{4.31}$$

$$m_{mhI} = \frac{M_m \rho_h V_T S_{hI}}{M_h} \tag{4.32}$$

$$m_{aI} = \rho_{aI} V_T S_{aI} \tag{4.33}$$

$$m_{gI} = \rho_{gI} V_T S_{gI} \tag{4.34}$$

where V_T is the total pore volume, found from

$$V_T = \pi R^2 L \phi \tag{4.35}$$

and S_{hI} [-], S_{aI} [-] and S_{gI} [-] represent the initial saturations of hydrate, water and gaseous methane and ρ_{aI} [ML^{-3}] and ρ_{gI} [ML^{-3}] are the densities of water and methane in the sandstone core at the initial pressure and temperature conditions. Furthermore,

$$m_{aP} = V_{aP} \rho_{aP} \tag{4.36}$$

$$m_{gP} = V_{gP} \rho_{gP} \tag{4.37}$$

where V_{aP} [L^3] and V_{gP} [L^3] are the volumes of water and methane produced from the core at standard conditions and ρ_{aP} [ML^{-3}] and ρ_{gP} [ML^{-3}] are the densities of water and methane gas at standard conditions (0.1014 MPa and 15.56 ^oC), respectively. At the end of the experiment it can be assumed that there is no hydrate present such that

$$m_{g0} = \left(V_T - \frac{m_{a0}}{\rho_{a0}} \right) \rho_{g0} \tag{4.38}$$

and ρ_{a0} [ML^{-3}] and ρ_{g0} [ML^{-3}] are the densities of water and methane in the sandstone core at the final pressure and temperature conditions. Substituting Eqs. (4.30)-(4.37) into Eq. (4.29), Eq. (4.29) can be solved to obtain the volume of gas:

$$V_{gP} = \left[\left(\frac{\rho_h}{M_h} (\rho_{g0}(M_h - M_g) + \rho_{a0} M_g) - \rho_{a0} \rho_{gI} \right) S_{hI} + \rho_{a0} \rho_{gI}(1 - S_{aI}) + \rho_{g0} \rho_{wI} S_{aI} \right.$$

$$\left. - \rho_{g0} \rho_{a0} - \frac{\rho_{g0} \rho_{aP} V_{aP}}{V_T} \right] \frac{1}{\rho_{a0} \rho_{gP}} \tag{4.39}$$

or for the volume of water produced:

$$V_{aP} = \left[\left(\frac{\rho_h}{M_h} (\rho_{g0}(M_h - M_g) + \rho_{a0} M_g) - \rho_{a0} \rho_{gI} \right) S_{hI} + \rho_{a0} \rho_{gI}(1 - S_{aI}) + \rho_{g0} \rho_{aI} S_{aI} \right.$$

$$\left. - \rho_{g0} \rho_{a0} - \frac{\rho_{a0} \rho_{gP} V_{gP}}{V_T} \right] \frac{1}{\rho_{g0} \rho_{aP}} \tag{4.40}$$

or alternatively, Eq. (4.29) can be solved for initial hydrate saturation:

$$S_{hI} = \left[\rho_{g0}\rho_{a0} - \rho_{a0}\rho_{gI}(1 - S_{aI}) - \rho_{g0}\rho_{aI}S_{aI} + \frac{1}{V_T}\left(\rho_{g0}\rho_{aP}V_{aP} + \rho_{a0}\rho_{gP}V_{gP}\right) \right] \quad (4.41)$$

$$\times \left[\frac{\rho_h}{M_h}\left(\rho_{g0}(M_h - M_g) + \rho_{a0}M_g\right) - \rho_{a0}\rho_{gI} \right]^{-1} \quad (4.42)$$

Table 4.2 provides the values of initial, final and produced water and methane densities for the four experimental runs, based on the pressures and temperatures provided in Table 4.1, along with estimates of volumes of gas produced, volumes of water produced and initial hydrate saturations calculated using Eqs. (4.39)-(4.41) respectively. The fact that the V_{gP} values in Table 4.2 are much lower than those observed by Masuda et al. (1999), reported in Table 4.1, confirms Masuda et al.'s concern that their estimates of S_{hI} are too low. In fact, forcing their reported values of V_{gP} and S_{hI} together, from Table 4.1, leads the material balance to forecast negative values for water production, V_{aP}. It is proposed that the new estimates of S_{hI} in Table 4.2 are more accurate because they are calculated directly from the observed gas and water production values given in Table 4.1, using Eq. (4.41) and are used for all the numerical simulations conducted hereafter.

Run number	1	2	3	4
Initial methane density, ρ_{gI} (kgm^{-3})	28.72	28.30	27.22	28.72
Final methane density, ρ_{g0} (kgm^{-3})	24.87	23.72	22.51	21.30
Standard methane density, ρ_{gP} (kgm^{-3})	0.6789	0.6789	0.6789	0.6789
Initial water density, ρ_{aI} (kgm^{-3})	1008	1008	1008	1008
Final water density, ρ_{a0} (kgm^{-3})	1005	1005	1005	1005
Standard water density, ρ_{aP} (kgm^{-3})	1002	1002	1002	1002
Volume of gas produced, V_{gP} (Scm^3)	6413	7271	7642	8099
Volume of water produced, V_{aP} (Scm^3)	-17.3	-17.2	-21.0	-20.5
Initial hydrate saturation, S_{hI} (-)	0.403	0.441	0.487	0.501

Tab. 4.2: Material balance study, determined using the pressures and temperatures in Table 4.1 and thermophysical properties from Lemmon et al. (2013) for gas and Batzle & Wang (1992) for brine water. Following Ahmed (2001), standard conditions are assumed to be 0.1014 MPa and 15.56^{o}C. Initial water density has a salinity of 10ppt following Masuda et al. (1999). Final water density and standard water density is assumed to have a salinity of 5ppt based upon preliminary runs. It is important to note that although it is not possible to determine the exact salinity of the final and produced water from the data provided, the calculated V_{gP}, V_{aP} and S_{hI} do not vary significantly with water densities using salinities between 1ppt and 10ppt. The volume of gas produced was calculated using Eq. (4.39) with all other parameters taken from Table 4.1. The volume of water produced was calculated using Eq. (4.40) with all other parameters taken from Table 4.1. The initial hydrate saturation was calculated using Eq. (4.41) with all other parameters taken from Table 4.1.

4.4.9 Model calibration and validation

Following the discussion above, their remain four unknown model parameters: S_{ar}; n_a; n_g and S_{gc} from the relative permeability functions and the convective heat transfer coefficient, γ. There is a known strong correlation between S_{ar} and n_a; and S_{gc} and n_g. Therefore, S_{ar} and S_{gc} is hereafter fixed to 0.1 and 0.0 respectively. Values for the remaining three parameters: n_a; n_g and γ, have been obtained by calibrating the mathematical model above to the observed gas production, water production, pressure and temperature data from Run 4 of Masuda et al. (1999). Run 4 is selected for comparison with earlier modelling studies (Nazridoust & Ahmadi, 2007; Liang et al., 2010; Ruan et al., 2012a; Zhao et al., 2012a; Shin, 2014; Chen et al., 2016). Calibration is achieved by minimizing the following objective function:

$$\varepsilon = \varepsilon_g + \varepsilon_a + \varepsilon_p + \varepsilon_{T1} + \varepsilon_{T2} + \varepsilon_{T3} \tag{4.43}$$

where

$$\varepsilon_y = \frac{\sum_{x=1}^{N_y}(\sigma_{yx} - m_{yx})^2}{\sum_{x=1}^{N_y}(\sigma_{yx} - \bar{\sigma}_{yx})^2} \tag{4.44}$$

and σ_{yx} are observed experimental data, m_{yx} are corresponding model results, N_y are the number of observed data, $\bar{\sigma}_{yx}$ represents the mean of the observed data, and $y = g$ for the gas production volume, $y = a$ for the final produced water volume, $y = p$ for the far-field boundary pressure, and $y = T1; T2$ and $T3$ for the observed temperature data at 225 mm, 150 mm and 75 mm from the fluid outlet, respectively. The above objective function is minimized using MATLAB's nonlinear minimization routine, FMINSEARCH. Based on the above discussion and some preliminary simulation results, seed values (for FMINSEARH) for n_a, n_g and γ are taken to be 1, 1.8 and 48 respectively. As a validation exercise, Masuda et al.'s Run 2 and Run 3 are subsequently simulated using the calibrated model parameters from Run 4.

4.5　Results and discussion

Following calibration of the above mathematical model to the observed data from Masuda's Run 4, it was found that optimal values of n_a, n_g and γ were 0.93, 2.15 and 55.4 $Wm^{-2}\,K^{-1}$, respectively. These values do not necessarily represent global optimal values but rather parameter values that achieve a local minimum of the objective function around the chosen seed values. The resulting simulated output from the model is compared to the observed data from Run 4 in Fig. 4.2. In Fig. 4.2a it can be seen that the model predicts the correct amount of final gas and water production volumes. Simulated gas production, as compared to the observed experimental data, is delayed by around 20 min. In Fig. 4.2b, the model can be seen to accurately predict most of the far-field boundary pressure data, with the exception of a mini-peak in pressure observed in the experimental data at around
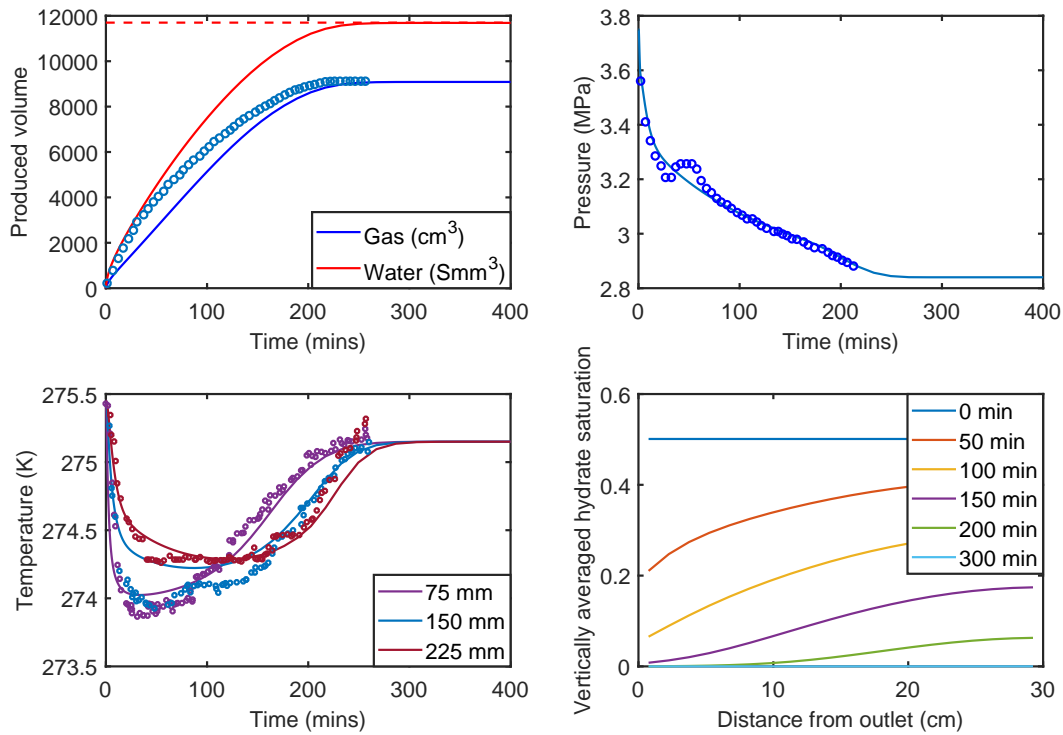
Fig. 4.2: Comparison of the numerical model with observed data extracted from Run 4 of Masuda et al. (1999). The solid lines are from the numerical model. The ciruclar markers are the experimental observed data from Masuda et al. (1999). (a) Comparison of fluid production volumes. The dashed red line represents the experimental observed final volume of water produced. Note that Masuda et al. (1999) do not report transient water production data. (b) Comparison of far-field boundary pressures. (c) Comaprison of temperature data at 225 mm, 150 mm, 75 mm from the outlet boundary, respectively. All temperature measurements are assumed to be taken from the outside boundary of the cylindrical core. (d) Simulated vertically averaged hydrate saturation plotted at different times as a function of distance from the fluid outlet. Note that 1 S cm^3 and 1 mm^3 imply volumes of 1 cm^3 and 1 mm^3, respectively, at standard conditions.
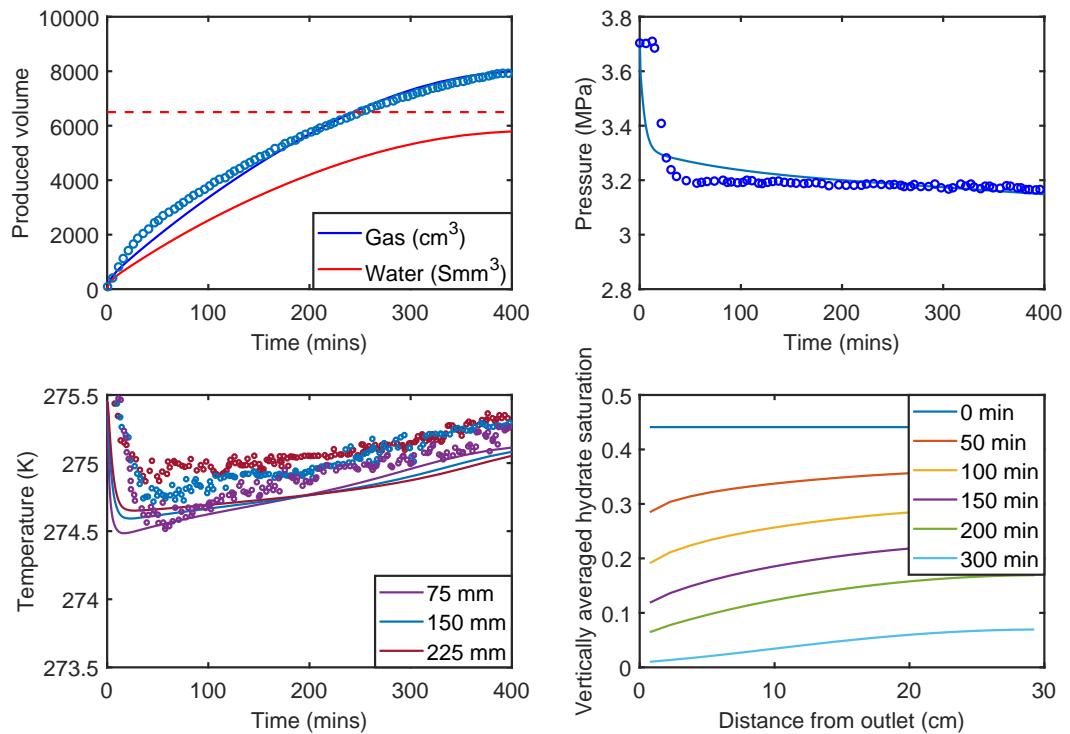
Fig. 4.3: Same as Fig. 4.2 but for Run 2 of Masuda et al. (1999).

50 min. The pressure evolution is over-predicted by the model in the first 25 minutes and this effect, coupled with the mini-peak in pressure build-up, can explain the poor calibration to the first 150 mins of the gas production curve. In Fig. 4.2c, it can be seen that the model does a good job of predicting the temperature data at 225 mm and 75 mm from the fluid outlet. However, there are some significant discrepancies between the model and observed data during the first 100 min at 150 mm from the fluid outlet. Fig. 4.2d shows simulated vertically averaged hydrate saturation as a function of distance from the outlet. Here it can be seen that, even at 200 min, for distances from the outlet greater than 5 cm, the hydrate saturation is well over the threshold value of 10^{-4} used in the permeability model (recall Eq. (2.23)). Also of note is that all the hydrate is dissociated after 300 min.

Figs. 4.3 and 4.4 compare model and experimental results for Masudas Runs 2 and 3, respectively, both using optimal model parameters derived from the Run 4 calibration, described above. For both Runs 2 and 3, the model underestimates far-field boundary pressure during the early part of the experiments and then overestimates the pressure in the latter part of the experiments. Water production is underestimated in Runs 2 and 3 by around 15 %, however, for both Run 2 and 3, the model does an excellent job of predicting the gas production data. Run 3 does a good job of predicting the temperature
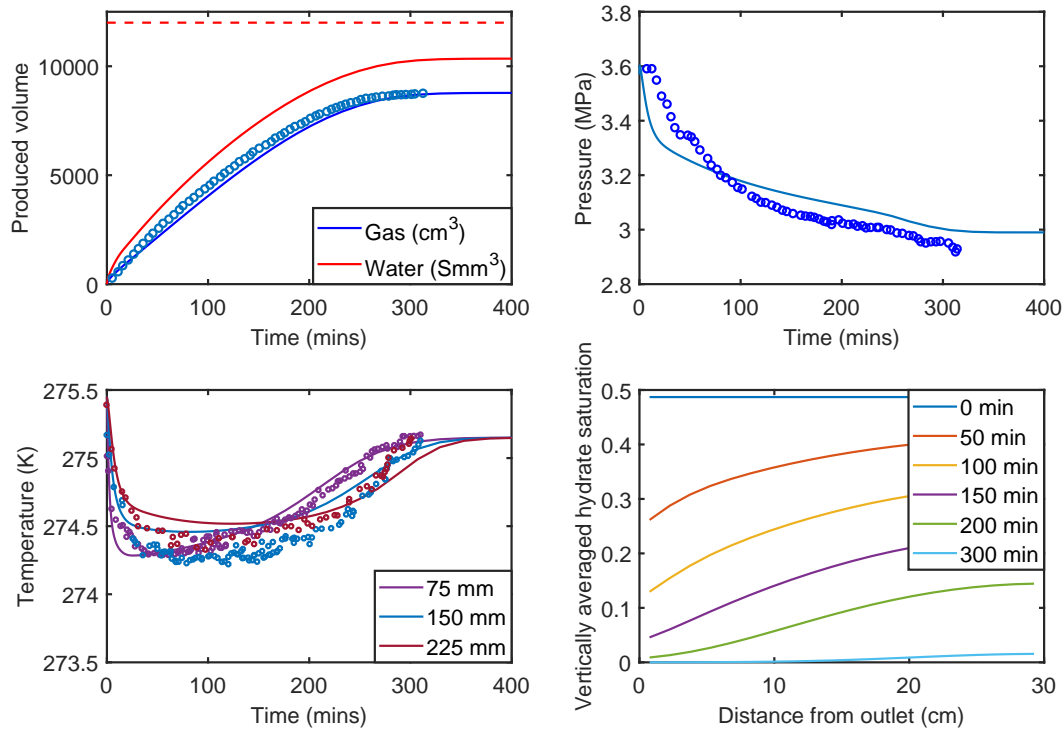
Fig. 4.4: Same as Fig. 4.2 but for Run 3 of Masuda et al. (1999).

data whereas Run 2 underpredicts temperature at all three observation points. It was found that only minor improvement was achieved by directly calibrating the model to Runs 2 and 3 independently as shown in Appendix B.

4.5.1   Comparison with earlier modelling studies

Fig. 4.5c compares the simulated far-field boundary pressure for Run 4 in this study with model results from Masuda et al. (1999), Nazridoust & Ahmadi (2007) and Chen et al. (2016). Recall that the other modelling studies discussed above do not report their simulated far-field boundary pressure data. The model results correspond much better to the observed far-field boundary pressure data as compared to previous reported modelling attempts. The simulated pressure data from Chen et al. (2016) reaches steady state almost 200 min too early. The simulated pressure data from Nazridoust & Ahmadi (2007) has the wrong shape. The simulated pressure data from Masuda et al. (1999) is closer to the observed data as compared to Nazridoust & Ahmadi (2007). However, Masuda's model overestimates the pressure throughout. Fig. 4.5a and b compare the simulated gas production for Run 4 with model results from Masuda et al. (1999), Nazridoust & Ahmadi (2007), Shin (2014), Liang et al. (2010), Ruan et al. (2012a) and Zhao et al. (2012a).
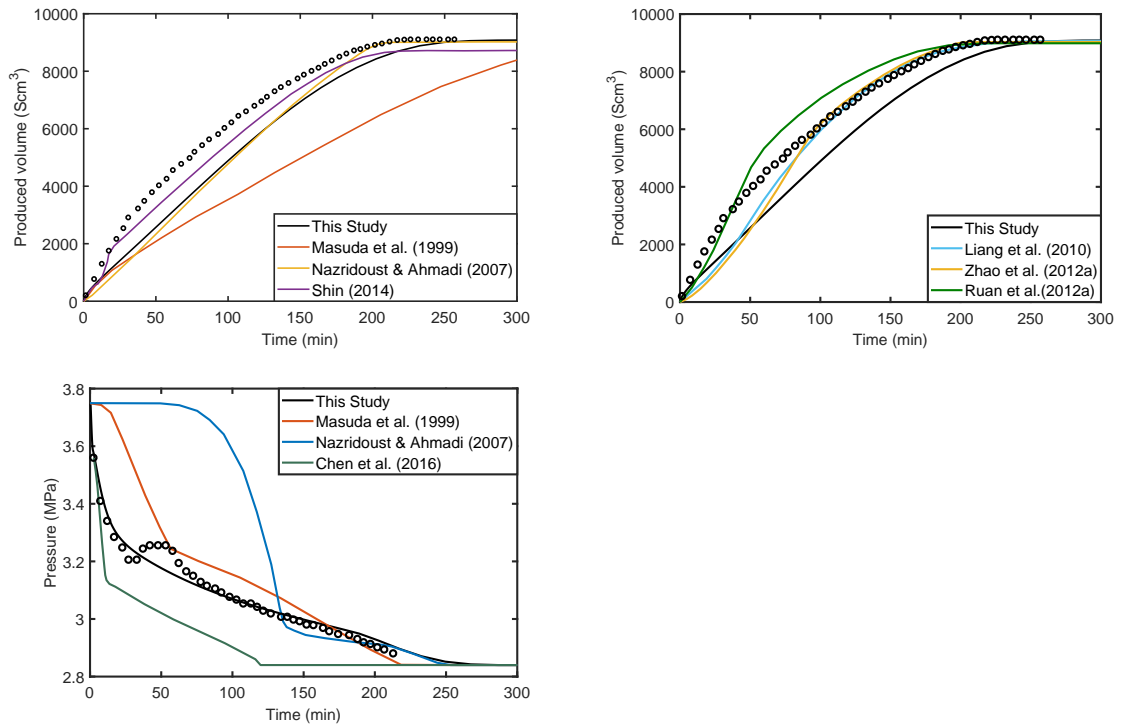
Fig. 4.5: Comparison of far-field boundary pressure and gas production volume from different model studies in the literature along with the current study. The circular markers are the observed data extracted from Masuda et al. (1999). (a)-(b) Comparison of gas production simulations. (c) Comparison of the far-field boundary pressure simulation results. Note that 1 Scm^3 implies a volume of 1 cm^3 at standard conditions.

Recall that Chen et al. (2016) does not report their simulated gas production data. The simulations of Masuda et al. (1999) and Shin (2014) produce around 3 % less gas than the other modelling studies. Furthermore, gas production from Masuda et al. (1999) is significantly delayed as compared to the observed data and the other modelling studies. The simulated gas production is very similar to the results generated by Nazridoust & Ahmadi (2007); both studies lead to slightly delayed gas production during the first 200 min. Masuda's simulation is able to predict a sustained difference between far-field and fluid outlet boundaries due to their relative permeability and permeability configuration. However, the consequence is that simulated gas production is delayed. In this new model, the sustained pressure difference and the relatively fast gas production is sustained by assuming that the bulk permeability is reduced to a 100th of its original value until hydrate saturation is below 10^{-4} (recall the discussion in Section 4.4.4). This enables porous media free of hydrate to provide significantly high mobility to both gas and water whilst simultaneously blocking off the far-field boundary from the outlet boundary pressure until (almost) all the hydrate has dissociated throughout the core. The modelling studies of Liang et al. (2010), Ruan et al. (2012a) and Zhao et al. (2012a) are worth considering

together because all three of these works were developed by the same research group at Dalian University of Technology. The simulated gas production data presented by Liang et al. (2010) and Zhao et al. (2012a) are almost identical. They both lead to slightly delayed gas production during the first 100 min and then closely follow the observed experimental data thereafter. The simulated gas production of Ruan et al. (2012a) is around 20 min faster than the observed experimental data. The reason for this is that both Liang et al. (2010) and Zhao et al. (2012a) adopt a permeability reduction exponent of 15 (recall the discussion in Section 4.4.4) whereas Ruan et al. (2012a) adopt an exponent of 11, allowing the gas to be more mobile earlier on in the experiment.

Fig. 4.6 compares all the modelling studies in terms of their ability to simulate the experimentally observed temperature data within the core at 225 mm, 150 mm and 75 mm from the fluid outlet, hereafter referred to as T_1; T_2 and T_3, respectively. All the modelling studies, with the exception of Shin (2014) and Chen et al. (2016) are able to correctly predict that T_3 declines before T_2, which declines before T_1. And similarly, that T_3 rises before T_2, which rises before T_1. In contrast, Shin (2014) predicts that T_1; T_2 T_3 decline together (Fig. 4.6f) and Chen et al. (2016) predicts that T_1 rises before T_2 and T_2 rises before T_3 (Fig. 4.6g). Interestingly, the simulated temperature responses of Liang et al. (2010) and Ruan et al. (2012a) are almost identical (compare Fig. 4.6c and d). In contrast, the temperature results from Zhao et al. (2012a) have a very different shape, which is difficult to explain (Fig. 4.6e). All the previous studies, with the exception of Chen et al. (2016), predict that either the minimum values of T_1; T_2 and T_3 are virtually the same or that the minimum of T_1 is less than that of T_2 and that of T_2 is less than that of T_3 (Fig. 6a, and f). Only the Chen et al. (2016) study is able to correctly predict that the minimum of T_3 is less than that of T_2 and the minimum of T_2 is less than that of T_1, as observed from Masudas experimental data (Fig. 4.6g). However, this is at the expense of getting the order of timing wrong, as discussed in the paragraph above. This modelling study presented here represents a considerable improvement in model performance because the simulation gets the order correct for both the timing and the minimum values (Fig. 4.6h).

Unfortunately, none of the above studies report simulated water production volumes, with the exception of Nazridoust & Ahmadi (2007). However, assuming that these studies used the initial saturation values given in Table 4.1, taking their final simulated gas production volumes and substituting these into Eq. (4.40) leads to negative values of water production volumes, as was seen in Table 4.2. This would suggest that either they used different initial saturations or their equation of state for methane and water are consider-
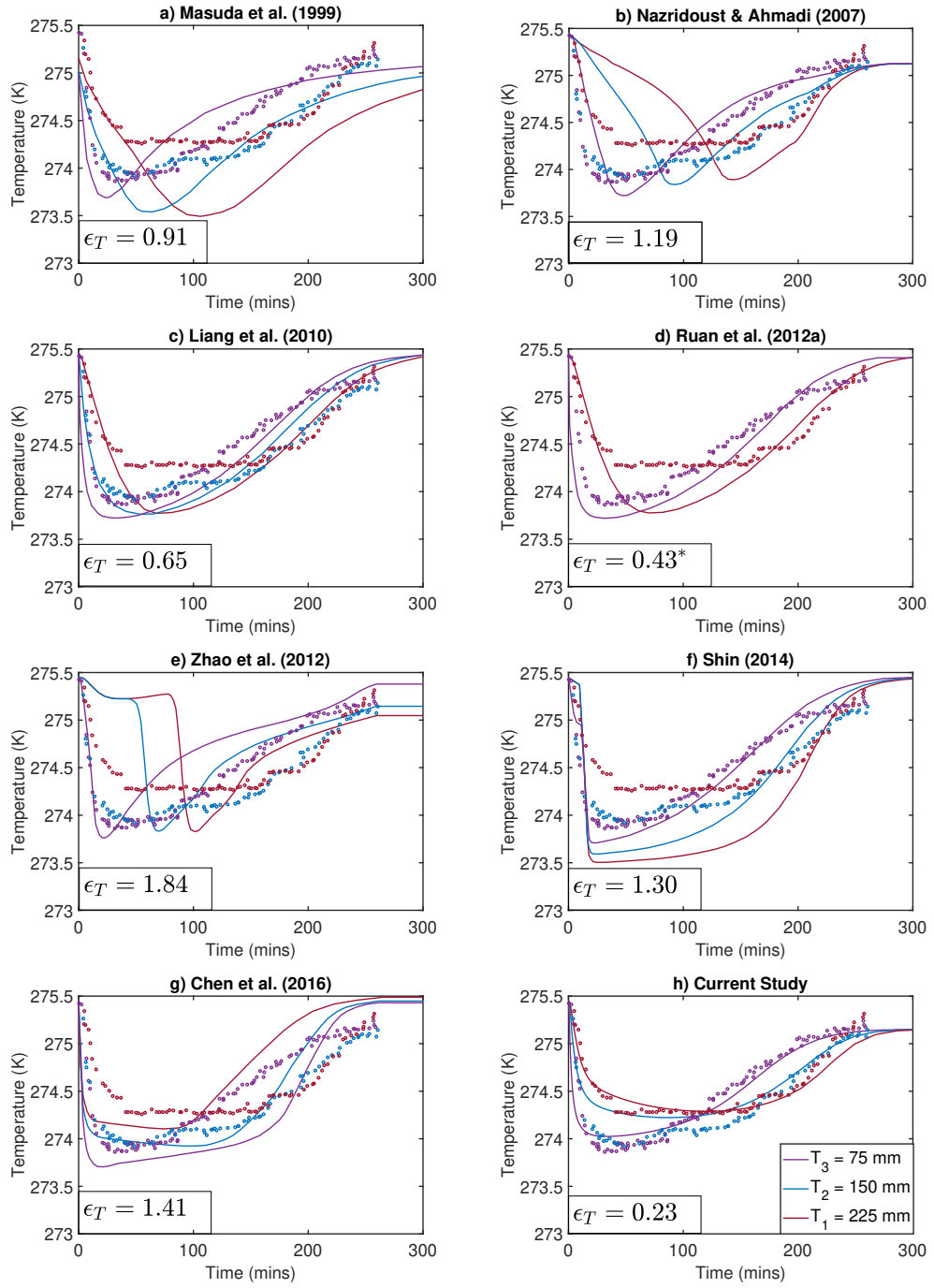
Fig. 4.6: Comparison of temperature data from different model studies in the literature along with our current study. The circular markers are the observed data extracted from Masuda et al. (1999). $\epsilon_T = \epsilon_{T1} + \epsilon_{T2} + \epsilon_{T3}$ from Eq. (4.44). Note that for the study by Ruan et al. (2012a) although ϵ_T is low, they only report on T_1 and T_3.

ably different to those provided by Lemmon et al. (2013) and Batzle & Wang (1992). In this way it can be understood that this modelling study provides a significant improvement in model performance compared to earlier studies in terms of correspondence to the various observed experimental data reported previously by Masuda et al. (1999). With a single set of parameters, reasonable simulations have been provided for gas production, water production, temperature and boundary pressure for Masuda et al.'s Runs 2, 3 and

4 (note that experimental data for Run 1 is not currently available and so this scenario has not been studied further). The reasons for the improvements on earlier work are as follows: (1) improved estimates of the initial hydrate saturation have been determined by applying a material balance to the experimental data; (2) the exponents of the water and gas relative permeability (n_a and n_g) and the convective heat transfer coefficient γ have been obtained by calibrating the mathematical model to the experimental data from Run 4; (3) a Critical Threshold permeability model is applied, which assumes permeability is significantly reduced when hydrate saturation is greater than a critical threshold value (recall Section 2.5.1, Eq. (2.23)).

4.6   Summary and conclusions

The objective of this study was to provide a set of numerical simulations that better match the various data presented by Masuda et al. (1999) from three hydrate dissociation experiments conducted in a cylindrical core (Run 2, Run 3 and Run 4). The observed experimental data include gas production volume, water production volume, far-field boundary pressure and temperature at three temperature observation points. With the exception of Masuda et al. (1999) and Nazridoust & Ahmadi (2007), previous modelling studies in the literature only looked at gas production and temperature. With the exception of Nazridoust & Ahmadi (2007), none of the modelling studies in the literature discussed the ability of their models to simulate the observed water production. A significant issue concerning the numerical simulations of Masuda et al. (1999) are that whilst their model did a good job of simulating the far-field boundary pressure, gas production was significantly delayed. In the current study it was found that a Critical Threshold permeability model was required to reconcile these two observations, whereby permeability for hydrate saturations $\geq 10^{-4}$ is assumed to be 100 times less than the bulk permeability. This enables porous media free of hydrate to provide significantly high mobility to both gas and water whilst simultaneously blocking off the far-field boundary from the outlet boundary pressure until almost all the hydrate has dissociated throughout the core. In addition to providing good correspondence between the gas production and far-field boundary pressure data, the model is also found to be effective at simulating the water production and temperature data, improving considerably on the seven earlier modelling studies found in the literature ((Masuda et al., 1999; Nazridoust & Ahmadi, 2007; Liang et al., 2010; Ruan et al., 2012a; Zhao et al., 2012a; Shin, 2014; Chen et al., 2016)). The reasons for the improvements on earlier work were as follows: (1) improved estimates of the initial hydrate saturation were determined by applying a material balance to the experimental data; (2) the relative permeability parameters and a convective heat transfer coefficient were obtained by calibrating the mathematical model to the experimental data from Run 4; and (3) an alternative permeability model was applied to specifically reconcile a relatively fast gas production with a relatively slow far-field boundary pressure response. An important subsidiary finding from this work is that permeability is significantly reduced in the presence of very low hydrate saturations. The results from this analysis suggest that this phenomenon can be approximated in numerical models using a simple step function (see Section 2.5.1). It has also been shown that the initial hydrate saturations for hydrate

dissociation experiments, such as those of Masuda et al. (1999), can be determined by material balance using experimentally observed volumes of produced gas and water. Finally, the multi-faceted effectiveness of the dataset from Masudas experiment is clearly demonstrated for numerical simulation benchmarking in the future.

4.7   1D modelling of the Masuda experiment

In this section, 1D and 2D cases of the core-scale modelling in the previous sections are compared. While simulating more spatial dimensions brings the model closer to reality, doing so adds extra complexity to the governing equations and consequently increases the computation time. Therefore, where possible, a 1D model is preferable.

Recall that the radius of the Berea sandstone core ($R = 2.54$ cm) is much less than the length of the core ($L = 30$ cm). As the location of the fluid outlet is at one end of the core while the other end is sealed, and given the core is much longer than it is wide, the pressure gradient dominates in the lengthwise direction. Subsequently, fluid migration in the lengthwise direction is significantly more compared to fluid movement in the radial direction. Furthermore, given the relatively thin core, it would be anticipated that heat transfer from the surrounding temperature air bath fluxes to the centre of the core is fast.

The only difference to the mathematical model in the 1D case is the treatment of heat transfer between the core and the surrounding air bath. In a 1D case, the ambient heat flux is applied across every cell in the discretised domain and not just on the radial boundary. From Eq. (4.25), the heat flux from outside of the sandstone core, Q_0, is added to the energy conservation statement as a source term and is calculated as follows

$$Q_0 = \frac{\gamma(T_0 - T)}{\pi \kappa_E R^2} \qquad (4.45)$$

where γ is the convective heat transfer coefficient, T_0 is the temperature of the surrounding air bath, T is temperature and κ_E is an effective thermal conductivity.

4.7.1   Comparisons between the 1D and 2D model

Aside for Q_0 described above, the same mathematical model described in Chapter 4 is used. The calibrated parameters for n_g (=2.15), n_a (=0.93) and γ (=55.4) are also used. The 2D and 1D model are graphically compared against each other. From Fig. 4.7 the two models can be seen to be in good agreement with each other, with the exception of some minor discrepancies. In Fig. 4.7a, the 1D model overpredicts the amount of water produced. However, increasing γ from 55.4 to 60 makes the two models indistinguishable suggesting the difference is caused by the effects of heat flow into the core. It is clear that the experiment by Masuda et al. (1999) can be adequately simulated using a 1D model.
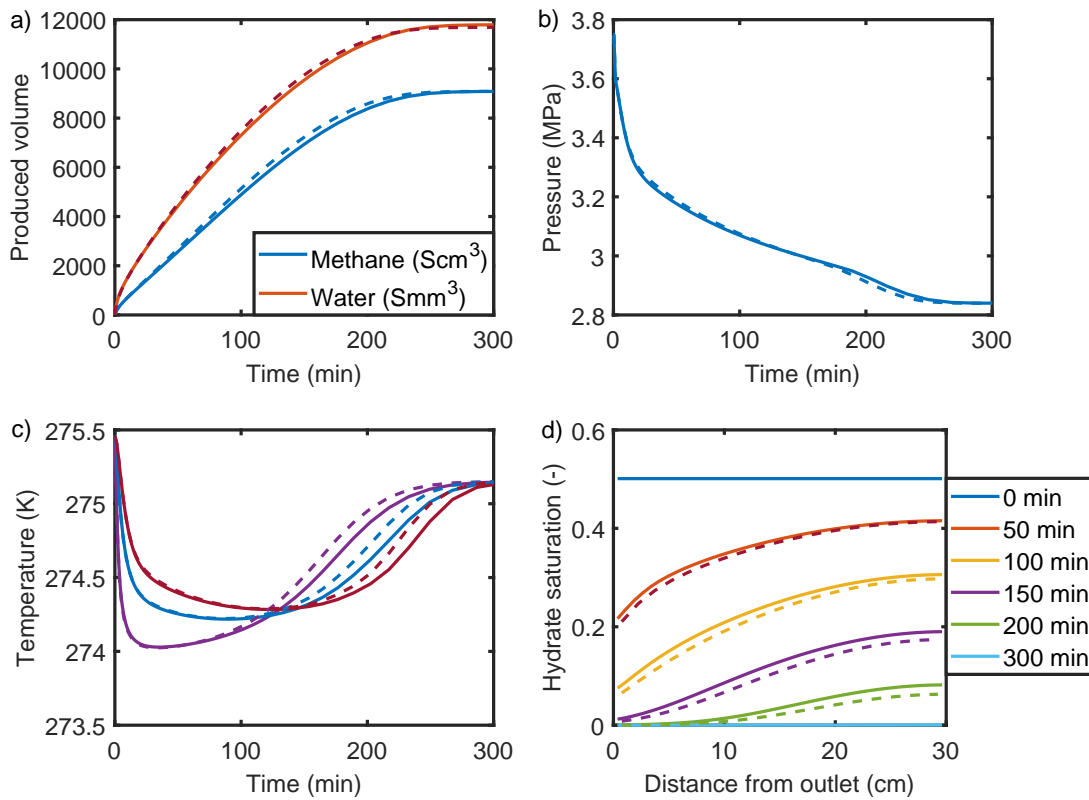
Fig. 4.7: Comparison between the 2D and 1D model against the experimental data from Masuda experiment. Solid lines are the 1D model response and dashed lines are the 2D model response.

5. COMPARISON OF EQUILIBRIUM AND KINETIC MODELS

5.1   Objective

- Introduce hydrate equilibrium theory.

- Present the mathematical model behind the equilibrium approach.

- Verify the equilibrium model.

5.2   Highlights

- A unique equilibrium model using persistent primary dependent variables is presented.

- The equilibrium model can be verified against the kinetic model and is appropriate for simulating regional scale problems.

5.3 Introduction

Chapter 2 presented and discussed the numerous controls that must be considered when simulating the methane hydrate dissociation problem. Building on from this, Chapter 4 validated the mathematical handling of these controls against multiple experimental datasets given by Masuda et al. (1999). The chapter also calibrated the model against the experimental dataset to constrain unknown variables such as the relative permeability exponents. Furthermore, Chapter 4 confirmed that the Method of Lines approach is a suitable way to simulate core scale methane hydrate dissociation.

The objective of this research hereon is to apply these discoveries to the regional scale methane hydrate dissociation problem. However, there are conceptual and numerical limitations to using the kinetic model at larger scales. Conceptually, the kinetic model is only formulated for the dissociation of hydrate, however in nature, formation can also occur. Numerically, the kinetic model is highly dependent upon the scale simulated. Consider Fig. 5.1. At a small scale, a discretised domain can describe the dissociation zone using many nodal points, where a nodal point is the centre of a cell. On upscaling, discretised with the same number of points, the active dissociation zone becomes a numerical singularity, or a sharp step-wise front. For a flowing material, this limitation is manifested through the dimensionless Peclét number, χ [-], which is the ratio of the advection rate, a [LT^{-1}], to the dispersion rate, b [$L^2 T^{-1}$]. It can be shown that to ensure numerical stability, $\chi < 2$, and the Peclét number can be defined as follows

$$\chi \equiv \frac{a\Delta x}{b} < 2 \tag{5.1}$$

where Δx is the distance between two adjacent nodal points. When discussing the Peclét number, Δx is commonly referred to as the "Characteristic Length". Recall that the 1st order Godunov upwinding scheme described in Section 3.7.2.2 can solve the Riemann problem associated with sharp discontinuities for flowing material and is used to handle the step in relative permeability as methane and water is produced at the dissociation front. In this way, by taking a first order approach, the numerical stability associated with the Peclét number is maintained. Considering the hydrate dissociation process, the dissociation rate is augmented by the difference between pressure, P, and equilibrium pressure, P_e, at the same nodal point and therefore behaves as a rate dependent point source. Alternatively, the dissociation zone could be considered as a set of dispersion rates, b. As
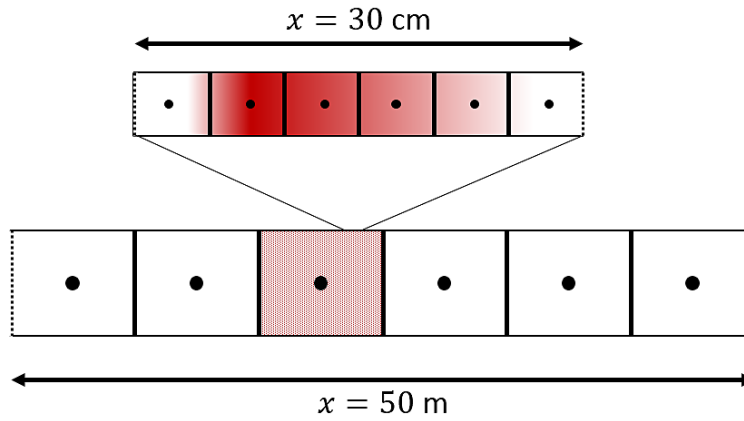
Fig. 5.1: Schematic highlighting the numerical issues associated with the scale dependency of the hydrate dissociation front. The red shaded region is the active dissociation zone.

the scale increases, *b* reduces and may violate the stability criterion in Eq. (5.1). Godunov's upwinding scheme cannot be applied to the hydrate conservation statement in Eq. (2.28) because $\frac{\partial G_h}{\partial t}$ is a singularity with no spatial terms either side of the dissociation zone which can be appropriately chosen (like $\mathbf{F}_{k\pm1/2}$ in Eq. (3.34)).

One solution to enable the dissociation front to be solvable over the numerical grid at larger scales (Fig. 5.1) is by reducing Δx. While this improves the resolution of the model it also significantly increases the computation time. An alternative solution is to remove the term generating the numerical instability by reformulating the problem. In the context of hydrate dissociation, this is commonly done by removing the hydrate kinetics in $\frac{\partial G_h}{\partial t}$ (Eq. (2.28)).

Commonly, numerical models that do not include the hydrate kinetics are called "Equilibrium models". Here, dissociation and formation is treated solely as a transfer of components between the available phases when crossing the hydrate-methane-water phase equilibrium boundary. For instance, if methane and water components exist above the three-phase equilibrium pressure, hydrate is formed. Depending on which component is in excess, there will be one free mobile phase. However, when methane and water components exist below the three-phase equilibrium pressure, the methane and water are in their free states.

In fact, the equilibrium model is a simplification of a kinetic model and under large scale thermal stimulation and depressurisation, the two models are very similar (Kowalsky & Moridis, 2007). Furthermore, Gamwo & Liu (2010) and Liu & Gamwo (2012) showed that kinetic models converge to the equilibrium model by increasing the intrinsic dissociation constant, k_{d0}. Although ignoring the kinetic controls at a laboratory scale will provide vastly different results (Kowalsky & Moridis, 2007), at regional scales, the

dissociation zone is so thin relative to the scale that it may be modelled as a point or line source, as shown in Fig. 5.2. Another important difference between the two models is that the equilibrium model can straightforwardly handle both dissociation and formation of hydrate, whereas the kinetic model requires different kinetic equations to describe the formation of hydrate. Furthermore, while the kinetic model can initially begin in disequilibrium, with co-existing gas, liquid and hydrate, the equilibrium model cannot do this by definition.

Generally researchers consider the kinetic model more realistic for core scale simulations and avoid using it for regional scale models due to how computationally expensive the approach can be (Kowalsky & Moridis, 2007; Gamwo & Liu, 2010; Moridis, 2012). Furthermore, by removing the hydrate kinetics, there is one less equation to solve for as the hydrate phase can be determined in terms of methane and water components purely.

Some equilibrium models are available in open source software such as HydrateResSim (Gamwo & Liu, 2010) and T+H (Moridis, 2012). Such models apply a numerical technique called the "Primary Variable Switch Method" (PVSM) (Gamwo & Liu, 2010; Liu & Gamwo, 2012; Moridis, 2012). This approach circumvents the problem arising from the singularity in $\frac{\partial G_h}{\partial t}$ (see Fig. 5.1) by solving for different primary dependent variables (PDVs), either side of the dissociation front, depending upon the availability of phases. Typically, these models employ switching criteria at each Newton-Raphson iteration time-step to determine the PDVs to solve for. However, such an approach is limited by the lowest possible Δt across the grid. Furthermore, the Newton-Raphson root finding algorithm uses the simplest implicit Euler time-stepping scheme. Hence, their solutions are limited to the 1st order of accuracy and requires significantly lower Δt compared to multi-step, multi-order schemes (recall the discussion in Section 3.6).

It is the desire of this study to use the numerical scheme presented in Chapter 3 in order to take advantage of the higher order, high accuracy solvers which is not possible by using a 1st order Newton Raphson and PVSM approach. No existing hydrate model under equilibrium assumptions uses persistent PDVs such that much of this chapter is dedicated to deriving and testing a unique equilibrium model in terms of persistent PDVs.

Finally, the equilibrium model is verified against the kinetic model, which in turn was verified in Chapter 4 against the Masuda experimental dataset.
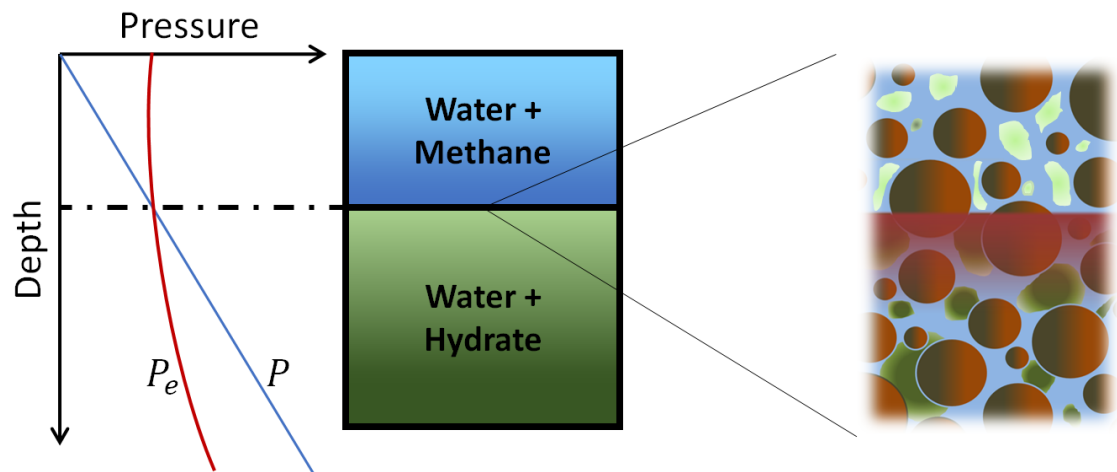
Fig. 5.2: A schematic emphasising how the equilibrium model is a special case of the kinetic model.

5.4   Equilibrium model

5.4.1   Mathematical model

Consider the presence of saline water, methane and hydrate in a rock which is a classically homogenous and isotropic porous medium. Unlike described in the kinetic model, as hydrate forms or dissociates, the concentration of salt is assumed not to change due to the assumption that, at a regional scale, brine water is in sufficient abundance and readily replenished.

The relevant component mass statements are given by Eq. (2.15) and can be simplified to:

$$\frac{\partial G_m}{\partial t} = -\mathbf{F}_m \tag{5.2}$$

$$\frac{\partial G_w}{\partial t} = -\mathbf{F}_w \tag{5.3}$$

Note that in the equilibrium model, there is no explicit satement of $\frac{\partial G_h}{\partial t}$ unlike in the kinetic model in Eq. (2.28). An accompanying heat transfer equation is given in Eq. (2.45):

$$\frac{\partial U}{\partial t} = -\nabla \cdot (\mathbf{v}H) + \nabla \cdot (\kappa_E \nabla \cdot T) \tag{5.4}$$

5.4.2   Recasting in terms of the primary dependent variables

The PDVs are chosen to be z_m, P and T. As with the approach outlined in Section 3.6.3, it follows that

$$z_w = \frac{G_w}{F} \tag{5.5}$$

$$z_m = \frac{G_m}{F} \tag{5.6}$$

where in this case

$$F = G_w + G_m \tag{5.7}$$

Given that P, T and z_m are the PDVs, the following can also be said

$$\frac{\partial F}{\partial t} = \frac{\partial F}{\partial P}\frac{\partial P}{\partial t} + \frac{\partial F}{\partial T}\frac{\partial T}{\partial t} + \frac{\partial F}{\partial z_m}\frac{\partial z_m}{\partial t} \tag{5.8}$$

The governing partial derivatives of z_m and F with respect to time is provided by Eq. (3.20) and Eq. (3.21) respectively:

$$\frac{\partial z_m}{\partial t} = \frac{1}{F}\left(\frac{\partial G_m}{\partial t} - z_m \frac{\partial F}{\partial t}\right) \tag{5.9}$$

$$\frac{\partial F}{\partial t} = \frac{\partial G_m}{\partial t} + \frac{\partial G_w}{\partial t} \tag{5.10}$$

The terms F, $\frac{\partial F}{\partial P}$, $\frac{\partial F}{\partial T}$ and $\frac{\partial F}{\partial z_m}$ are to be determined in the following work.

Recall that the amount of hydrate formed is limited by the abundance of free gas, herein referred to as the gas limited case ($S_g = 0$) or the abundance of water, herein referred to as the water limited case ($S_a = 0$). Subsituting Eq. (2.10) into Eq. (5.5) (5.6) assuming a water limited and gas limited case respectively produces the following discontinuous function for the hydrate saturation, S_h:

$$S_h = \begin{cases} \frac{F z_w}{\phi X_{wh}\rho_h}, & S_a = 0 \\ \frac{F z_m}{\phi X_{mh}\rho_h}, & S_g = 0 \end{cases} \tag{5.11}$$

Equating both limiting cases to find the singularity at which point hydrate formation moves from a water limited to a gas limited case gives

$$z_m - X_{mh} = 0 \tag{5.12}$$

The gas limited case can then be expressed as

$$z_m - X_{mh} < 0 \tag{5.13}$$

and the water limited case can also be expressed as

$$z_m - X_{mh} > 0 \tag{5.14}$$

Recall that under equilibrium conditions, hydrate dissociation and formation is treated as a phase change when methane and water components cross the three-phase equilibrium

boundary. The following can be stated:

$$S_h = \begin{cases} 0, & P < P_e \\ S_h, & P > P_e \end{cases} \tag{5.15}$$

Combining Eqs. (5.11), (5.13), (5.14) and (5.15), the hydrate saturation can be stated as

$$S_h = \frac{F\Psi_P}{\phi\rho_h}\left(\frac{z_m(1-\Psi_{zm})}{X_{mh}} + \frac{z_w\Psi_{zm}}{X_{wh}}\right) \tag{5.16}$$

where Ψ_P and Ψ_{zm} are Heaviside step-function as follows

$$\Psi_P = H(P - P_e) \tag{5.17}$$

$$\Psi_{zm} = H(z_m - X_{mh}) \tag{5.18}$$

Applying Eq. (5.17) and Eq. (5.18) does not remove the singularity associated with the dissociation front as they are spatially discontinuous functions which do not enable the whole system to be definable in terms of a persistent set of PDVs. Therefore smooth, spatially continuous approximations to these Heaviside functions are instead used as follows:

$$\Psi_P = \frac{1}{2}\left(1 + \tanh\left[\frac{A(P - P_e)}{P_e}\right]\right) \tag{5.19}$$

$$\Psi_{zm} = \frac{1}{2}\left(1 + \tanh\left[\frac{B(z_m - X_{mh})}{X_{mh}}\right]\right) \tag{5.20}$$

where A [-] and B [-] control the precision of the approximation to their respective heaviside step-functions and P_e is taken from Eq. (2.32).

Expanding out Eqs. (5.5) and (5.6), and substituting in Eq. (5.16), expressions for S_a and S_g can be found respectively:

$$S_a = \frac{F}{\phi\rho_a}\left[z_w - X_{wh}\Psi_P\left(\frac{z_m(1-\Psi_{zm})}{X_{mh}} + \frac{z_w\Psi_{zm}}{X_{wh}}\right)\right] \tag{5.21}$$

$$S_g = \frac{F}{\phi\rho_g}\left[z_m - X_{mh}\Psi_P\left(\frac{z_m(1-\Psi_{zm})}{X_{mh}} + \frac{z_w\Psi_{zm}}{X_{wh}}\right)\right] \tag{5.22}$$

As $S_h + S_a + S_g = 1$, F can now be expressed in terms of the PDVs:

$$F = \phi\left[\frac{z_m}{\rho_g} + \frac{z_w}{\rho_a} - \Psi_P\left(\frac{X_{mh}}{\rho_g} + \frac{X_{wh}}{\rho_a} - \frac{1}{\rho_h}\right)\left(\frac{z_m(1-\Psi_{zm})}{X_{mh}} + \frac{z_w\Psi_{zm}}{X_{wh}}\right)\right]^{-1} \tag{5.23}$$

From which it can be shown that the associated partial derivatives of F are obtained as follows:

$$\frac{\partial F}{\partial P} = \frac{F}{\phi}\left[\alpha_E + \frac{\phi S_h 2A(1-\Psi_P)}{P_e}\left(\frac{X_{mh}\rho_h}{\rho_g} + \frac{X_{wh}\rho_h}{\rho_a} - 1\right)\right] \tag{5.24}$$

$$\frac{\partial F}{\partial T} = -\frac{F}{\phi}\left[\beta_E + \frac{\phi S_h 2AP(1-\Psi_P)}{P_e^2}\frac{dP_e}{dT}\left(\frac{X_{mh}\rho_h}{\rho_g} + \frac{X_{wh}\rho_h}{\rho_a} - 1\right)\right] \tag{5.25}$$

$$\frac{\partial F}{\partial z_m} = -\frac{F^2}{\phi}\left[\frac{1}{\rho_g} - \frac{1}{\rho_a} - \Psi_p\left(\frac{X_{mh}}{\rho_g} + \frac{X_{wh}}{\rho_a} - \frac{1}{\rho_h}\right)\left(\frac{1}{X_{mh}}\left[1 - \Psi_{zm} - z_m\frac{d\Psi_{zm}}{dz_m}\right]\right.\right.$$
$$\left.\left. + \frac{1}{X_{wh}}\left[z_w\frac{d\Psi_{zm}}{dz_m} - \Psi_{zm}\right]\right)\right] \tag{5.26}$$

where the effective isothermal compressibility, α_E, can be found from

$$\alpha_E = \phi(S_g\alpha_g + S_a\alpha_a + S_h\alpha_h) + (1-\phi)\alpha_R \tag{5.27}$$

and the effective volumetric expansivity, β_E, is as in Eq. (2.61). From Eq. (5.20), $\frac{d\Psi_{zm}}{dz_m}$ can be found:

$$\frac{d\Psi_{zm}}{dz_m} = \frac{B}{2X_{mh}}\text{sech}^2\left(\frac{a(z_m - X_{mh})}{X_{mh}}\right) \tag{5.28}$$

As in Section 2.7, the energy conservation statement in Eq. (5.4) can be recast in terms in terms of P and T by considering all the available phases as follows

$$\frac{\partial U*}{\partial t} = (\rho C_p)_E\frac{\partial T}{\partial t} - T\beta_E\frac{\partial P}{\partial t} \tag{5.29}$$

$$= -(F_g C_{pg} + F_a C_{pa})\nabla T + (T\beta_g - 1)\nabla\cdot P + (T\beta_a - 1)\nabla\cdot P + \nabla\cdot(\kappa_E\nabla\cdot T) + h_D\frac{\partial G_h}{\partial t}$$

Recall that the equilibrium model does not explicitly state $\frac{\partial G_h}{\partial t}$ such it is necessary to define this term by alternative means for the energy conservation statement in Eq. (5.29). Given that $G_h = \phi\rho_h S_h$, from Eq. (5.16) the following can be said

$$G_h = F\Psi_p\left(\frac{z_m(1-\Psi_{zm})}{X_{mh}} + \frac{z_w\Psi_{zm}}{X_{wh}}\right) = G_{hi}\cdot\Psi_p \tag{5.30}$$

In this way, $\frac{\partial G_h}{\partial t}$ can be found by partial differentiation of the above expression:

$$\frac{\partial G_h}{\partial t} = G_{hi}\frac{\partial\Psi_p}{\partial t} + \Psi_p\frac{\partial G_{hi}}{\partial t} \tag{5.31}$$

where

$$\frac{\partial \Psi_P}{\partial t} = \frac{\partial \Psi_P}{\partial P} \frac{\partial P}{\partial t} + \frac{\partial \Psi_P}{\partial T} \frac{\partial T}{\partial t} \qquad (5.32)$$

The partial derivatives $\frac{\partial \Psi_P}{\partial P}$ and $\frac{\partial \Psi_P}{\partial T}$ can be found by partially differentiating Eq. (5.19) to provide

$$\frac{\partial \Psi_P}{\partial P} = \frac{A}{2P_e} \operatorname{sech}^2 \left(\frac{A(P - P_e)}{P_e} \right) \qquad (5.33)$$

and

$$\frac{\partial \Psi_P}{\partial T} = -\frac{AP}{2P_e^2} \frac{dP_e}{dT} \operatorname{sech}^2 \left(\frac{A(P - P_e)}{P_e} \right) \qquad (5.34)$$

The term $\frac{dP_e}{dT}$ can easily be retrieved by differentiating the equilibrium pressure, $P_e(T)$ as found in Eq. (2.66). Furthermore, $\frac{\partial G_{hi}}{\partial t}$ can be derived from Eq. (5.30):

$$\frac{\partial G_{hi}}{\partial t} = \frac{G_{hi}}{F} \frac{\partial F}{\partial t} + F \left[\left(\frac{(1 - \Psi_{zm})}{X_{mh}} - \frac{\Psi_{zm}}{X_{wh}} \right) + \left(\frac{z_w}{X_{wh}} - \frac{z_m}{X_{mh}} \right) \frac{\partial \Psi_{zm}}{\partial z_m} \right] \frac{\partial z_m}{\partial t} \qquad (5.35)$$

Of which, $\frac{\partial z_m}{\partial t}$, $\frac{\partial F}{\partial t}$ and $\frac{\partial \Psi_{zm}}{\partial z_m}$ are known from Eqs. (5.9), (5.10) and (5.28) respectively. The energy conservation statement for the equilibrium problem from Eq. (5.29) can now be re-defined in terms of its primary dependent variables as follows

$$\frac{\partial U^*}{\partial t} = C \frac{\partial T}{\partial t} + D \frac{\partial P}{\partial t} + E \qquad (5.36)$$

where

$$C = (\rho C_p)_E - h_D G_{hi} \frac{\partial \Psi_p}{\partial T} \qquad (5.37)$$

$$D = -T\beta_E - h_D G_{hi} \frac{\partial \Psi_p}{\partial P} \qquad (5.38)$$

$$E = -h_D \Psi_p \frac{\partial G_{hi}}{\partial t} \qquad (5.39)$$

Combining Eqs. (5.8) and (5.36) then yields expressions for $\frac{\partial P}{\partial t}$ and $\frac{\partial T}{\partial t}$:

$$\frac{\partial P}{\partial t} = \frac{\frac{\partial F}{\partial t} - \frac{\partial F}{\partial z_m} \frac{\partial z_m}{\partial t} + \frac{1}{C} \frac{\partial F}{\partial T} \left(E - \frac{\partial U^*}{\partial t} \right)}{\frac{\partial F}{\partial P} - \frac{D}{C} \frac{\partial F}{\partial T}} \qquad (5.40)$$

and finally

$$\frac{\partial T}{\partial t} = \left(\frac{\partial F}{\partial t} - \frac{\partial F}{\partial z_m} \frac{\partial z_m}{\partial t} - \frac{\partial F}{\partial P} \frac{\partial P}{\partial t} \right) \left(\frac{\partial F}{\partial T} \right)^{-1} \qquad (5.41)$$

5.4.3 Sensitivity analysis of A and B

It would be preferable to use the exact Heaviside functions in Eq. (5.17) and (5.18) to describe the phase transfer between components across the three-phase equilibrium boundary and the transition between limiting cases respectively at large scales. However, while the solution scheme in this study has its advantages as described in Chapter 3, it does not lend itself to time-dependent singularities when compared to schemes like the PVSM. The PVSM instead handles these problems by solving either side of the dissociation front with different mass conservation statements. In this study, smooth approximations of the Heaviside functions are used in Eq. (5.19) and (5.20), which include scaling parameters, *A* and *B* respectively.

Scaling parameter *A* controls the degree of smoothness as phases cross the three-phase equilibrium boundary - effectively the dissociation and formation rate. Scaling parameter *B* instead controls the smoothing across the limiting cases. There is an inherent scale dependency of *A* and *B* because higher resolutions could allow for better approximations to the Heaviside functions. Therefore, for each problem simulated, scales and resolutions, an appropriate choice for *A* and *B* would need to be tested prior to final simulation runs. Formulating a precise relationship between resolution and these scaling parameters is beyond the scope of this thesis.

The sensitivity of both parameters are discussed in the following section with the aim to choose appropriate values to be used to validate the equilibrium model.

5.4.3.1 Scaling parameter B

Recall that for equilibrium conditions, if hydrate has formed and stable above the three-phase equilibrium pressure, there can be only one free mobile phase. The parameter *B* should therefore be large enough so that the transition between water limited and gas limited cases is virtually step-wise. From Fig. 5.3a, a value of $B = 50$ can be seen to achieve this with a difference between the smoothed approximation and the Heaviside step of $< 10^{-2}$. Note that the core scale model in Chapter 4 does not exhibit a change in the limiting case during the simulation.

5.4.3.2 Error calculation

The "Mean absolute normalised component error" $\bar{\delta}_i$ (%), is used to assess the choice of *A* in the following sections and the regional scale modelling in Section 6.1. It can be
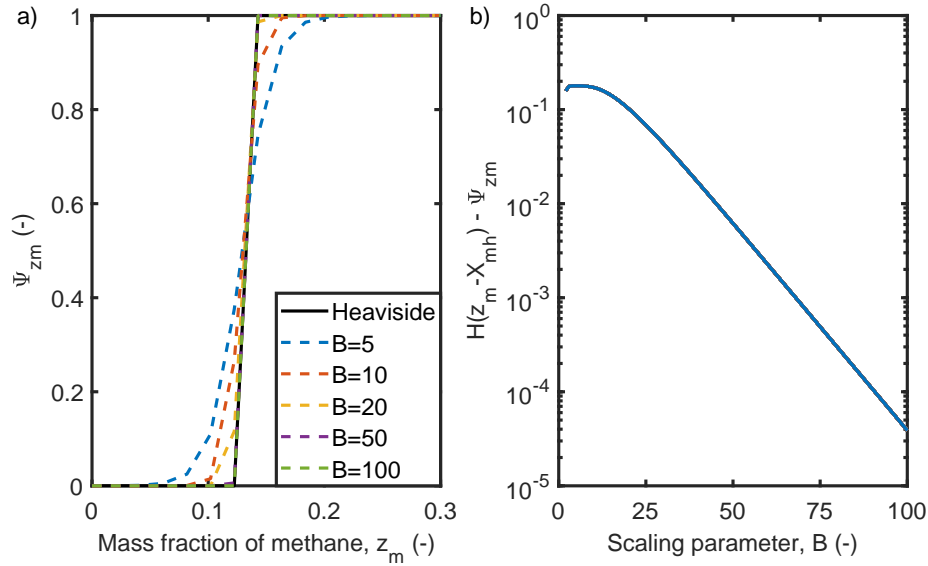
Fig. 5.3: How changing the B parameter affects the smoothed approximation Ψ_{zm} in Eq. (5.20) compared to the analytical Heaviside function in Eq. (5.18). (a) How increasing B tends the approximation to the analytical. (b) The associated error between the smoothed approximation and the Heaviside function.

calculated numerically as follows

$$\bar{\delta} = \frac{1}{M} \sum_{n=1}^{M} |\delta(n)| \tag{5.42}$$

where M is the number of time steps output and $\delta(n)$ is given as

$$\delta(n) = \frac{m_i(0) - m_i(n) + m_{iP}(n)}{m_i(0)} \times 100 \tag{5.43}$$

where $m_i(n)$ [M] is the mass in place at time n of component i and $m_{iP}(n)$ [M] is the mass produced at time t of component i. The terms m_i and m_{iP} are found numerically as follows

$$m_i(n) = \int_0^V G_i(t)dV \tag{5.44}$$

and for a 1D model:

$$m_{iP}(n) = \int_0^t \nabla \cdot \mathbf{F}_i|_{x=0}dt \tag{5.45}$$

5.4.3.3 Scaling parameter A

All model outputs displayed in the following sections use the parameterisation given in Chapter 4 unless specified otherwise. The only difference is that conditions must be initialised in equilibrium. Therefore, the following initial saturations are used: $S_{hI} = 0.1$,
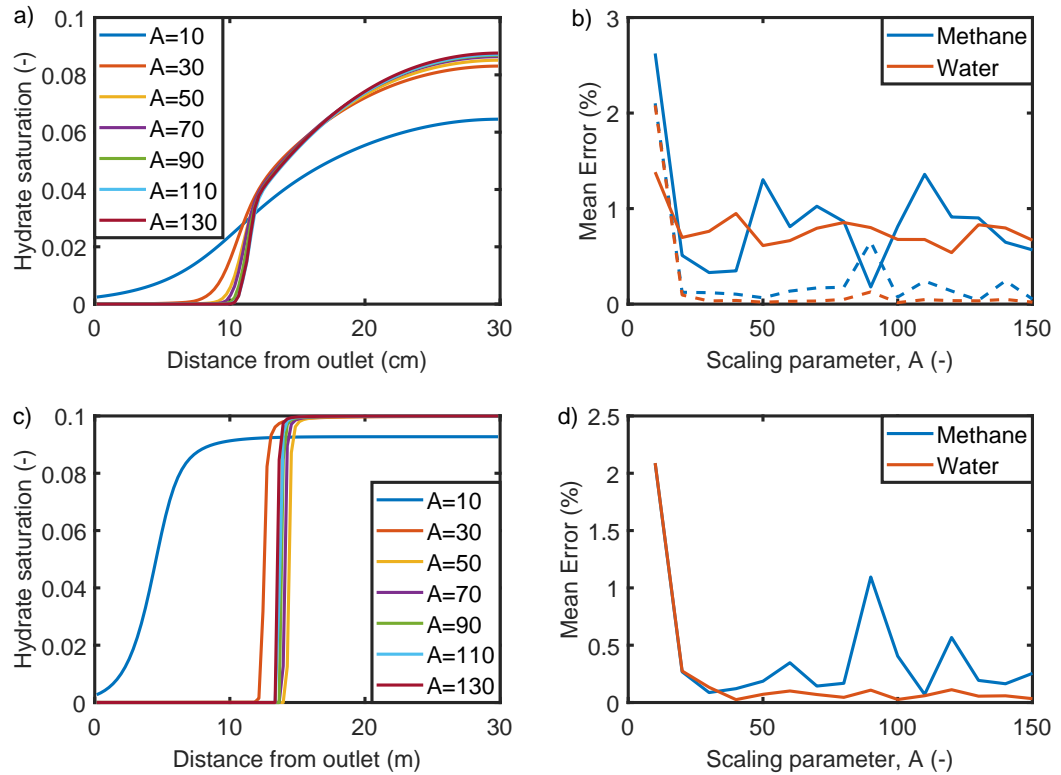
Fig. 5.4: How changing *A* affects the dissociation front and error. (a) The response of hydrate saturation with increasing *A* using 100 nodal points. (b) The mean absolute normalised component error for methane and water complimentary to (a). Solid lines used 100 nodal points to discretise the domain. Dashed lines used 200 nodal points to discretise the domain. (c) The response of hydrate saturation with increasing *A* for a domain 30 m long using 100 nodal points. (d) The mean absolute normalised component error for methane and water complimentary to (b).

$S_{aI} = 0.9$ and $S_{gI} = 0$.

The numerical model is significantly more sensitive to the scaling parameter, *A*. Fig 5.4 shows how increasing *A* affects the dissociation front and changes the error. Two cases are presented in Fig. 5.4. Figs. 5.4a and b show outputs from the core scale model in Chapter 4, whereas Figs. 5.4c and d show outputs from the same mathematical model as in Chapter 4 but for a domain 100 times larger. This is done to demonstrate how the model performs at different scales. In both cases shown in Fig. 5.4a and c, when the value of *A* is low, the dissociaton front is shallow and does not allow the hydrate to completely dissociate. This corresponds with significant error as exhibited in Fig. 5.4b and d. Increasing *A* causes the front to sharpen out but beyond $A = 90$ for both cases, increases in *A* does not greatly change the front location or form. An interesting observation to draw from Fig. 5.4a is that the dissociation front is curved. This suggests that there is an inherent rate dependency in the equilibrium model that is observed at this core scale (30 cm). However, note that in Fig. 5.4c, this curved feature disappears as the

size of the domain is increased, leading the front to behave more step-wise. Furthermore, by comparison of Figs. 5.4b and d, the error is reduced for the larger domain, despite a coarser resolution. This suggests that much of the component error in Fig. 5.4b is likely through this curved feature which is at odds with the step-wise assumption in Eq. (5.17). However, from Fig. 5.4b, increasing the grid resolution can significantly reduce this error, indicating that the error associated with this curved front is also limited by the resolution across it. Not displayed in Fig. 5.4a, using 200 nodal points instead of 100 for a given A does not significantly change the front location or form. From Fig. 5.4b and d, after the initial drop-off for low A values, there appears to be no pattern between the value used for A and the error development.

However, by interpreting the error and with the aim to make the front as sharp as possible, for a core scale model using 100 nodal points, an $A = 40$ is appropriate. For the core scale model using 200 nodal points, A has a greater range and can be up to 80. Similarly, for the larger scale model using 100 nodal points in Fig. 5.4d, an A of 80 can be chosen.

From this analysis, it is suggested that the equilibrium model derived in this chapter is better suited to larger scale problems where the dissociation front would behave more like the step-wise formulation in Eq. (5.17). Improving the resolution of the problem can enhance the range of A that can be utilised. Nonetheless, it is advised that before running simulations, the A parameter is tested by assessing the error and factoring it in against the resolution required.

5.4.4   Further discussion

The equilibrium model developed in this chapter must first be validated before there is confidence in its ability to simulate regional scale problems. Following Gamwo & Liu (2010) and Liu & Gamwo (2012), the kinetic model can be used to verify the equilibrium model by increasing the intrinsic dissociation constant, k_{d0} to unrealistic values. Doing so acts to sharpen out the dissociation front providing an analogous model response to increasing the spatial scale.

Fig. 5.5 compares the equilibrium model to the kinetic model in this way for four outputs of pressure, hydrate saturation, temperature and bulk mass per unit volume through the rock core, observed at a single time. From all four comparisons, as the dissociation rate increases, the kinetic model converges towards the equilibrium model. That all

outputs converge suggests that all aspects of the system tend to the equilibrium case. Attention can be drawn to some features. In Fig.5.5a, the pressure wave in the kinetic model appears to converge quicker to the equilibrium response than the dissociation represented in Fig. 5.5b. This may be due to the delay in mass release at the dissociation front as the pressure falls below the equilibrium pressure in the rate-dependent kinetic model compared to the relatively instantaneous formulation of the equilibrium model. In Fig. 5.5c, as the dissociation rate increases and the front narrows, the temperature profile concaves and a greater drop in temperature is observed. This is likely due to the latent heat loss on dissociation becoming more concentrated.

Furthermore, increasingly large increments of k_{d0} sharpen the front out less as the kinetic model tends towards the equilibrium model. This suggests that there is a non-linear relationship between the intrinsic dissociation constant and scale. These subsidiary observations demonstrate the numerical limitations associated with handling the hydrate dissociation kinetics at larger scales. However, it is not the focus of this study to investigate this relationship further.

As discussed in Section 5.3 and inferred in Fig. 5.1, for each kinetic model run with an increased k_{d0} in Fig. 5.5, the number of nodal points required to discretise the dissociation zone must increase. Subsequently, this leads to significant increases in computation time. For example, the simulation labelled 400 k_{d0} in Fig. 5.5 had a run time of more than 6 hours and used 600 nodal points. By contrast, using the same computer, the equilibrium model (with $A = 80$) took around 20 minutes with 200 nodal points used to discretise the domain. Significant savings in computation time can be made by using the equilibrium model.

From the work in this chapter, it can be concluded that, by assuming k_{d0} is an appropriate proxy for scale, the equilibrium model developed in this chapter is viable to model reservoir scale problems initialised under equilibrium conditions.
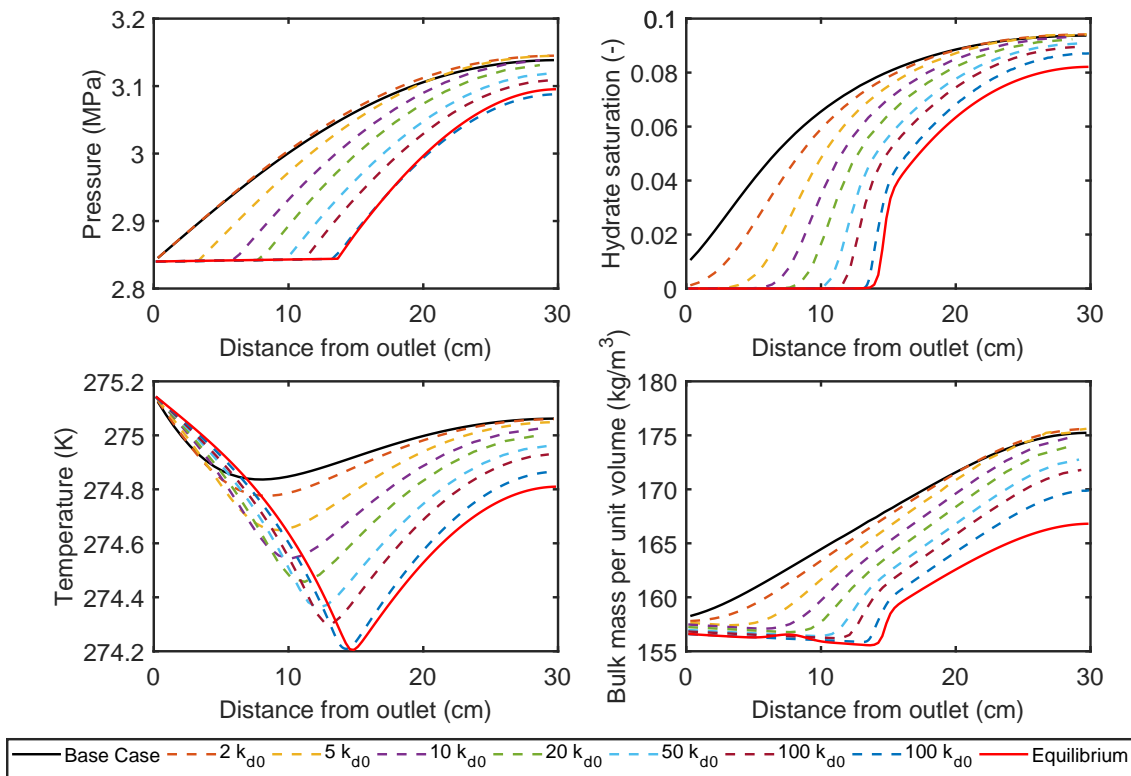
Fig. 5.5: Convergence of the kinetic model towards the equilibrium model by increasing the intrinsic dissociation constan, k_{d0}. Recall that the base case $k_{d0} = 36$ kmol m^{-2} Pa^{-1} s^{-1} Figures include: (a) Pressure, P. (b) Hydrate saturation, S_h. (c) Temperature, T and (d) Bulk mass per unit volume, F.

6. CONCLUSIONS AND FURTHER WORK

Methane hydrates have gained significant attention in recent years as a cleaner, potential energy resource and due to fears that ocean warming driven by climate change may lead to widespread methane release at the sea floor.

Multi-component, multi-phase (MCMP) modelling is a powerful tool which can be used to investigate methane hydrate dissociation by numerically solving a set of mass and energy conservation equations. However, throughout literature there is a lack of clarity over how best to describe controlling dynamics in the presence of hydrate such as heat transfer, hydrate stability and relative permeability.

The objective of this project was to develop a new numerical model capable of simulating methane hydrate dissociation in a laboratory and regional scale setting. By building the model from first principles, the controlling dynamics were freely assessed at the laboratory scale against real experimental data. Furthermore, existing studies typically use numerical integration schemes which are only 1st order accurate. Instead, this study takes advantage of the built-in high accuracy, multi-step, multi-order, ordinary differential equation (ODE) solvers found within MATLAB. This study sought to apply the Method of Lines (MOL) approach to convert the partial differential equations (PDEs), used to describe mass and energy conservation, into a set of ODEs to be integrated by the MATLAB solvers. This is done by replacing the spatial derivatives in the governing equations with algebraic approximations while keeping the temporal derivative continuous.

In Chapter 2, mass, momentum and energy conservation statements were presented for the methane hydrate dissociation problem. The energy conservation statement was demonstrated to be directly derivable from the first law of thermodynamics and the Clapeyron equation was shown as a viable way of handling the latent heat loss that occurs as hydrate dissociates. Literature review revealed a wide variation in methods for quantitatively handling many of the relevant characteristics, including the surface area to volume ratio of hydrate available to dissociation (Section 2.6.2), hydrate formation/dissociation

pressure (equilibrium pressure) (Section 2.6.3), the effect of salinity on hydrate stability (Section 2.6.3.1) and handling of relative permeability (Section 2.5.1).

In Chapter 3, the numerical solution scheme and methodology was described. Time integration methods were compared with focus on numerical stiffness, and the theory behind MATLAB's ODE solvers were outlined. Common methods solving the hydrate dissociation problem use 1st order integration methods together with the so-called "primary variable switch method" (PVSM) which switch the primary dependent variables (PDVs) to be solved for depending upon the availability of the phases (Gamwo & Liu, 2010; Liu & Gamwo, 2012; Moridis, 2012). However, PDVs are not able to be switched during MATLAB's ODE solver routine. Therefore, to use MATLAB's solvers in conjunction with the MOL, it was necessary to recast the mass and energy conservation equations into a set of persistent PDVs that can define the whole system state at any point in space and time domain. The algebraic approximations to the spatial derivatives in the MOL approach were achieved using finite differencing in conjunction with a 1st order Godunov upwinding scheme to resolve discontinuities that arise due to increases in gas and water flow as hydrate dissociates.

Through numerical modelling, Chapter 4 investigated an experimental dataset provided by Masuda et al. (1999) to derive the mathematical model in Chapter 2 and verify the numerical solution scheme in Chapter 3. This experimental dataset had been widely simulated before (Nazridoust & Ahmadi, 2007; Liang et al., 2010; Zhao et al., 2012a; Ruan et al., 2012a; Shin, 2014; Chen et al., 2016) or used as a base case for numerical parameter sensitivity analysis (Gamwo & Liu, 2010; Ruan et al., 2012b; Zhao et al., 2014, 2015, 2016; Song et al., 2016). The Masuda experiment involved pressure induced hydrate dissociation within a Berea sandstone core saturated with hydrate, gas and water. The dataset included information about the rate of gas production, the total production of water, the temperature evolution through time at three discrete locations in the core and pressure evolution at the opposing end to the fluid outlet. Whereas many previous studies calibrated to the rate of gas production and the temperature distribution, observed data concerning the far-field pressure evolution or the water production has generally been ignored. It was first realised through a mathematical material balance that the initial phase saturations reported by Masuda et al. (1999) were likely to be incorrect. Using an updated set of phase saturations, it was discovered that in order to simulate the experimental response which included reconciling a fast gas production with a relatively slow pressure decline, hydrate was assumed to significantly impede fluid flow, even at very small hy-

drate saturations. A new relative permeability model, the so-called "Critical Threshold model", described in Section 2.5.1, was therefore developed and calibrated against the experimental data. Furthermore, it was shown that the Masuda experiment can also be adequately simulated using a 1D model.

At larger scales, the dissociation front becomes sharper causing the stability of the kinetic model used in Chapter 4 to become limited by the Peclét number. While a 1st order Godunov scheme can be used to resolve across sharp fronts for flowing material, hydrate does not flow such that an upwinding scheme cannot be applied to the mass conservation equation for hydrate. The kinetic model can only be utilised at larger scales when excessively high spatial resolutions are maintained, which in turn leads to impractical computation times. Furthermore, the formulation used to describe hydrate kinetics cannot also handle the formation of hydrate which becomes an important consideration over larger time scales. An alternative "equilibrium model" in Chapter 5 was developed which removes the hydrate kinetics by assuming hydrate dissociation and formation is an instantaneous transfer of components between phases based upon the local hydrate stability conditions. In this instance, the PVSM may be a more suitable approach as it avoids the need to resolve the front explicitly by instead simulating either side of the dissociation front. Although the PVSM cannot be applied when using MATLAB's ODE solvers, it was shown in Chapter 5 that a set of persistent PDVs for the equilibrium problem can be utilised for an equilibrium model by approximating the instantaneous transfer of components between phases with a smoothed step-function. This MOL equilibrium model was benchmarked against the existing kinetic model in Chapter 4 by initialising the kinetic model under equilibrium conditions at laboratory scale. The rate of hydrate decomposition was increased to produce a sharper dissociation front analogous to how the domain would look at the reservoir scale. The two models matched each other well, providing confidence in the formulation of the equilibrium model. Under these conditions, the equilibrium model was found to be significantly less computationally expensive.

Preliminary work in Section 6.1 applies this equilibrium model to simulate reservoir scale hydrate dissociation driven by ocean warming and assess methane release rates. A 1D vertical model of a hydrate saturated reservoir beneath a water column of variable thickness was invoked. All existing MCMP models developed for the purpose of assessing hydrate dissociation driven by ocean warming specifically use the modified Stone three-phase relative permeability model originally developed for gas-water-oil flows (see Section 2.5.1), often with the same parameters (Reagan & Moridis, 2008, 2009; Reagan

et al., 2011; Thatcher et al., 2013; Marín-Moreno et al., 2013, 2015a,b; Stranne et al., 2016a,b). There is no explanation in the literature as to why this formulation or parameterisation is an appropriate choice. Instead, this study used the Critical Threshold relative permeability model outlined in Section 2.5.1 alongside the parameterisations found to adequately simulate the data from the Masuda experiments in Chapter 4.

A major concern is that large quantities of methane might migrate into the oceans and atmosphere when shallow marine hydrate dissociates in response to a warming climate. For hydrate-derived methane to enter the ocean or atmosphere in sizeable quantities, the methane released from the hydrate-bearing sediment must flux at a large enough rate to bypass the methane sink in the shallow sea floor sediment, the so-called "sulphate reduction zone" (SRZ). Therefore two main controls should be aimed to be constrained when it comes to assessing the size of the flux from the sediment at a particular locale through MCMP modelling: (1) the strength and size of the local SRZ sink, as this will limit the amount of methane entering the ocean (Boetius & Wenzhöfer, 2013). (2) how phases can mobilise through the porous media in the presence of hydrate.

A number of two-phase (Masuda et al., 1999; Delli & Grozic, 2013; Daigle, 2016) and three-phase (Moridis, 2012) hydrate-associated relative permeability models can be found. However, in this study, an alternative relative permeability model, the Critical Threshold model (Section 2.5.1) was necessarily formulated in order to simulate the experimental data set from Masuda et al. (1999). From the discussion in Section 2.5.1, it can be considered that the appropriate relative permeability model to choose from is strongly related to the methane hydrate morphology as it grows within the porous network. The hydrate morphology itself is dependent upon the distribution of hydrate forming phases. In a heterogeneous porous medium, such distribution is non-uniform as it is related to the interfacial tension and wetting relationships between these phases and the porous network. It therefore could suggest that, although ignored in this thesis, capillary pressure may also be an important consideration when assessing methane release rates in regional scale shallow marine environments, susceptible to climate change.

Both relative permeability and capillary pressure are strong functions on the hydrate morphology which is intrinsically correlated to the pore morphology. Correctly assessing the correlation between hydrate growth in porous media and porosity will help understand flow in hydrate saturated porous media.

From this project, it is concluded that continued effort should be made to constrain flow in hydrate-bearing sediments through relative permeability experiments. In partic-

ular, focus should be driven towards simultaneous flushing of hydrate saturated porous media with gas and water. Doing so would help produce a dataset from which mathematical three-phase relative permeability models can be developed in order to better constrain the appropriate handling of relative permeability in regional scale models.

Where possible, modellers should refrain from employing only one relative permeability model and parameterisation to their MCMP models as this may dramatically mislead the volume of methane that may be derived from hydrate as a response to climate change. Instead, an ensemble of models should be utilised to better understand the uncertainty associated with relative permeability and how it controls whether methane will, and at what rate, discharge into the oceans as a response to climate change.

6.1 Preliminary regional scale simulation of climate induced hydrate dissociation

6.1.1   Objective

- Utilise the equilibrium model developed in Chapter 5 for a regional scale problem.

- Compare the response of the hydrate inventory with climate change to previous studies.

- Assess the effect of utilising a different three-phase relative permeability models on methane release rates.

6.1.2   Highlights

- The equilibrium model can adequately simulate regional scale climate driven hydrate dissociation problems.

- The choice of three-phase relative permeability model significantly affects the timing of methane release due to the onset of sea floor warming.

- Hydrate derived methane flux rates in sediment are strongly controlled by relative permeability.

6.1.3   Introduction

A number of articles have used multi-component, multi-phase (MCMP) flow modelling to quantify methane release into the oceans and atmosphere driven by hydrate dissociation in a regional scale setting (Xu et al., 2001; Reagan & Moridis, 2008, 2009; Reagan et al., 2011; Thatcher et al., 2013; Marín-Moreno et al., 2013, 2015a,b; Stranne et al., 2016a,b). In each case, hydrate dissociation driven by climate change is interpreted as a change in ocean temperature. Although sea levels are rising due to warming of polar ice caps, sea level change is consistently ignored when considering geologically short time periods. Even in extreme cases of sea level change (e.g. 20 mm yr^{-1}), warming induced by climate change drives regional scale dissociation significantly more over a century scale (Hunter et al., 2013).

Reagan & Moridis (2008) performed 1D modelling of such a problem by linearly increasing the sea floor temperature over 100 years for three hydrate-bearing environments. One case represented cold, deep ocean hydrate deposits, another represented shallow, warmer hydrate deposits analogous to the Gulf of Mexico and a third case represented shallow, cold conditions associated with arctic shelf hydrate deposits. They found that the deepest deposits were unaffected by temperature change at the sea floor whereas the shallower deposits were highly susceptible. Furthermore, they also found that permeability strongly controlled hydrate dissociation and methane release rates.

Building on this, Reagan & Moridis (2009) and Reagan et al. (2011) applied a 2D model to investigate the possible origin of recent gas plumes observed at the seabed offshore West Svalbard region. They concluded that the plumes were most likely due to the dissociation of low saturation hydrates at shallow depths beneath the sea floor.

Thatcher et al. (2013) also investigated the West Svalbard area. They hypothesised that emissions observed in 2008 (Westbrook et al., 2009) may have been driven by an anomalous sea temperature increase 30 years before. A sensitivity analysis was performed on a one-dimensional numerical simulation to look at: (1) the delay time between the onset of ocean warming and the emission of gas from the sea floor; (2) the rate of gas emissions from the sea floor. Three parameters studied included: (1) the saturation of the hydrate in the sediment; (2) permeability of the host sediments; (3) a methane flux rate at the base of the model. The models were configured to run for 100 years and dissociation was driven by the sea floor temperature which linearly increased from $2^{o}C$ to $3^{o}C$ over a period of 33 years and was then held constant at $3^{o}C$ thereafter. Thatcher et al. (2013)

showed that in order to achieve a time delay of around 30 years from the onset of ocean warming, a combination of a higher hydrate saturation, a larger permeability, a lower porosity and a shallower depth to the top of the hydrate was required. This was compared to a base case model using parameters provided by assessments of the broader regional geology. The depth to the top of the hydrate was maintained by elevating the gas flow at the base of the gas hydrate stability zone (BGHSZ) to the order of tens of mol m^{-2} yr^{-1}. However, Reagan et al. (2011) states that this gas flow beneath the BGHSZ is not known in this region. Artificially forcing the hydrate close to the sea floor in this way would naturally coincide with reduced delay times between the onset of warming and methane release. From their study, Thatcher et al. (2013) suggested that fractures may form during hydrate dissociation in low permeability reservoirs as the local gas pressure increases above the lithostatic pressure which could enable rapid release of methane and reduce the delay time significantly.

Marín-Moreno et al. (2013) built on the work by Thatcher et al. (2013) in the West Svalbard area by constructing seabed temperature time series data applied beneath a discrete set of water depths ranging from 350 to 800 m for the previous 2 millennia and across the next three centuries. The water depth to the sea floor is an important consideration in these investigations as it determines the thickness of the gas hydrate stability zone (GHSZ) within the sediment. The GHSZ is limited by the temperature and pressure distribution through the hydrate-bearing reservoir where pressure increases with depth below the sea floor and the pressure acting on the sea floor is due to the weight of the water column. To investigate future methane release rates and how the thickness of the GHSZ may respond, they used two climate models, CCSM-4 and HadGEM2 (Gent et al., 2011; Collins et al., 2011), under two climate warming scenarios, RCP 2.6 and RCP 8.5 (Representative Concentration Pathway) (Moss et al., 2010). RCP 2.6 predicts a modest warming scenario whereas RCP 8.5 predicts an extreme warming scenario. Their 1D model used many similar parameters to the base case of Thatcher et al. (2013). As in Reagan & Moridis (2008), the deeper hydrate deposits were found to be unaffected by changes in ocean temperatures. However, their models showed that over 300 years, hydrate deposits below water depths of less than 600 m became more sensitive to ocean warming, with deposits situated beneath water depths of 400 m completely dissociating for both climate models.

Some studies assessing methane release due to climate driven hydrate dissociation over a centuries scale ignore MCMP dynamics such as permeability, relative permeabil-

ity and endothermic heat loss on dissociation (Biastoch et al., 2011; Giustiniani et al., 2013; Kretschmer et al., 2015). Such models handle hydrate-derived methane release as related to the vertical shift in the BGHSZ and subsequent volume loss of the GHSZ. These approaches use knowledge of the conductive heat flow, sediment porosity and hydrate saturation and assume the hydrate is in constant equilibrium under steady state conditions.

Stranne et al. (2016a,b) and Ruppel and Kessler (2017) reiterated the importance of incorporating MCMP dynamics into estimations of methane release derived by climate driven hydrate dissociation. Stranne et al. (2016b) performed a direct comparison over century scales of models including MCMP dynamics compared to the volume balance approach which do not. It was found that ignoring methane sinks in the sediment like permeability can lead to overestimations of the amount of methane produced by several hundred percent.

Each of the studies performing MCMP modelling to determine methane release by hydrate dissociation as a response to climate change use the popular TOUGH+HYDRATE code (Moridis, 2012). T+H gives the user a broad selection of functions to handle the properties of the sediment. This said, each of the above studies use the so-called "modified version of Stone's first three-phase relative permeability model" outlined in Eq. (2.22) and herein referred to as the "Modified Stone" model. Each study set relative peremabiliy parameters $n_g = n_a = 4$ and $S_{gc} = 0.02$. All studies use $S_{ar} = 0.12$ except for Reagan & Moridis (2008) and Reagan et al. (2011) who used $S_{ar} = 0.2$. There is no explanation in the literature as to why these parameter values and formulation are an appropriate choice.

The objective of the following is to assess whether utilising a different relative permeability model affects the nature and rate of methane release at the sea floor, driven by ocean warming. The Critical Threshold model in Section 2.5.1 and parameterisation derived in Chapter 4 is applied in conjunction with the equilibrium model developed in Chapter 5 in a regional setting. This work will perform simulations using initial and boundary conditions from the West Svalbard area because of the recent widespread methane emissions that are being observed there (Westbrook et al., 2009) and due to the availability of previous studies which can be used for comparisons (Reagan et al., 2011; Thatcher et al., 2013; Marín-Moreno et al., 2013). In particular, the study by Marín-Moreno et al. (2013) is closely followed and is compared due to the particular clarity of input data provided by the author.

6.1.4   Data and methods

6.1.4.1   Mathematical model

Following Marín-Moreno et al. (2013), MCMP models are used to assess the hydrate inventory response and methane emission rates due to warming in the West Svalbard area. The simulated hydrate reservoir is assumed to reside beneath shallow water depths of 400 and 450 m as these are the most likely to dissociate under ocean warming. Fluid can only escape at the top of the reservoir into the overlying water column. The ocean is not simulated and is instead represented as a fixed pressure boundary and the projected transient sea floor temperatures as a fixed temperature boundary, as in Marín-Moreno et al. (2013). Sea floor temperature-time series data was constructed by Marín-Moreno et al. (2013) under these water depths from 1 AD to 2300 but here limited to 2150 due to the compounding uncertainty in climate model forecasts through time. Sea floor temperature for the period 1 AD to 2005 is extracted from foraminifera proxy data and ocean water measurements whereas from 2006 to 2150, the climate model CCSM-4 and two warming scenarios, RCP 2.6 and 8.5, are used (further information regarding how this data is acquired can be found in the supporting information by Marín-Moreno et al. (2013)). The temperature data is shown in Fig. 6.1.
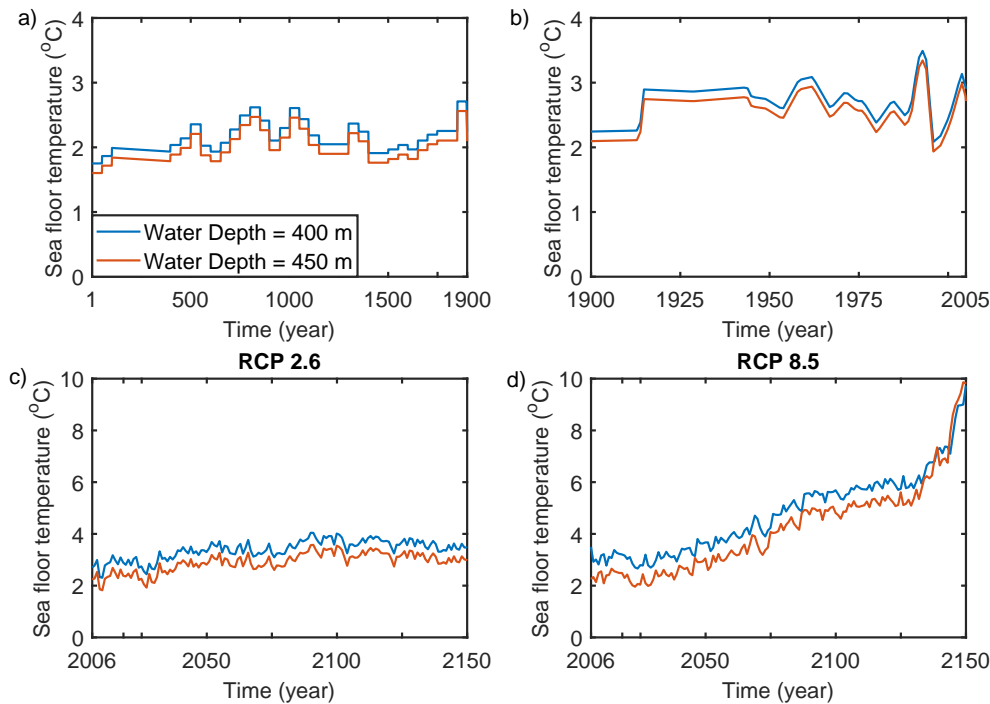
Fig. 6.1: Temperature time-series data for the period 1-2150 years. (a) and (b) show temperature data from 1 AD to 1900. (c) RCP 2.6. (d) RCP 8.5. Data provided by Marín-Moreno et al. (2013).

Let Z [L] (= 700 m) be the thickness of the simulated region and z [L] be the elevation above an impermeable bedrock. The rock is vertically oriented such that gravity is included. The domain extends deep enough for the simulated water depths that the impermeable bedrock is sufficiently below the BGHSZ so as not to significantly affect the simulation. From seismic interpretations by Sarkar et al. (2012), the bottom simulating reflector (BSR) could not generally be observed for hydrate reservoirs below water depths of less than 700 m, where the BSR delineates the contact between the BGHSZ and an underlying free gas layer. Given this and the uncertainty of choosing an appropriate rate of gas flow beneath the GHSZ, following Reagan et al. (2011), a gas layer beneath the BGHSZ under the water depths considered is assumed not to exist. In this way, methane release rates can be solely attributed to climate driven hydrate dissociation. A constant heat flow is assumed at the base of the domain.

The "sulphate reduction zone" (SRZ) exists in the shallowest metres below the sea floor (mbsf) and acts to inhibit the amount of methane that can reach the ocean by consuming methane. Marín-Moreno et al. (2013) handled the SRZ by assuming the top 7 m of the reservoir are not saturated with hydrate, despite located within the GHSZ. Alternatively, Reagan et al. (2011) and Thatcher et al. (2013) do not simulate the SRZ. Due to the lack of information regarding the SRZ thickness or methane consumption rate in the West Svalbard area, this study assumes the SRZ is negligibly thick and instead treated as a percentage loss of methane flux between two extremes taken from Boetius & Wenzhöfer (2013): SRZ = 20 & and 80 %.

The numerical modelling approach uses the scheme presented in Chapter 3 and follows the formulation outlined for the equilibrium model in Chapter 5.

As in Eq. (2.15), the following mass conservation statements can be made:

$$\frac{\partial G_m}{\partial t} = -\nabla \cdot \mathbf{F}_m \tag{6.1}$$

$$\frac{\partial G_w}{\partial t} = -\nabla \cdot \mathbf{F}_w \tag{6.2}$$

where, from Eq (2.14):

$$\mathbf{F}_m = -\rho_g \lambda_g (\nabla P + \rho_g \mathbf{g}) \tag{6.3}$$

and

$$\mathbf{F}_w = -\rho_a \lambda_a (\nabla P + \rho_a \mathbf{g}) \tag{6.4}$$

Recall that there is no explicit statement of $\frac{\partial G_h}{\partial t}$ as hydrate is solely treated as a phase in the equilibrium model.

The accompanying heat transport equation is as derived in Eq. (2.45):

$$\frac{\partial U}{\partial t} = -\nabla \cdot (\boldsymbol{v} H) + \nabla \cdot (\kappa_E \nabla \cdot T) \tag{6.5}$$

6.1.4.2   *Initial and boundary conditions*

The model is initialised under equilibrium conditions with pressure, $P = P_I$, and temperature, $T = T_I$, where subscript I is herein used to denote "initial". Consider Eq. (2.19) under hydrostatic conditions which, on rearranging for the pressure gradient leaves

$$\frac{\partial P_I}{\partial z} = -\rho_j g \tag{6.6}$$

From Fourier's law, the initial temperature gradient can be calculated as follows

$$\frac{\partial T_I}{\partial z} = -\frac{Q_H}{\kappa_{EI}} \tag{6.7}$$

where Q_H [MT^{-3}] is a constant heat flow and κ_{EI} [$MLT^{-3}\Theta^{-1}$] is the initial effective thermal conductivity given by

$$\kappa_{EI} = \phi(S_{gI}\kappa_g + S_{aI}\kappa_a + S_{hI}\kappa_h) + (1-\phi)\kappa_R \tag{6.8}$$

Although the average geothermal gradient for the area is around 65 ^oC km^{-1}, following Thatcher et al. (2013), the temperature gradient is initialised using constant heat flow rather than a constant geothermal gradient. This is because the thermal conductivities of hydrate, water and methane gas are highly contrasting such that phase change through the reservoir alters the thermal gradient. Q_H is taken to be 7.7×10^{-2} W m^{-2} (Marín-Moreno et al., 2013).

The derivatives in Eq. (6.6) and (6.7) are solved to obtain steady state solutions for P_I and T_I, respectively, by forward modelling through elevation, z, using MATLAB's explicit solver, ode45 (solving with respect to z rather than t in this case). The following constraints are applied to solve this initial value problem:

$$P_I|_{z=Z} = P_{WD}, \qquad T_I|_{z=Z} = T_{sf}(t=0) \tag{6.9}$$

where P_{WD} [ML^{-1}T^{-2}] is the pressure at the sea floor due to the weight of the water column and T_{sf} is the temperature at the sea floor taken from Fig. 6.1. P_{WD} is calculated as follows

$$P_{WD} = \rho_{sw} g z_{WD} \qquad (6.10)$$

where ρ_{sw} [ML^{-3}] ($= 1035$ kgm^{-3}) is the assumed density of sea water and z_{WD} [L] is the water depth.

The BGHSZ is demarcated as the first depth which the local pressure lies below the equilibrium pressure. Following Reagan et al. (2011), Sarkar et al. (2012), Thatcher et al. (2013) and Marín-Moreno et al. (2013), the empirical expression for the three-phase equilibrium pressure, P_e, in Eq. (2.32) is used with the reference values: $T_{d,ref} = 2^oC$ and $x_{sa,ref} = 0.0134$ (Moridis, 2012) following the work of Wright et al. (1999).

The BGHSZ is linked to temperature through the equilibrium pressure, $P_e(T)$ and therefore Eq. (6.7). In order to approximate the depth to the BGHSZ the thermal conductivity of rock, κ_R, in Eq. (6.8) is calibrated to the observed BSRs under a water depth of 600 m and 700 m observed at ~ 160 m and ~ 175 m respectively (Marín-Moreno et al., 2013; Sarkar et al., 2012). A $\kappa_R = 2.25$ W m^{-1} K was determined to be most suitable at matching the calculated BGHSZ to these observed depths. From Eq. (6.8) this gives an initial effective thermal conductivity below the BGHSZ, κ_{EI}, of 1.43 W m^{-1} K, similar to the thermal conductivity of water saturated sediment used by Marín-Moreno et al. (2013).

The equations of state described in Section 2.8 are used. The following parameters are used for all simulations in this study: $\rho_R = 2600$ kgm^{-3}, $C_{pR} = 2010$ J kg^{-1}K^{-1}, $\phi = 0.5$. The permeability model used is the Critical Threshold model devised in preceding chapters expressed as in Eq. (2.23):

$$k_{ra} = k_{rf} \left(\frac{S_a - S_{ar}}{1 - S_{ar} - S_{gc}} \right)^{n_a}, \qquad S_{ar} \leq S_a \leq 1 - S_{gc} \qquad (6.11)$$

$$k_{rg} = k_{rf} \left(\frac{S_g - S_{gc}}{1 - S_{ar} - S_{gc}} \right)^{n_g}, \qquad S_{gc} \leq S_g \leq 1 - S_{ar}$$

$$kk_{rf} = \begin{cases} k_c, & S_h > S_{hc} \\ k_c + (k - k_c) \left(\frac{S_{hc} - S_h}{S_{hc}} \right), & 0 \leq S_h \leq S_{hc} \end{cases}$$

where, as throughout this project, $k = 96.7 \times 10^{-15}$, $k_c = k/100$ and $S_{hc} = 10^{-4}$. The exponents and residual saturations are taken from Chapter 4 where they were calibrated

to the experimental study by Masuda et al. (1999) and are as follows: $n_g = 2.16$, $n_a = 0.93$, $S_{gc} = 0.0$ and $S_{ar} = 0.1$. Note that the permeability of rock absent of hydrate, k, used in this study is almost equal to the rock permeability suggested by Thatcher et al. (2013) and Marín-Moreno et al. (2013).

Hydrate saturation is one of the least certain parameters in reservoir scale models. In reality, reservoirs are heterogeneous and hydrate saturation may vary significantly through the GHSZ. Clays and fine grained sediment inhibit the accumulation of hydrate, whereas high porosity, high permeability, coarse grained sands tend to host the highest accumulations. This said, high hydrate saturations are not commonly found within the GHSZ (Ruppel and Kessler, 2017) and following Marín-Moreno et al. (2013), a hydrate saturation of 5% is therefore taken. The initial hydrate saturation, S_{hI} [-] is initialised as in Eq. (5.16). A schematic diagram of the above problem is shown in Fig. 6.2 and can also be appropriately constrained by the following initial and boundary conditions:

$$
\begin{aligned}
P &= P_I, & 0 \leq z \leq Z, & \quad t = 0 \\
T &= T_I, & 0 \leq z \leq Z, & \quad t = 0 \\
S_h &= S_{hI}, & 0 \leq z \leq Z, & \quad t = 0 \\
S_a &= 1 - S_{hI}, & 0 \leq z \leq Z, & \quad t = 0 \\
S_g &= 0, & 0 \leq z \leq Z, & \quad t = 0 \\
P &= P_{wd}, & z = Z, & \quad t = 0 \\
T &= T_{sf}, & z = Z, & \quad t \geq 0 \\
\frac{\partial T}{\partial z} &= -\frac{Q_H}{\kappa_E}, & z = 0, & \quad t \geq 0 \\
\mathbf{F}_g &= 0, & z = 0, & \quad t \geq 0 \\
\mathbf{F}_a &= 0, & z = 0, & \quad t \geq 0
\end{aligned}
\tag{6.12}
$$
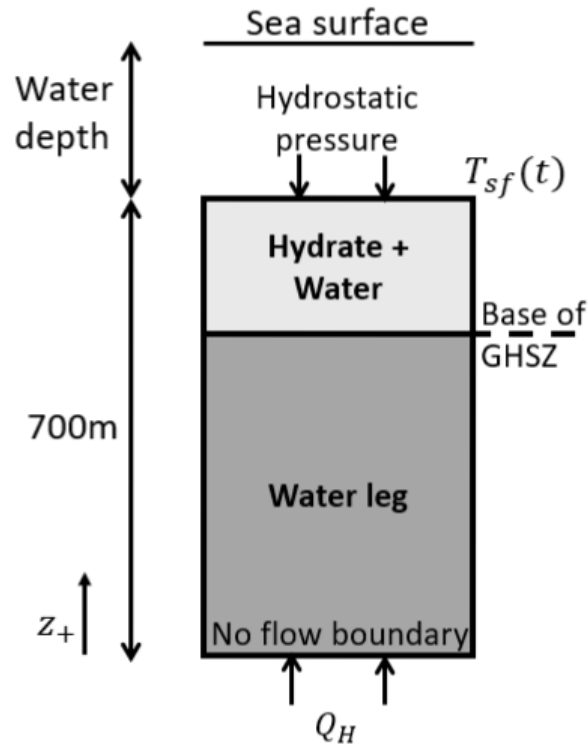
Fig. 6.2: Schematic of the regional scale problem.

6.1.4.3 Recasting in terms of the primary dependent variables

The three PDEs to be solved for include Eqs. (6.1), (6.2) and (6.23). Following the discussion in Section 3.6.3 and the work in Section 5.4.2, it is necessary to recast these equations in terms of fluid pressure, P, temperature, T, and the component mass fraction of methane in the pore-space, z_m. The latter can be found from

$$z_m = \frac{G_m}{F} \qquad (6.13)$$

where

$$F = G_m + G_w \qquad (6.14)$$

The necessary derivatives of z_m and F with respect to time are found from Eq. (3.20) and as in (3.21) respectively to be

$$\frac{\partial z_m}{\partial t} = \frac{1}{F} \left(\frac{\partial G_m}{\partial t} - z_m \frac{\partial F}{\partial t} \right) \qquad (6.15)$$

and

$$\frac{\partial F}{\partial t} = \frac{\partial G_m}{\partial t} + \frac{\partial G_w}{\partial t} \qquad (6.16)$$

Due to the choice of PDVs, $F = f(P, T, z_m)$, it can also be said that

$$\frac{\partial F}{\partial t} = \frac{\partial F}{\partial P}\frac{\partial P}{\partial t} + \frac{\partial F}{\partial T}\frac{\partial T}{\partial t} + \frac{\partial F}{\partial z_m}\frac{\partial z_m}{\partial t} \tag{6.17}$$

From Eq. (5.23), F can be found to be

$$F = \phi\left[\frac{z_m}{\rho_g} + \frac{z_w}{\rho_a} - \Psi_p\left(\frac{X_{mh}}{\rho_g} + \frac{X_{wh}}{\rho_a} - \frac{1}{\rho_h}\right)\left(\frac{z_m(1 - \Psi_{zm})}{X_{mh}} + \frac{z_w\Psi_{zm}}{X_{wh}}\right)\right]^{-1} \tag{6.18}$$

from which it can be shown that the associated partial derivatives of F are obtained as in Eqs. (5.24), (5.25) and (5.26) as follows:

$$\frac{\partial F}{\partial P} = \frac{F}{\phi}\left[\alpha_E + \frac{\phi S_h 2A(1 - \Psi_P)}{P_e}\left(\frac{X_{mh}\rho_h}{\rho_g} + \frac{X_{wh}\rho_h}{\rho_a} - 1\right)\right] \tag{6.19}$$

$$\frac{\partial F}{\partial T} = -\frac{F}{\phi}\left[\beta_E + \frac{\phi S_h 2AP(1 - \Psi_P)}{P_e^2}\frac{dP_e}{dT}\left(\frac{X_{mh}\rho_h}{\rho_g} + \frac{X_{wh}\rho_h}{\rho_a} - 1\right)\right] \tag{6.20}$$

$$\frac{\partial F}{\partial z_m} = -\frac{F^2}{\phi}\left[\frac{1}{\rho_g} - \frac{1}{\rho_a} - \Psi_p\left(\frac{X_{mh}}{\rho_g} + \frac{X_{wh}}{\rho_a} - \frac{1}{\rho_h}\right)\left(\frac{1}{X_{mh}}\left[1 - \Psi_{zm} - z_m\frac{d\Psi_{zm}}{dz_m}\right]\right.\right.$$
$$\left.\left. + \frac{1}{X_{wh}}\left[z_w\frac{d\Psi_{zm}}{dz_m} - \Psi_{zm}\right]\right)\right] \tag{6.21}$$

Recall from Section 2.7, the energy conservation statement in Eq. (2.45), used throughout this thesis, can be recast in terms of P and T by considering all the available phases as follows:

$$\frac{\partial U*}{\partial t} = (\rho C_p)_E\frac{\partial T}{\partial t} - T\beta_E\frac{\partial P}{\partial t} \tag{6.22}$$

$$= -(F_g C_{pg} + F_a C_{pa})\nabla T + (T\beta_g - 1)\nabla \cdot P + (T\beta_a - 1)\nabla \cdot P + \nabla \cdot (\kappa_E \nabla \cdot T) + h_D\frac{\partial G_h}{\partial t}$$

Recall that the equilibrium model does not explicitly state $\frac{\partial G_h}{\partial t}$ such it is necessary to define this term by alternative means. Following the work in Section 5.4.2, it can be shown that $\frac{\partial G_h}{\partial t}$ can be expressed in terms of P, T and z_m to produce a modified expression of the energy conservation statement in Eq. (6.22) as follows:

$$\frac{\partial U^*}{\partial t} = C\frac{\partial T}{\partial t} + D\frac{\partial P}{\partial t} + E \tag{6.23}$$

where

$$C = (\rho C_p)_E - h_D G_{hi}\frac{\partial \Psi_p}{\partial T} \tag{6.24}$$

$$D = -T\beta_E - h_D G_{hi} \frac{\partial \Psi_p}{\partial P} \tag{6.25}$$

$$E = -h_D \Psi_p \frac{\partial G_{hi}}{\partial t} \tag{6.26}$$

where h_D, G_{hi}, $\frac{\partial \Psi_P}{\partial T}$, $\frac{\partial \Psi_P}{\partial P}$ and $\frac{\partial G_{hi}}{\partial t}$ can be found from Eqs. (2.65), (5.30), (5.34), (5.33) and (5.35) respectively. Combining Eqs. (6.17) and (6.23) then yields expressions for $\frac{\partial P}{\partial t}$ and $\frac{\partial T}{\partial t}$:

$$\frac{\partial P}{\partial t} = \frac{\frac{\partial F}{\partial t} - \frac{\partial F}{\partial z_m} \frac{\partial z_m}{\partial t} + \frac{1}{C} \frac{\partial F}{\partial T} \left(E - \frac{\partial U^*}{\partial t} \right)}{\frac{\partial F}{\partial P} - \frac{D}{C} \frac{\partial F}{\partial T}} \tag{6.27}$$

$$\frac{\partial T}{\partial t} = \left(\frac{\partial F}{\partial t} - \frac{\partial F}{\partial z_m} \frac{\partial z_m}{\partial t} - \frac{\partial F}{\partial P} \frac{\partial P}{\partial t} \right) \left(\frac{\partial F}{\partial T} \right)^{-1} \tag{6.28}$$

6.1.4.4 Numerical grid

Given that the detail in the model lies in the top portion of the domain where the hydrate layer is situated and methane is produced at the sea floor, it makes computational sense to refine the grid in this region. Furthermore, as gas rises and water sinks at the dissociating BGHSZ, the underlying water saturated domain should change little through the simulation and can therefore use a coarser discretisation.

It is generally considered good practise to build a grid that transitions smoothly between fine and coarse grid spacings and therefore the grid progresses from the top to the bottom of the reservoir described as follows: The top most grid cell has a fixed thickness of $\Delta z = \Delta z_t$ [L] ($= 0.01$ m) where subscript t in this case denotes the "top" of the reservoir and Δz is the distance between two adjacent nodes. The grid spacing is then geometrically scaled by the coefficient η_t [-] until a depth of 5 mbsf. From hereon to the depth of the BGHSZ, the grid is equally spaced by $\Delta z = \Delta z_h$ [L], where Δz_h is equivalent to the distance between the deepest two nodal points in the top 5 m. From the BGHSZ to the impermeable bedrock, the grid spacing is geometrically coarsened again using a different scaling coefficient, η_w, where subscript w denotes the free water layer below the BGHSZ. The grid spacing in the shallowest 5 m and below the BGHSZ can be described by the following geometric series:

$$\Gamma_L = \sum_{n=0}^{N_L} \Delta z_L \eta_L{}^n = \Delta z_L + \Delta z_L \eta_L + \Delta z_L \eta_L{}^2 + \dots \Delta z_L \eta_L{}^{N_L-1} + \Delta z_L \eta_L{}^{N_L}, \qquad L = t, w \tag{6.29}$$

where N_L [-] is the number of nodal points covering the layer of interest, η_L [-] is a scaling constant for the layer of interest by which Δz_L [L] is scaled through the layer of

thickness Γ_L [L]. Note that for the top 5 m layer, $\Gamma_t = 5$ m and $\Delta z_t = 0.01$ m and that $\Gamma_w = Z - \Gamma_t - \Gamma_h$ where Γ_h is found from Section 6.1.4.2. Note that by virtue of the linear discretisation through the hydrate saturated layer, $\Delta z_w = \Delta z_h$.

From Eq. (6.29), it can be shown that

$$\Gamma_L = \Delta z_L \frac{1 - \eta_L^{N_L+1}}{1 - \eta_L} \tag{6.30}$$

Rearranging in terms of N_L to find the number of points in the water column it leads that

$$N_L = \frac{\ln\left(1 + \frac{(\eta_L - 1)\Gamma_L}{\Delta z_L}\right)}{\ln \eta_L} - 1 \tag{6.31}$$

Recall that the bottom water layer has the least effect on results and therefore $\eta_w = 1.11$ was chosen subjectively to ensure a smooth coarsening up from the base of the hydrate saturated layer to the bottom of the reservoir. Fig. 6.3 shows a graphical example of this grid. The scaling coefficient η_t varies depending on the desired discretisation in the hydrate saturated layer and is shown in Table 6.1.
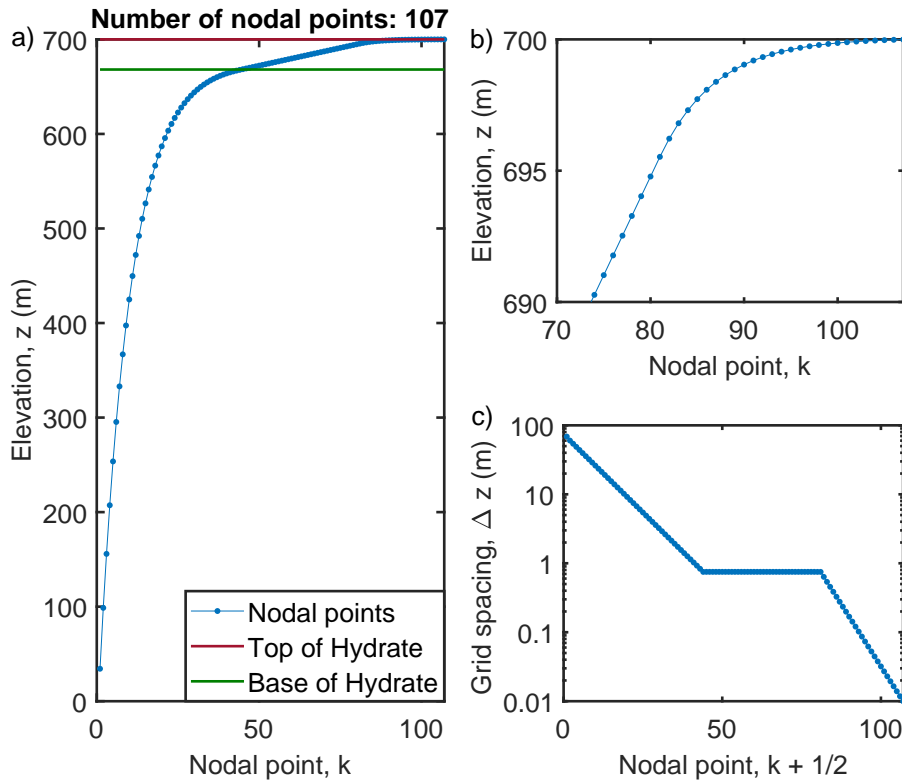

Fig. 6.3: Details of the numerical grid for the case of a hydrate saturated reservoir under a water depth of 400 m. Let k be the spatial index location of a nodal point. (a) The locations of the nodal points through the reservoir. (b) A closer look at the log spaced discretisation in the top 10 m of the domain. (c) How Δz varies through the domain.

6.1.4.5 Model sensitivity testing

Recall that in the equilibrium model formulated in Chapter 5, scaling parameters *A* and *B* control the precision of the smoothing functions which necessarily approximate the Heavisde step-wise function used to describe hydrate dissociation and formation, and transition between gas and water limiting cases respectively. In this section, an optimum value for the scaling parameter *A* is chosen and a convergence test is performed to assess an appropriate resolution for the model runs. The scaling parameter *B* is taken to be equal to 50, following the analysis in Chapter 5.

6.1.4.6 Scaling parameter, A

It was demonstrated in Chapter 5, that increasing *A* acts to sharpen the dissociation front. Following Chapter 5, it is necessary to test the sensitivty of *A* to determine a suitable value. Depicted in Fig. 6.4a, as *A* increases, the smoothing function tends the hydrate saturation towards that given by the analytical Heaviside step-wise function: $S_h H(P - P_e)$.

In Fig 6.4b, the difference between the smooth approximation, Ψ_P, and the Heaviside function decays exponentially with increasing *A*. The test resolution used is shown in Fig. 6.3. Beyond $A = 160$, there is not much improvement in the approximation by choosing a higher value to warrant the increased computation time that was found to be required. Subsequently, a value of $A = 160$ is chosen as a compromise between precision and computation time. Regardless, the approximated depth to the BGHSZ lies within an acceptable range because of the large uncertainty in the distribution of hydrate at the BGHSZ. Ruppel and Kessler (2017) states that the BGHSZ is continually dissociating and reforming hydrate due to seasonal and historical temperature variations suggesting it is unlikely to be of the same saturation as in the GHSZ. Emissions are currently observed in the west Svalbard area suggesting the BGHSZ is already dissociating (Westbrook et al., 2009).

6.1.4.7 Convergence test

Recall from Section 6.1.4.4 that deeper than the first 5 mbsf, a linear discretisation is used throughout the GHSZ. Greater water depths can maintain thicker GHSZs due to the increased weight of the water column. In order to apply the same grid spacing through the hydrate saturated layer, Δz_h, different numbers of nodal points are required for each water depth studied. A convergence test is performed to assess how many nodal points are
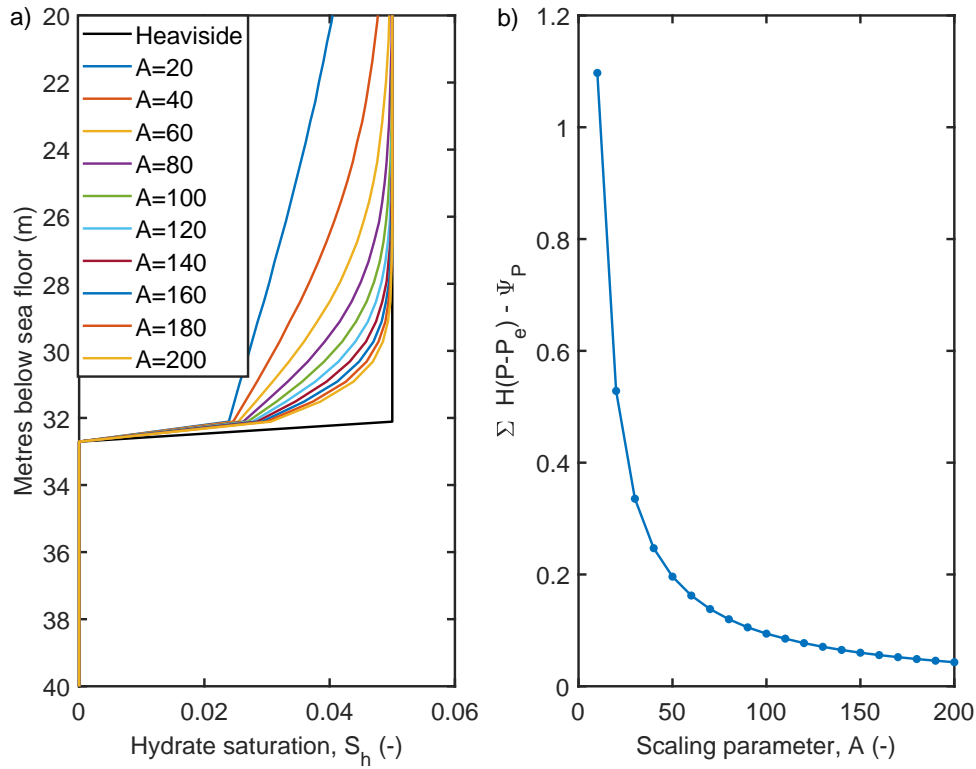
Fig. 6.4: An analysis on the scaling parameter, A. The reservoir is initialised under a water depth of 400 m using RCP 8.5. For this, $B = 50$ and the numerical grid is as described in Fig. 6.3. (a) How increasing A improves the approximation of the BGHSZ. (b) The difference between the smoothed approximation in Eq. (5.19) and the analytical Heaviside step function in Eq. (5.17).

required to adequately resolve a numerical model of this kind within an acceptable error. The shallowest water depth of interest, 400 m, along with RCP 2.6 is used for testing because it would be the most susceptible to warming induced dissociation. The component masses for each run is integrated over a time interval of 1 year in Section 5.4.3.2. Fig. 6.5 shows the results of this convergence test and Table 6.1 shows how the resolution grows the number of nodal points required. From Fig. 6.5, the model using $N_z = 107$, has a mean absolute normalised error for the gas component in the simulation of around 0.3 %. While a resolution of $N_z = 125$ has a lower error, such improvements were not worth the increased computation time, particularly in the case where water depth is 450 m, when the objective of this study is to compare model responses and not to accurately predict the total methane released due to climate change. Furthermore, preliminary testing with much coarser discretisation showed that the error could also be reduced by integrating over a smaller discrete time interval in Section 5.4.3.2, such as 0.1 or 0.01 years. However, given the simulated time is 2150 years, extracting such small time intervals from MATLAB's ode solver leads to impractical computation times for higher spatial resolutions.
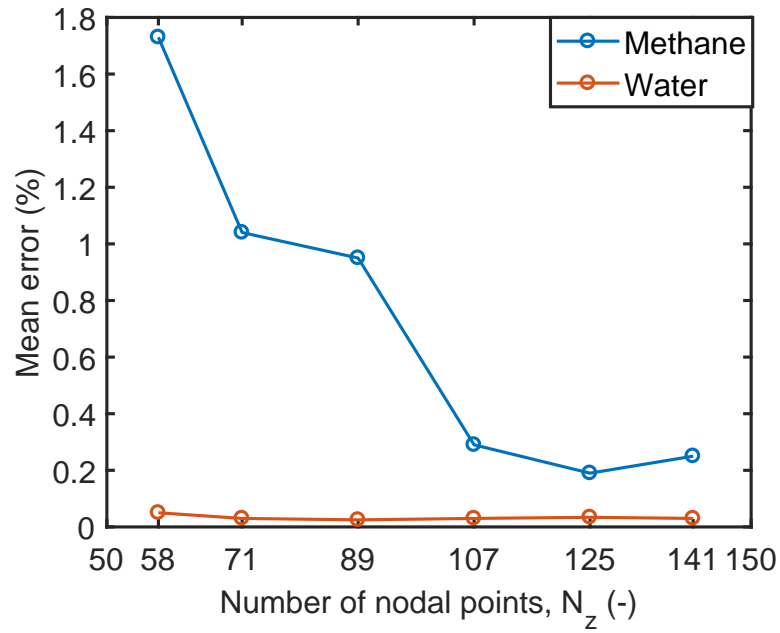
Fig. 6.5: Results from the convergence test for RCP 2.6. Mean absolute normalised error is calculated as in Section 5.4.3.2.

	η_t	1.80	1.40	1.26	1.18	1.14	1.11
	Δz_h (m)	2.0	1.50	1.0	0.75	0.60	0.50
$z_{WD} = 400$ m	N_z	58	71	89	107	125	141
$z_{WD} = 450$ m		75	94	125	155	184	212

Tab. 6.1: The η_t used to adjust the discretisation through the hydrate, Δ_{zh} and the corresponding number of nodal points used for the 400 m and 450 m water depth cases.

6.1.5   Results and discussion
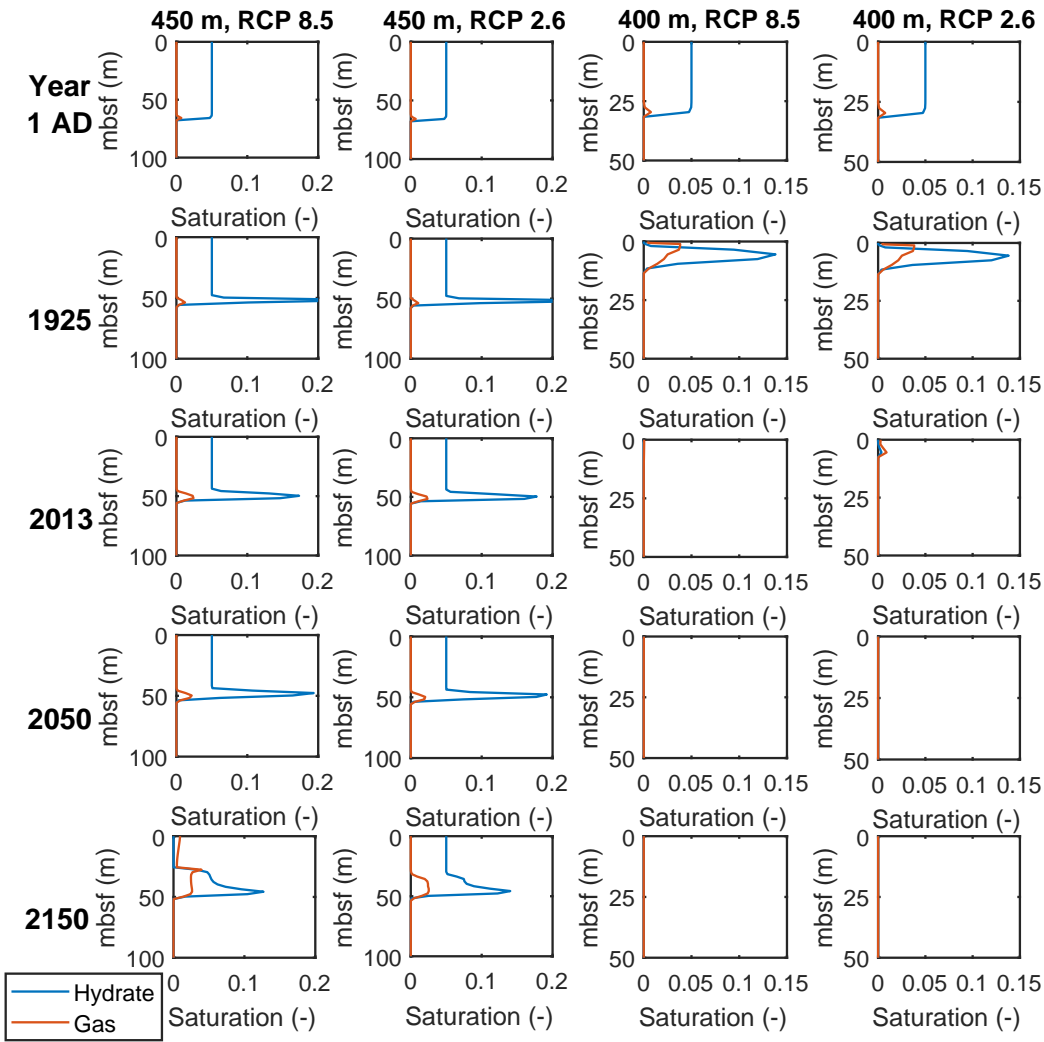
Fig. 6.6: Hydrate and gas saturation profiles through the shallowest depths of the domain at discrete times: 1 AD, 1925, 2013, 2050, 2150. From left to right, the models observed are: $z_{WD} = 450$m and RCP 8.5, $z_{WD} = 450$m and RCP 2.6, $z_{WD} = 400$m and RCP 8.5 and $z_{WD} = 400$m and RCP 2.6.

Following simulations of the above problem, gas and hydrate saturation distributions at the years 1 AD, 1925, 2013, 2050 and 2150 are shown in Fig. 6.6. Saturation profiles at year 1 AD are the initial saturation conditions used and years 2013 and 2050 are used for direct comparison to Marín-Moreno et al. (2013) (see Fig. 4 of their supporting information). Recall that the same temperature time-series at the top of the domain is used for both RCP cases at a given water depth up until 2005, hence the simulation similarities in 1925. Fig. 6.7a shows the methane release over the period 1800-2000 under a water depth of 400 m. Flux rates for the 400 m water depth for RCP 8.5 and RCP 2.6 are shown in Fig. 6.7b and d respectively and the case of a 450 m water depth, RCP 8.5, is shown in Fig. 6.7c. The simulation under a 450 m water depth and RCP 2.6 is not illustrated in
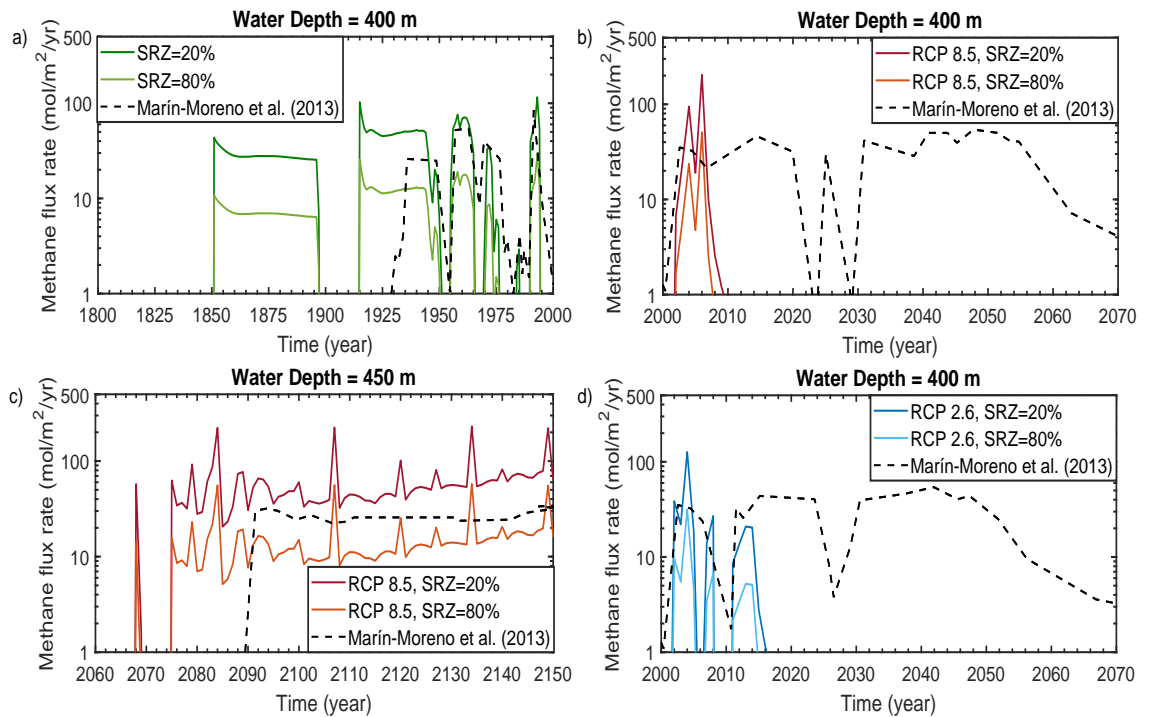
Fig. 6.7: Methane flux rates into the overlying column as a response to warming induced hydrate dissociation for three of the four simulated models. a) $z_{WD} = 400$m for 1800-2000 years b) $z_{WD} = 400$m, RCP 8.5 c) $z_{WD} = 450$m, RCP 8.5. d) $z_{WD} = 400$ m, RCP 2.6. $z_{WD} = 450$ m, RCP 2.6 is not included because as can be seen in Fig. 6.6, methane is not released over the simulated time.

this figure as it does not release gas at the top of the reservoir over the simulated time of interest.

6.1.5.1 Water depth = 400 m

The onset of methane breakthrough to the overlying water column under a water depth of 400 m is identified by a sudden spike in gas flux. Depicted in Fig. 6.7a, methane is released by 1850 due to the associated warming in Fig. 6.1a. On the contrary, this warming period does not produce methane of sizeable quantites in the model of Marín-Moreno et al. (2013) (see Fig. 2 of their supporting information) suggesting that liberated gas at the BGHSZ in their model instead remains trapped and reforms in the GHSZ. From the year 1896, there is a 19 year gap of sizeable methane release which coincides with a reduction in sea floor temperature of 0.5 ^{o}C as shown in Fig. 6.1a, leading to dissociation and related methane release to be effectively terminated.

Methane breakthrough occurs again at 1915 and is held relatively constant until 1950, at which point the sea floor temperature reduces by 0.2 ^{o}C (see Fig. 6.1b) and is enough to again terminate methane release. During this period of elevated methane flux, it can

be seen in Fig. 6.6 at 1925, that the uppermost portion of the domain is absent of hydrate and hosts 4 % of gas. Furthermore, around 20 m of hydrate has dissociated from the BGHSZ by this time and more hydrate is formed at a shallower depth from gas which has migrated away from the dissociating BGHSZ. In contrast, Marín-Moreno et al. (2013) has methane breakthrough 14 years later than the current study in 1929 and lasts until a short termination period in 1955. Recall that Marín-Moreno et al. (2013) applies a constant gas source which contributes a few $mol\,m^{-2}\,yr^{-1}$ and hence their simulated flow terminations are not as distinctly observed in Fig. 6.7. As discussed by Reagan et al. (2011), such small gas flows would add comparatively little to the flux rate compared to hydrate dissociation as even sparse hydrate contains more methane per unit volume than what would be typically found beneath the BGHSZ.

After 2005, the model response for the 400 m water depth in Fig. 6.7b and d diverge due to the different RCP scenario. The extreme warming scenario, RCP 8.5, leads to significantly elevated flux rates, peaking at more than 200 $mol\,m^{-2}\,yr^{-1}$ (SRZ= 20 %) by 2006. By contrast, the modest warming scenario, RCP 2.6, has a generally reduced methane flux rate and experiences intermittent flux terminations identified at 2006 and between 2008 and 2011. All methane in the system is released by 2010 for RCP 8.5 and by 2016 for RCP 2.6. This can be further illustrated in Fig. 6.6 for the year 2013 where a small pocket of hydrate and trapped gas remains at around 5 mbsf for the RCP 2.6 case whereas all gas is effused in the RCP 8.5 scenario at this time. Conversely, Marín-Moreno et al. (2013) maintains around 20 m of hydrate at the top of the reservoir by 2013 for the RCP 2.6 case. The major differences between these two models are: (1) the onset of methane release into the overlying water column occurs much earlier; (2) considering that the flux rates in Fig. 6.7 are dampened due to treating the SRZ as a percentage loss of mass flux unlike Marín-Moreno et al. (2013), methane is released at a generally much higher rate.

6.1.5.2   Water depth = 450 m

In the case where water depth is 450 m, it can be seen from Fig. 6.6 that around 10 m of hydrate has dissociated at the BGHSZ by 1925. This leads to further hydrate formation directly above as this dissociated gas is recycled upon migration back into the GHSZ. The model responses under both RCP scenarios are similar up to the year 2050 although Marín-Moreno et al. (2013) did not observe as significant hydrate dissociation or refor-

mation at the BGHSZ by this time. Observed at 2150 however, the responses are vastly different as RCP 8.5 has dissociated around 25 m of hydrate at the top of the reservoir whereas under RCP 2.6, no hydrate has dissociated at the sea floor. Illustrated in Fig. 6.7c, aside from the short high flux at 2068 which coincides with a sharp temperature increase of 0.8 ^{o}C in Fig. 6.1, the results by Marín-Moreno et al. (2013) are again 14 years later than the current study. Flux rate evolution over time in the 450 m water depth case is highly contrasting to that of the 400 m water depth. From 2075 onwards, methane release is relatively consistent, between 10 and 20 mol m^{-2} yr^{-1} for SRZ = 20 % and between 40 and 80 mol m^{-2} yr^{-1} for SRZ = 80 % with intermittent spikes of elevated flux rates more than 50 mol m^{-2} yr^{-1} and 200 mol m^{-2} yr^{-1} for SRZ = 20 % and 80 % respectively. This trend is not observed in the model response by Marín-Moreno et al. (2013) which maintains a more regular flux rate. These intermittent periods of high flux correspond with the sudden release of free gas at the top of the GHSZ as the last volumes of hydrate are dissociated that were otherwise trapping the gas.

6.1.5.3 Model response due to relative permeability

The shorter delays observed between the warming periods and the release of methane in this study is likely due in part to the hydrate being located at the top of the GHSZ, thus reducing the distance that the sea floor temperature must diffuse through to reach the BGHSZ. In the study by Thatcher et al. (2013), which uses comparable diffusivities to the current study, a delay between the onset of warming and subsequent methane release at the top of the reservoir could be around 15 years if the hydrate was located at the sea floor.

However, hydrate located at the sea floor in the current study is not enough to reduce the delay times between the onset of sea floor warming and methane release to the near instantaneous response observed in the simulation results. If the diffusivity is fixed, then the remaining significant control which can reduce this delay time further is by enhancing gas mobility through the handling of relative permeability. The Critical Threshold relative permeability model used in this work is compared to the Modified Stone model (see Section 2.5.1) used by Marín-Moreno et al. (2013), Thatcher et al. (2013) and others in Fig. 6.8.

From Fig. 6.8a, for high gas saturations when hydrate saturates the pore volumes above the critical hydrate saturation ($S_{hc} = 10^{-4}$), the relative permeability of gas is or-
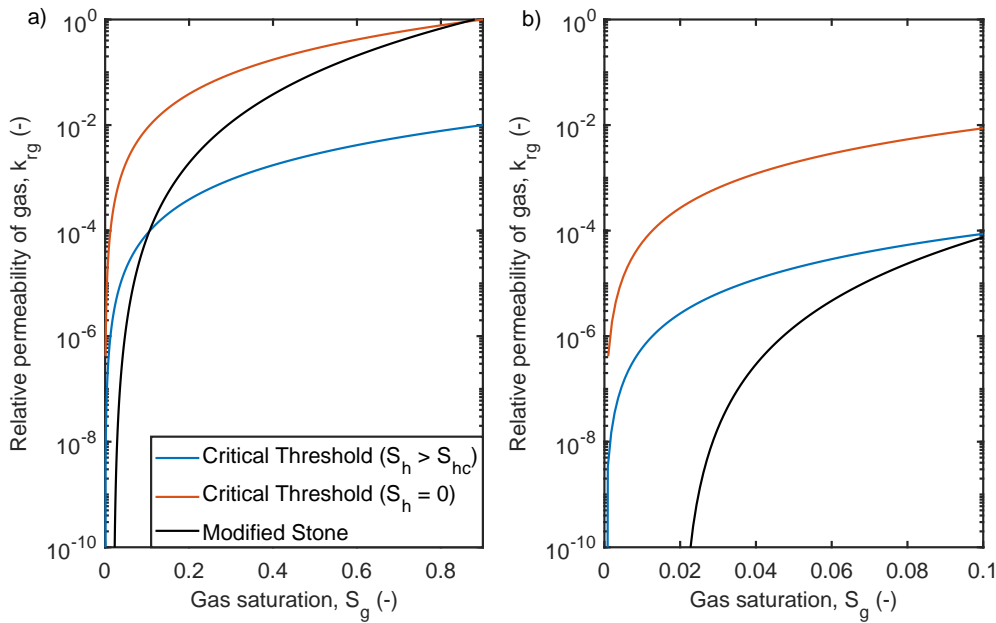
Fig. 6.8: a) Comparison of the Critical Threshold model developed in this project and the modified Stone three-phase relative permeability model used by Marín-Moreno et al. (2013). The parameters used for the Critical Threshold model can be found in Section 6.1.4.2 and the modified stone model uses: $n_g = 4$, $S_{gc} = 0.02$ and $S_{ar} = 0.12$. b) a look at the relative permeability response for lower gas saturations.

ders of magnitude less in the Critical Threshold model than the Modified Stone model. On the contrary, Fig. 6.8b shows that for lower gas saturations (i.e. less than 0.1), the Critical Threshold model is orders of magnitude more effective at mobilising gas. Most notably, when hydrate is completely dissociated, the Critical Threshold model incurs a jump in relative permeability by a factor of 100, making the two models diverge even more at low gas saturations. The Modified Stone model instead treats the gain in gas mobility through a loss of hydrate as a gain in gas saturation only, thus taking an appropriate value further up the relative permeability curve. The Modified Stone model could be inferred to ignore the variation in permeability reduction with hydrate morphology in heterogeneous porous media by assuming that increases in hydrate saturation uniformly reduces the pore volume saturated with mobile phases. On the contrary, the Critical Threshold model acknowledges that a well-placed hydrate of a small amount, such as within the pore throats, could act to drastically reduce the permeability, despite porosity remaining virtually unchanged. In this way, removal of hydrate at the top of the GHSZ can lead to sudden high fluxes of methane as can be observed in Fig. 6.7c.

The gas saturations observed in this problem are typically small, as illustrated in Fig. 6.6 and in the results by Thatcher et al. (2013) and Marín-Moreno et al. (2013). It is therefore difficult to effectively migrate gas regardless whether hydrate is present or not,

when using high relative permeability exponents in the Modified Stone model ($n_g = 4$) in contrast to the Critical Threshold model ($n_g = 2.16$). Furthermore, a residual gas saturation ($S_{gc} = 0.02$) used in the Modified Stone model prevents flow until enough gas has accumulated.

In this study, the handling of relative permeability is concluded to be an important consideration when assessing methane release rates as a response to ocean warming induced by climate change. The more mobile Critical Threshold relative permeability model coupled with hydrate poised at the sea floor (see Fig. 6 in Thatcher et al. (2013)) enables the delay time between the onset of warming and the methane release into the overlying water column to be of the order of a year or less. While Westbrook et al. (2009) does not report the observed methane flow rates, Westbrook et al. (2009) and Thatcher et al. (2013) suggest that the widespread methane release they observed was possibly due to warming 30 years prior. Thatcher et al. (2013) required a theory which included enhancing flow through a fracture network to achieve a delay time of around 30 years by permeability alone. This study has demonstrated that the choice of the relative permeability model and parameterisation as hydrate dissociates could just as equally act to reduce the delay time in hydrate saturated reservoirs with low permeabilities (recall that $k_c = k_0/100 = 96.7 \times 10^{-17}$ in the Critical Threshold model).

Not only was the delay time reduced by 14 years when compared to the study by Marín-Moreno et al. (2013), the rate of methane release into the overlying ocean waters were also significantly elevated. Crucially, the higher the methane flux rate, the more methane can bypass the sulphate reduction zone into the water column (Boetius & Wenzhöfer, 2013). Furthermore, a higher methane flux rate encourages larger methane bubble diameters which would take longer to diffuse away into the ocean and therefore more likely to reach the atmosphere (Chen et al., 2014).

Relative permeability is found to be a strong control on methane release rates. As relative permeability involving hydrate is dependent upon the distribution of hydrate-forming phases (see the discussion in Section 2.5.1), it therefore follows that capillary pressure may also be a significant control on methane release rates in regional scale methane hydrate dissociation. Small pores, either as part of the rock matrix or due to the formation of hydrate, can inhibit hydrate formation as high capillary pressure can prevent gas to enter the pore. Similarly, as hydrate dissociates, until the available pore volume for fluid phases becomes large enough, gas may become stuck and unable to flow (Clennell et al., 1999; Goel, 2006). This idea is also acknowledged through the step-wise Critical Threshold rel-

ative permeability model whereby until all the hydrate is dissociated, gas flow is limited. If gas is present in a small pore as hydrate continues to form, fracturing may occur as the gas pressure overcomes the local effective stress as Thatcher et al. (2013) suggested. Subsequently, it could be understood that methane release rates may also be dependent upon capillary pressure. However, for large pores, capillary pressure reduces and may play less of a role to inhibit gas release rates or hydrate formation. As hydrate forms and dissociates, the pore volume available for fluids to permeate reduces or increases respectively. Indeed, pore morphology may be the underlying factor controlling both the distribution of hydrate in porous media and the ability for fluids to flow. However, in the context of this regional scale study, as the porosity is large ($\phi = 0.5$) and the reservoir is assumed to be homogeneous, further formulation of the equilibrium model to include capillary pressure and sensitivity testing of the regional scale model would be required to determine whether capillary pressure is a necessary consideration or not under these simulation conditions.

Improvements have been made on previous work because no study had previously assessed the effect of utilising an alternative three-phase relative permeability model, such as the Critical Threshold model, to the widely used Modified Stone model in the context of regional scale sea floor warming induced hydrate dissociation. While Reagan et al. (2011) and Thatcher et al. (2013) did perform a degree of sensitivity analysis on methane release rates by changing the permeability of the rock absent of hydrate and, also in the case of the latter, the residual gas saturation, they both used the same Modified Stone model with the same relative permeability exponents. While there is an intrinsic relationship between the residual saturation and the relative permeability exponent, this relationship is less coupled for low gas saturations as flow cannot begin until gas saturation exceeds the residual.

The Critical Threshold model applied for comparison to the simulations by Marín-Moreno et al. (2013) was derived from the work in Chapter 4 and based upon real data of a real hydrate-saturated rock with a similar rock permeability in the absence of hydrate. It was found that the handling of relative permeability in regional scale modelling is a major consideration and utilising different models can lead to significantly different responses of the hydrate saturated reservoir.

6.1.6   Summary and conclusions

The objective of this preliminary work was to assess how using an alternative three-phase relative permeability model and parameterisation to existing studies affected the evolution

of a methane hydrate saturated reservoir as it responded to ocean warming. The reservoir simulated used characteristics and data related to the West Svalbard area to enable direct comparison with the modelling results presented by Marín-Moreno et al. (2013).

Previous modelling attempts of regional scale hydrate dissociation problems in the context of climate change consistently use the same three-phase relative permeability model, the so-called "Modified Stone three phase relative permeability model" with almost identical parameterisation (Reagan & Moridis, 2008; Reagan et al., 2011; Thatcher et al., 2013; Marín-Moreno et al., 2013, 2015a,b; Stranne et al., 2016a,b).

This study improves on previous work by using an alternative three-phase relative permeability model, the "Critical Threshold" model, developed in this project alongside relative permeability parameterisation determined from real laboratory scale data in Chapter 4.

It was found that utilising a different three-phase relative permeability model can lead to a significantly different response of a hydrate saturated reservoir with the onset of ocean warming. The mathematical model in this study led to a less than year delay between the onset of ocean warming and methane emissions at the sea floor compared to around 15 years for similar conditions by Thatcher et al. (2013). While one reason for this is that the top of the hydrate saturated reservoir lies at the sea floor (Thatcher et al., 2013), enhanced gas mobility through the relative permeability model also significantly contributed to minimising the delay time to around a year. The GHSZ also diminishes quicker with an elevated gas relative permeability as less liberated gas becomes re-trapped within the GHSZ and the methane flux rates were also found to be generally enhanced in this study compared to Marín-Moreno et al. (2013).

It is suggested that for future MCMP problems investigating methane hydrate dissociation in a regional scale context, where there is a lack of data to constrain the mathematical model, a broad parameter sensitivity analysis should be performed to understand the range of possible methane flux rates. Future sensitivity analyses that use the Modified Stone model should include but are not limited to: (1) the intrinsic permeability of the rock absent of hydrate; (2) the depth to the top of the hydrate reservoir, which could be interpreted as the thickness of the SRZ; (3) the reservoir porosity; (4) the irreducible phase saturations; (5) as not previously performed but important due to the generally low gas saturations associated with marine GHSZs, the relative permeability exponents. Where possible, alternative three-phase relative permeability models should be developed and tested for regional scale problems to provide a broader selection of appropriate models

and lessen the over-reliance on the Modified Stone model.

6.2   Recommendations for further work

The kinetic model in Chapter 4 was shown to be particularly effective at simulating methane hydrate dissociation requiring minimal spatial resolution in discretisation and reasonable computation times. This model could be used to investigate the parameterisations of further experimental datasets such as the experiment performed by Yousif et al. (1991). The kinetic model could also be extended to include further complexity such as the partial miscibility of methane and water components. in aqueous and gaseous phases respectively, and allow ice to form. Additional phases do not require more primary dependent variables and governing equations, but rather necessitate compositional considerations into the thermodynamic equations of state. Introducing an ice phase would be of interest because it would allow laboratory scale modelling of conditions analogous to permafrost methane hydrate, which this model is unable to presently do.

Following the preliminary study in Section 6.1, a thorough sensitivity analysis of the Critical Threshold model on the regional scale, sea floor warming induced hydrate dissociation scenario should be carried out. Doing so would enable the effect of relative permeability to be better understood in this context and to compare better the Critical Threshold model as a viable alternative to the Modified Stone model.

The equilibrium model could also be extended to include typical capillary pressure functions to help assess its role on methane release rates in regional scale scenarios. However, significant work is necessary to determine how best to formulate capillary pressure in the context of methane hydrates as seldom literature currently investigates on the subject.

The highly oscillating sea floor temperature boundary condition used in Section 6.1 coupled with the cyclical dissociation and formation of hydrate in proximity to this boundary can lead to very large computation times. Further testing of the equilibrium model under different regional scale scenarios would help assess the robustness and limits of this model. One such good test case that could be utilised in future work would be to make the equilibrium model radially axisymmetric and simulate depressurisation of a hydrate-bearing reservoir emanating from a fully penetrating well. With real world depressurisation tests ongoing, particularly in the Nankai trough, Japan, this exercise would be both a good assessment of the model limitations and relevant to existing research.

Appendix A

INCORPORATING CAPILLARY PRESSURE INTO THE CORE SCALE SIMULATIONS

It was found through preliminary testing that capillary pressure could be ignored during simulation under the conditions of the experiment by Masuda et al. (1999). Apart from Liang et al. (2010), studies attempting to simulate the Masuda experiment also ignored capillary pressure (Ruan et al., 2012a; Zhao et al., 2012a; Nazridoust & Ahmadi, 2007; Shin, 2014; Chen et al., 2016). This appendix describes the additional formulation used to include capillary pressure to the core scale model in Chapter 4 and provides a graphical comparison to the model without capillary pressure.

Capillary pressure, P_c [ML^{-1}T^{-2}] is defined as the difference between the wetting and the non-wetting phase as

$$P_c = P_g - P_a \tag{A.1}$$

A common function used to handle capillary pressure is through the soil-water retention model devised by van Genuchten (1980). This can be represented as follows

$$P_c = P_{c0} \left(S_e^{-\frac{1}{m_v}} - 1 \right)^{\frac{1}{n_v}} \tag{A.2}$$

where P_{c0} (= 19,600 Pa) [ML-1T^{-2}] is the capillary entry pressure, m_v (= 0.254) [-] and $n_v = \frac{1}{1-m_v}$ [-] are empirical van Genuchten parameters related to the soil-water characteristics and S_e [-] is the effective water saturation. The parameters are taken from the regional scale hydrate dissociation study by Marín-Moreno et al. (2013). Capillary pressure increases with increasing hydrate saturation due to a reduction in pore volume Sun et al. (2014). If the growth of hydrate can be considered to form the framework of the porous media, then the effective aqueous saturation is normalised with respect to the effective pore volume such that S_e is given as

$$S_e = \frac{S_a^* - S_{ar}}{1 - S_{ar}} \tag{A.3}$$
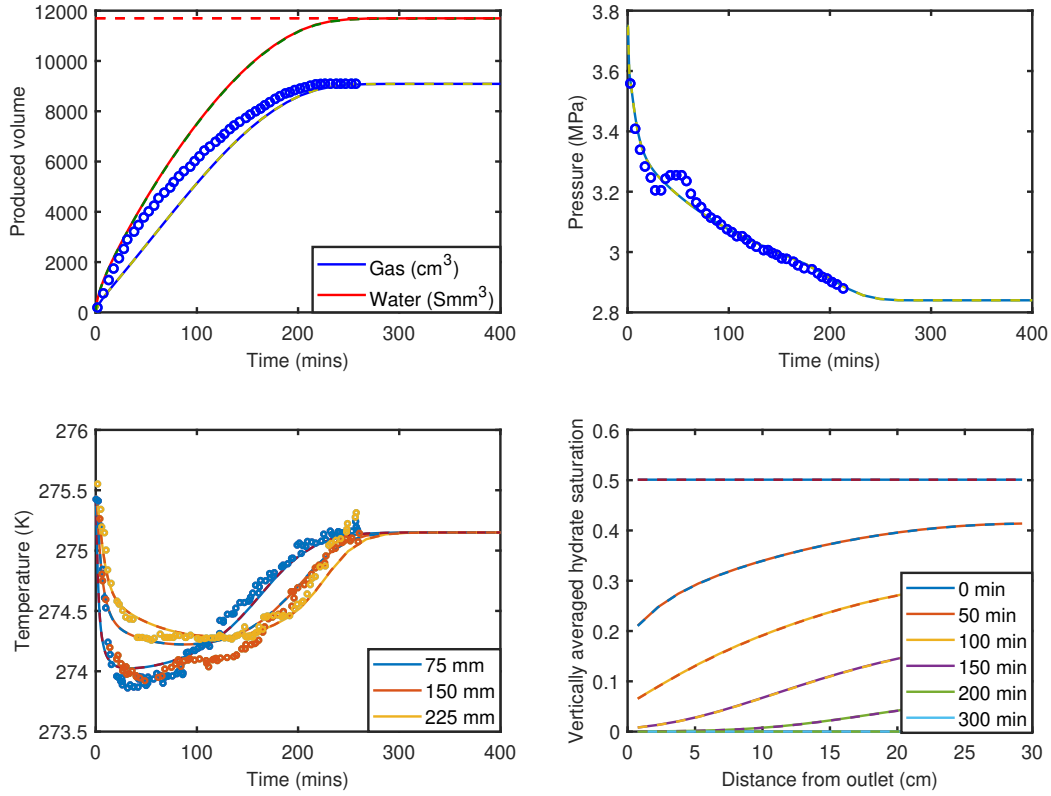
Fig. A.1: A comparison of the simulation results for Run 4 with and without capillary pressure included. The model outputs are indistinguishable.

where

$$S_j^* = \frac{S_j}{1 - S_h}, \qquad j = g, a \tag{A.4}$$

Assuming that pressure is distributed proportionally to the available phases it follows that

$$P = \sum_j S_j^* P_j, \qquad j = g, a \tag{A.5}$$

Substituting Eq. (A.1) into Eq. (A.5) gives an expression for the gaseous and aqueous phase pressures.

$$P_g = P + S_a^* P_c \tag{A.6}$$

$$P_a = P - S_g^* P_c \tag{A.7}$$

These phase pressures then replace the global pressure, P, in the Darcy's flow rate term of the mass conservation statement in Eq. (2.19) and the energy conservation statement in Eq. (2.58).

Fig. A.1 shows that including capillary pressure makes negligible difference to the simulation results.

Appendix B

ALTERNATIVE CALIBRATIONS TO THE CORE SCALE EXPERIMENT

In Chapter 4, the core scale model described therein was calibrated to Run 4 of the Masuda experiment (Masuda et al., 1999) by optimising three unknown parameters: the relative permeability exponents of aqueous and gaseous phases, n_a and n_g respectively; and the convective heat transfer coefficient, γ. The calibrated parameters were then used to forecast Run 2 and 3 of the experiment to verify the results. Alternatively, calibrations to Run 2 or Run 3 could have been made and the modelling results used to forecast the remaining two runs.

Calibrating the three parameters to different individual runs leads to different outputs of n_a, n_g and γ, as shown in Table B.1.

	Run 2	Run 3	Run 4
n_a	0.75	0.70	0.93
n_g	2.21	2.16	2.15
γ	51.42	51.12	55.40

Tab. B.1: Summary of the outputs after calibrating the unknown parameters: n_a, n_g and γ to the individual runs.

The most significant difference between calibrating the three runs separately in Table B.1 is the value of the relative permeability exponent for the aqueous phase, n_a. The key outputs from Chapter 4 were the gas production data, water production data, boundary pressure evolution data and temperature evolution at three locations within the core. However, from Figs. B.1 and B.2, it can be seen that although using a different value of n_a does lead to a better of simulation of the total water produced from the core, the effects on the rest of the data are comparatively marginal.
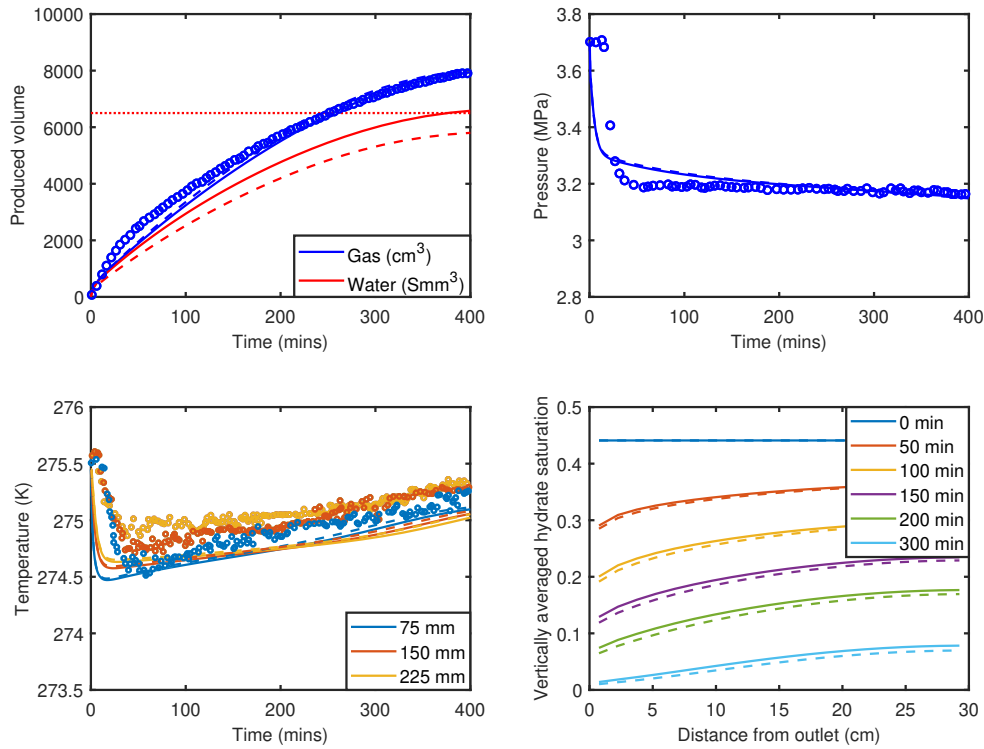
Fig. B.1: A comparison of calibrating the core scale model in Chapter 4 to Run 2 directly (solid lines) with using the optimised parameters from calibrating to Run 4 as default in Chapter 4 (dashed lines). Dotted lines or circular markers are the experimental data.
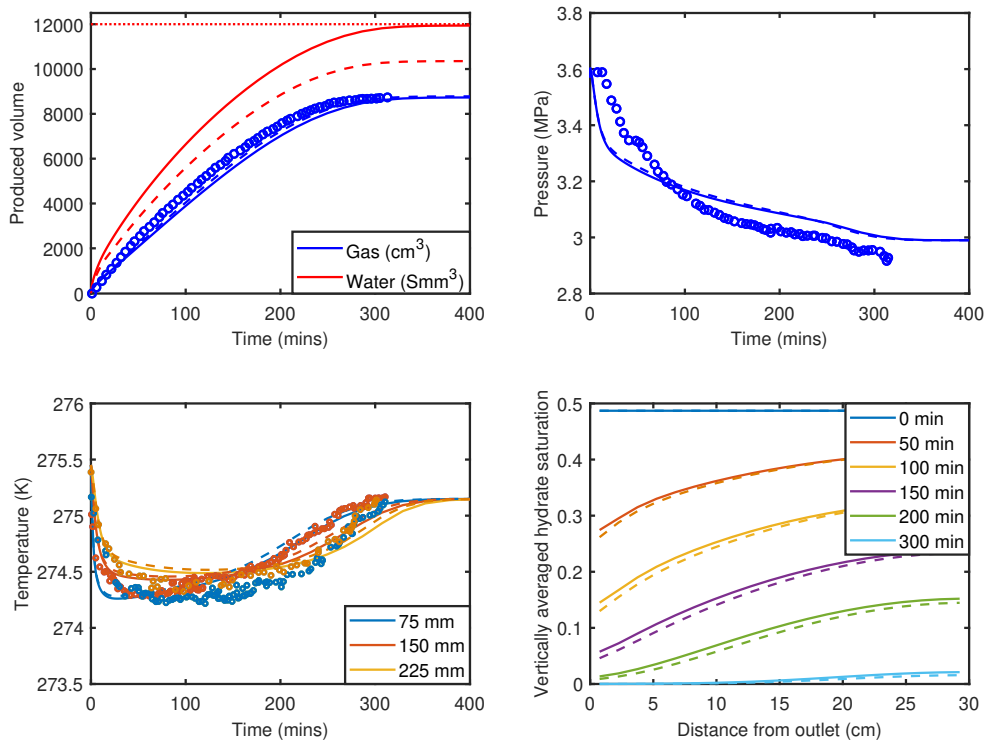

Fig. B.2: As Fig. B.1 but for Run 3.

BIBLIOGRAPHY

Ahmed, T., (2001) Reservoir Engineering Handbook. Springer, London

Ahmadi, G., Ji, C., & Smith, D. H. (2007). Natural gas production from hydrate dissociation: An axisymmetric model. Journal of petroleum science and engineering, 58(1), 245-258.

Ahn, T., Lee, J., Huh, D. G., & Kang, J. M. (2005). Experimental study on two-phase flow in artificial hydrate-bearing sediments. Geosystem Engineering, 8(4), 101-104.

Archer, D., B. Buffett, and V. Brovkin (2009), Ocean methane hydrates as a slow tipping point in the global carbon cycle, Proc. Natl. Acad. Sci. U. S. A., 106(49), 20,59620,601.

Anderson, G. K. (2004). Enthalpy of dissociation and hydration number of methane hydrate from the Clapeyron equation. The Journal of Chemical Thermodynamics, 36(12), 1119-1127.

Anderson, B. J., Kurihara, M., White, M. D., Moridis, G. J., Wilson, S. J., Pooladi-Darvish, M., ... & Narita, H. (2011). Regional long-term production modeling from a single well test, Mount Elbert gas hydrate stratigraphic test well, Alaska North slope. Marine and petroleum geology, 28(2), 493-501.

Amaziane, B., Jurak, M., & Zgaljic-Keko, A. (2012). Modeling compositional compressible two-phase flow in porous media by the concept of the global pressure. In ECMOR XIII-13th European Conference on the Mathematics of Oil Recovery.

Batzle, M., & Wang, Z. (1992). Seismic properties of pore fluids. Geophysics, 57(11), 1396-1408.

Bangs, N. L., Hornbach, M. J., Moore, G. F., & Park, J. O. (2010). Massive methane release triggered by seafloor erosion offshore southwestern Japan. Geology, 38(11), 1019-1022.

Bear, J. (2018). Modelling Phenomena of Flow and Transport in Porous Media (Vol. 31). Springer.

Berndt, C., Feseker, T., Treude, T., Krastel, S., Liebetrau, V., Niemann, H., ... & Graves, C. (2014). Temporal constraints on hydrate-controlled methane seepage off Svalbard. Science, 343(6168), 284-287.

Biastoch, A., Treude, T., Rpke, L. H., Riebesell, U., Roth, C., Burwicz, E. B., ... & Wallmann, K. (2011). Rising Arctic Ocean temperatures cause gas hydrate destabilization and ocean acidification. Geophysical Research Letters, 38(8).

Birkedal, K. A., Freeman, C. M., Moridis, G. J., & Graue, A. (2014). Numerical predictions of experimentally observed methane hydrate dissociation and reformation in sandstone. Energy & Fuels, 28(9), 5573-5586.

Bjerrum, C. J., & Canfield, D. E. (2011). Towards a quantitative understanding of the late Neoproterozoic carbon cycle. Proceedings of the National Academy of Sciences, 108(14), 5542-5547.

Bourgeat, A., Jurak, M.,& Smaï, F. (2013). On persistent primary variables for numerical modeling of gas migration in a nuclear waste repository. Computational geosciences, 17(2), 287-305.

Bock, M., Schmitt, J., Mller, L., Spahni, R., Blunier, T., & Fischer, H. (2010). Hydrogen isotopes preclude marine hydrate CH4 emissions at the onset of Dansgaard-Oeschger events. Science, 328(5986), 1686-1689.

Boetius, A., & Wenzhöfer, F. (2013). Seafloor oxygen consumption fuelled by methane from cold seeps. Nature Geoscience, 6(9), 725.

Borowski, W. S., Paull, C. K., & Ussler, W. (1997). Carbon cycling within the upper methanogenic zone of continental rise sediments; an example from the methane-rich sediments overlying the Blake Ridge gas hydrate deposits. Marine Chemistry, 57(3), 299-311.

Buffett, B. A., & Zatsepina, O. Y. (2000). Formation of gas hydrate from dissolved gas in natural porous media. Marine geology, 164(1), 69-77.

Buffett, B., & Archer, D. (2004). Global inventory of methane clathrate: sensitivity to changes in the deep ocean. Earth and Planetary Science Letters, 227(3-4), 185-199.

Burwicz, E., L. Rpke, and K. Wallmann (2011), Estimation of the global amount of submarine gas hydrates formed via microbial methane formation based on numerical reaction-transport modeling and a novel parameterization of Holocene sedimentation, Geochim. Cosmochim. Acta, 16, 45624576, doi:10.1016/j.gca.2011.05.029.

Boswell, R., & Collett, T. S. (2011). Current perspectives on gas hydrate resources. Energy & environmental science, 4(4), 1206-1215.

Boswell, R., Collett, T. S., Frye, M., Shedd, W., McConnell, D. R., & Shelander, D. (2012). Subsurface gas hydrates in the northern Gulf of Mexico. Marine and Petroleum Geology, 34(1), 4-30.

Cellier, F. E., & Kofman, E. (2006). Continuous system simulation. Springer Science & Business Media.

Cengel, Y. A., & Boles, M. A. (2002). Thermodynamics: an engineering approach. Sea, 1000, 8862.

Chen, Z., Huan, G., & Ma, Y. (2006). Computational methods for multiphase flows in porous media (Vol. 2). Siam.

Chen, L., Levine, J. S., Gilmer, M. W., Sloan, E. D., Koh, C. A., & Sum, A. K. (2014). Methane hydrate formation and dissociation on suspended gas bubbles in water. Journal of Chemical & Engineering Data, 59(4), 1045-1051.

Chen, L., Yamada, H., Kanda, Y., Lacaille, G., Shoji, E., Okajima, J., ... & Maruyama, S. (2016). Numerical analysis of core-scale methane hydrate dissociation dynamics and multiphase flow in porous media. Chemical Engineering Science, 153, 221-235.

Chen, L., Yamada, H., Kanda, Y., Okajima, J., Komiya, A., & Maruyama, S. (2017). Investigation on the dissociation flow of methane hydrate cores: Numerical modeling and experimental verification. Chemical Engineering Science, 163, 31-43.

Civan, F. (2001). Scale effect on porosity and permeability: Kinetics, model, and correlation. AIChE journal, 47(2), 271-287.

Clarke, M. A., & Bishnoi, P. R. (2001). Measuring and modelling the rate of decomposition of gas hydrates formed from mixtures of methane and ethane. Chemical Engineering Science, 56(16), 4715-4724.

Clarke, M., & Bishnoi, P. R. (2001b). Determination of the activation energy and intrinsic rate constant of methane gas hydrate decomposition. The Canadian Journal of Chemical Engineering, 79(1), 143-147.

Clauser, C., & Huenges, E. (1995). Thermal conductivity of rocks and minerals. Rock physics & phase relations: a handbook of physical constants, 105-126.

Clennell, M. B., Hovland, M., Booth, J. S., Henry, P., & Winters, W. J. (1999). Formation of natural gas hydrates in marine sediments: 1. Conceptual model of gas hydrate growth conditioned by host sediment properties. Journal of Geophysical Research: Solid Earth, 104(B10), 22985-23003.

Corey, A. T. (1954). The interrelation between gas and oil relative permeabilities. Producers monthly, 19(1), 38-41.

Collett, T. S., Lee, M. W., Agena, W. F., Miller, J. J., Lewis, K. A., Zyrianova, M. V., Boswell, R., Inks, T. L. (2011). Permafrost-associated natural gas hydrate occurrences on the Alaska North Slope. Marine and Petroleum Geology, 28(2), 279-294.

Collett, T., Bahk, J. J., Baker, R., Boswell, R., Divins, D., Frye, M., ... & Morell, M. (2014). Methane Hydrates in Nature - Current Knowledge and Challenges. Journal of Chemical & Engineering Data, 60(2), 319-329.

Collins, W. J., Bellouin, N., Doutriaux-Boucher, M., Gedney, N., Halloran, P., Hinton, T., ... & Martin, G. (2011). Development and evaluation of an Earth-System model-HadGEM2. Geoscientific Model Development, 4(4), 1051.

Covert, T., Greenstone, M., & Knittel, C. R. (2016). Will we ever stop using fossil fuels?. The Journal of Economic Perspectives, 30(1), 117-137.

Crank, J., (1975). The Mathematics of Diffusion. Springer.

Crutchley, G. J., Mountjoy, J. J., Pecher, I. A., Gorman, A. R., & Henrys, S. A. (2016). Submarine slope instabilities coincident with shallow gas hydrate systems: insights from New Zealand examples. In Submarine Mass Movements and their Consequences (pp. 401-409). Springer International Publishing.

Dallimore, S. R., & Collett, T. S. (1995). Intrapermafrost gas hydrates from a deep core hole in the Mackenzie Delta, Northwest Territories, Canada. Geology, 23(6), 527-530.

Dallimore, S. R., T. S. Collett, A. E. Taylor, T. Uchida, M. Weber, A. Chandra, T. H. Mroz, E. M. Caddel, and T. Inoue (2005). Scientific results from the Mallik 2002 gas hydrate production research well program, Mackenzie Delta, northwest territories, Canada: Preface. Bulletin of the Geological Survey of Canada 585 .

Davis, M. E. (2013). Numerical methods and modeling for chemical engineers. Courier Corporation.

Delli, M. L., & Grozic, J. L. (2013). Prediction performance of permeability models in gas-hydrate-bearing sands. Spe Journal, 18(02), 274-284.

Dickens, G. R., & QuinbyHunt, M. S. (1994). Methane hydrate stability in seawater. Geophysical Research Letters, 21(19), 2115-2118.

Dickens, G. R., O'Neil, J. R., Rea, D. K., & Owen, R. M. (1995). Dissociation of oceanic methane hydrate as a cause of the carbon isotope excursion at the end of the Paleocene. Paleoceanography, 10(6), 965-971.

Dickens, G. R., Castillo, M. M., & Walker, J. C. (1997). A blast of gas in the latest Paleocene: Simulating first-order effects of massive dissociation of oceanic methane hydrate. Geology, 25(3), 259-262.

Dickens, G. R. (2011). Down the rabbit hole: Toward appropriate discussion of methane release from gas hydrate systems during the Paleocene-Eocene thermal maximum and other past hyperthermal events. Climate of the Past, 7(3), 831-846.

Daigle, H. (2016). Relative permeability to water or gas in the presence of hydrates in porous media from critical path analysis. Journal of Petroleum Science and Engineering, 146, 526-535.

Englezos, P., Kalogerakis, N., Dholabhai, P. D., & Bishnoi, P. R. (1987). Kinetics of gas hydrate formation from mixtures of methane and ethane. Chemical Engineering Science, 42(11), 2659-2666.

Englezos, P., & Lee, J. D. (2005). Gas hydrates: A cleaner source of energy and opportunity for innovative technologies. Korean Journal of Chemical Engineering, 22(5), 671-681.

Frieling, J., Peterse, F., Lunt, D. J., Bohaty, S. M., S Sinninghe Damst, J., Reichart, G. J., & Sluijs, A. (2016). A Smoking Gun for Methane Hydrate Release During the Paleocene-Eocene Thermal Maximum. In AGU Fall Meeting Abstracts.

Frye, M. (2008). Preliminary evaluation of in-place gas hydrate resources: Gulf of Mexico outer continental shelf: Minerals Management Service Report 2008-004. GasHydrate-Assessment. htm.

Fuji, T., T. Saeki., T. Kobayashi., T. Inamori., M. Hayashi, O. Takano., T. Takayama, T. Kawasaki., S. Nagakubo., M. Nakamizu., K. Yokoi. (2008) Resource Assessment of Methane Hydrate in the Eastern Nankai Trough, Japan. Offshore Technology Conference, Paper Number OTC 19310.

Gamwo, I. K., & Liu, Y. (2010). Mathematical modeling and numerical simulation of methane production in a hydrate reservoir. Industrial & engineering chemistry research, 49(11), 5231-5245.

Gent, P. R., Danabasoglu, G., Donner, L. J., Holland, M. M., Hunke, E. C., Jayne, S. R., ... & Worley, P. H. (2011). The community climate system model version 4. Journal of Climate, 24(19), 4973-4991.

Giustiniani, M., Tinivella, U., Jakobsson, M., & Rebesco, M. (2013). Arctic ocean gas hydrate stability in a changing climate. Journal of Geological Research, 2013.

Goudarzi, S., Mathias, S. A., & Gluyas, J. G. (2016). Simulation of three-component two-phase flow in porous media using method of lines. Transport in Porous Media, 112(1), 1-19.

Goel, N., Wiggins, M.,& Shah, S. (2001). Analytical modeling of gas recovery from in situ hydrates dissociation. Journal of Petroleum Science and Engineering, 29(2), 115-127.

Goel, N. (2006). In situ methane hydrate dissociation with carbon dioxide sequestration: Current knowledge and issues. Journal of petroleum science and engineering, 51(3-4), 169-184.

Gupta, A., Lachance, J., Sloan Jr, E. D., & Koh, C. A. (2008). Measurements of methane hydrate heat of dissociation using high pressure differential scanning calorimetry. Chemical Engineering Science, 63(24), 5848-5853.

Haq, S., Hussain, A., & Uddin, M. (2012). On the numerical solution of nonlinear Burgers-type equations using meshless method of lines. Applied Mathematics and Computation, 218(11), 6280-6290.

Hardwick, J. S., & Mathias, S. A. (2017). Masudas sandstone core hydrate dissociation experiment revisited. Chemical Engineering Science.

Handa, Y. P., & Stupin, D. Y. (1992). Thermodynamic properties and dissociation characteristics of methane and propane hydrates in 70-. ANG.-radius silica gel pores. The Journal of Physical Chemistry, 96(21), 8599-8603.

Hammerschmidt, E. G., (1934) Formation of gas hydrates in natural gas transmission lines. Industrial & Engineering Chemical Research Vol 26, 851-855

Heinrich, H. (1988). Origin and consequences of cyclic ice rafting in the northeast Atlantic Ocean during the past 130,000 years. Quaternary research, 29(2), 142-152.

Hoffman, P. F., Kaufman, A. J., Halverson, G. P., & Schrag, D. P. (1998). A Neoproterozoic snowball earth. science, 281(5381), 1342-1346.

Hutchinson, D., C. Ruppel, H. Roberts, R. Carney, M. Smith (2011). Gas hydrates in the Gulf of Mexico. C. Holmes (Ed.), Gulf of Mexico; Its Origin, Waters, and Biota, Texas A&M University Press

Hunter, S. J., Goldobin, D. S., Haywood, A. M., Ridgwell, A., & Rees, J. G. (2013). Sensitivity of the global submarine hydrate inventory to scenarios of future climate change. Earth and Planetary Science Letters, 367, 105-115.

Husebø, J., Ersland, G., Graue, A., & Kvamme, B. (2009). Effects of salinity on hydrate stability and implications for storage of CO_2 in natural gas hydrate reservoirs. Energy Procedia, 1(1), 3731-3738.

Hyndman, R. D., & Spence, G. D. (1992). A seismic study of methane hydrate marine bottom simulating reflectors. Journal of Geophysical Research: Solid Earth, 97(B5), 6683-6698.

IEA (2016), World Energy Outlook 2016, IEA, Paris.

Jaiswal, N. J., Dandekar, A. Y., Patil, S. L., Hunter, R. B., & Collett, T. S. (2009). Relative permeability measurements of gas-water-hydrate systems.

Ji, C., Ahmadi, G.,& Smith, D. H. (2001). Natural gas production from hydrate decomposition by depressurization. Chemical Engineering Science, 56(20), 5801-5814.

Jiang, G., S. Xiaoying, Z. Shihong,. (2006). Methane seeps, methane hydrate destabilization, and the late Neoproterozoic postglacial cap carbonates. Chinese Science Bulletin, 51(10),1152-1173

Johnson, A., Patil, S., & Dandekar, A. (2011). Experimental investigation of gas-water relative permeability for gas-hydrate-bearing sediments from the Mount Elbert Gas Hydrate Stratigraphic Test Well, Alaska North Slope. Marine and petroleum geology, 28(2), 419-426.

Kerkar, P., Jones, K. W., Kleinberg, R., Lindquist, W. B., Tomov, S., Feng, H., & Mahajan, D. (2009). Direct observations of three dimensional growth of hydrates hosted in porous media. Applied physics letters, 95(2), 024102.

Kennedy, M., Mrofka, D., & Von Der Borch, C. (2008). Snowball Earth termination by destabilization of equatorial permafrost methane clathrate. Nature, 453(7195), 642.

Kennett, J. P., Cannariato, K. G., Hendy, I. L., & Behl, R. J. (2003). Methane hydrates in quaternary climate change: the clathrate gun hypothesi (pp. 1-9). American Geophysical Union.

Kim, H. C., Bishnoi, P. R., Heidemann, R. A., & Rizvi, S. S. (1987). Kinetics of methane hydrate decomposition. Chemical engineering science, 42(7), 1645-1653.

Klauda, J. B., S. Sandler (2003). Predictions of gas hydrate phase equilibria and amounts in natural sediment porous media. J. Mar. Pet. Geol., 20 (5) (2003), pp. 459-470

Klauda, J. B., & Sandler, S. I. (2005). Global distribution of methane hydrate in ocean sediment. Energy & Fuels, 19(2), 459-470.

Kleinberg, R. L., Flaum, C., Griffin, D. D., Brewer, P. G., Malby, G. E., Peltzer, E. T., & Yesinowski, J. P. (2003). Deep sea NMR: Methane hydrate growth habit in porous media and its relationship to hydraulic permeability, deposit accumulation, and submarine slope stability. Journal of Geophysical Research: Solid Earth, 108(B10).

Kneafsey, T. J., Tomutsa, L., Moridis, G. J., Seol, Y., Freifeld, B. M., Taylor, C. E., & Gupta, A. (2007). Methane hydrate formation and dissociation in a partially saturated core-scale sand sample. Journal of Petroleum Science and Engineering, 56(1), 108-126.

Kneafsey, T. J., Seol, Y., Gupta, A., & Tomutsa, L. (2011). Permeability of laboratory-formed methane-hydrate-bearing sand: measurements and observations using X-ray computed tomography. Spe Journal, 16(01), 78-94.

Krey, V., Canadell, J. G., Nakicenovic, N., Abe, Y., Andruleit, H., Archer, D., ... & Lamarque, J. F. (2009). Gas hydrates: entrance to a methane age or climate threat?. Environmental Research Letters, 4(3), 034007.

Kretschmer, K., A. Biastoch, L. Rpke, and E. Burwicz (2015) Modeling the fate of methane hydrates under global warming *Global Biogeochem. Cycles, 29* 610-625

Konno, Y., Masuda, Y., Takenaka, T., Oyama, H., Ouchi, H., Kurihara, M., (2008). Relative permeability curves during hydrate dissociation in depressurization. In: Proceedings of the 6th International Conference on Gas Hydrates (ICGH).

Konno, Y., Jin, Y., Uchiumi, T., & Nagao, J. (2013). Multiple-pressure-tapped core holder combined with X-ray computed tomography scanning for gaswater permeability measurements of methane-hydrate-bearing sediments. Review of scientific instruments, 84(6), 064501.

Konno, Y., Yoneda, J., Egawa, K., Ito, T., Jin, Y., Kida, M., ... & Nagao, J. (2015). Permeability of sediment cores from methane hydrate deposit in the Eastern Nankai Trough. Marine and Petroleum Geology, 66, 487-495.

Kowalsky, M. B., & Moridis, G. J. (2007). Comparison of kinetic and equilibrium reaction models in simulating gas hydrate behavior in porous media. Energy Conversion and Management, 48(6), 1850-1863.

Kumar, A., Maini, B., Bishnoi, P. R., Clarke, M., Zatsepina, O., & Srinivasan, S. (2010). Experimental determination of permeability in the presence of hydrates and its effect on the dissociation characteristics of gas hydrates in porous media. Journal of Petroleum Science and Engineering, 70(1-2), 114-122.

Kumar, A., Maini, B., Bishnoi, P. R., & Clarke, M. (2013). Investigation of the variation of the surface area of gas hydrates during dissociation by depressurization in porous media. Energy & Fuels, 27(10), 5757-5769.

Kurihara, M., Sato, A., Ouchi, H., Narita, H., Ebinuma, T., Suzuki, K., ... & Fujii, T. (2010, May). Prediction of production test performances in eastern Nankai Trough

methane hydrate reservoirs using 3D reservoir model. In Offshore Technology Conference.

Kvenvolden, K. A. (1993). Gas hydratesgeological perspective and global change. Reviews of geophysics, 31(2), 173-187.

Kvenvolden, K. A. (1995). A review of the geochemistry of methane in natural gas hydrate. Organic geochemistry, 23(11), 997-1008.

Lemmon, E. E., M. O. McLinden and D. G. Friend., (2013) Thermophysical properties of fluid systems. In: NIST Chemistry WebBook, NIST Standard Reference Database, Vol 69, National Institute of Standards and Technology, (online).

LeVeque, R. J. Numerical Methods for Conservation Laws. 1992. Birkhaøuser Basel.

Li, B., Li, X. S., Li, G., Jia, J. L., & Feng, J. C. (2013). Measurements of water permeability in unconsolidated porous media with methane hydrate formation. Energies, 6(7), 3622-3636.

Li, M., Fan, S., Su, Y., Ezekiel, J., Lu, M., & Zhang, L. (2015). Mathematical models of the heat-water dissociation of natural gas hydrates considering a moving Stefan boundary. Energy, 90, 202-207.

Li, A., Davies, R. J., Mathias, S., Yang, J., Hobbs, R., & Wilson, M. (2017). Gas venting that bypasses the feather edge of marine hydrate, offshore Mauritania. Marine and Petroleum Geology.

Li, N., Sun, Z. F., Sun, C. Y., Li, P., Chen, G. J., Ma, Q. L., & Liu, B. (2018). Simulating natural hydrate formation and accumulation in sediments from dissolved methane using a large three-dimensional simulator. Fuel, 216, 612-620.

Liang, H., Song, Y., & Chen, Y. (2010). Numerical simulation for laboratory-scale methane hydrate dissociation by depressurization. Energy Conversion and Management, 51(10), 1883-1890.

Liang, H., Song, Y., Chen, Y., & Liu, Y. (2011). The measurement of permeability of porous media with methane hydrate. Petroleum Science and Technology, 29(1), 79-87.

Liu, Y.,& Gamwo, I. K. (2012). Comparison between equilibrium and kinetic models for methane hydrate dissociation. Chemical engineering science, 69(1), 193-200.

Lu, Z., & Sultan, N. (2008). Empirical expressions for gas hydrate stability law, its volume fraction and mass-density at temperatures 273.15 K to 290.15 K. Geochemical Journal, 42(2), 163-175.

Majorowicz, J. A., Osadetz, K. G., Safanda, J. (2008, July). Onset and stability of gas hydrates under permafrost in an environment of surface climatic change-past and future. In Proceedings of the 6th International Conference on Gas Hydrates (ICGH VI, 2008), Vancouver, British Columbia, Canada.

Makogon, Y.F., Trebin, F.A., Trofimuk, A.A., and Cherskii, V.P., (1971), Detection of a pool of natural gas in a solid hydrate state: Doklady Akademii Nauk SSSR, v. 196, n.1, p. 197-200.

Makogon, I. F. (1997). Hydrates of hydrocarbons. Pennwell Books.

Makogon, Y. F. (2010). Natural gas hydratesA promising source of energy. Journal of Natural Gas Science and Engineering, 2(1), 49-59.

Mallison, B. T., Gerritsen, M. G., Jessen, K., & Orr, F. M. (2005). High order upwind schemes for two-phase, multicomponent flow. SPE Journal, 10(03), 297-311.

Maslin, M., Owen, M., Day, S., & Long, D. (2004). Linking continental-slope failures and climate change: Testing the clathrate gun hypothesis. Geology, 32(1), 53-56.

MASUDA, Y. (1999). Modeling and experimental studies on dissociation of methane gas hydrate in Berea sandstone cores. In Proc. 3rd International Conference on Gas Hydrates, 1999.

Marín-Moreno, H., Minshull, T. A., Westbrook, G. K., Sinha, B., & Sarkar, S. (2013). The response of methane hydrate beneath the seabed offshore Svalbard to ocean warming during the next three centuries. Geophysical Research Letters, 40(19), 5159-5163.

MaríMoreno, H., Minshull, T. A., Westbrook, G. K., & Sinha, B. (2015). Estimates of future warminginduced methane emissions from hydrate offshore west Svalbard for a range of climate models. Geochemistry, Geophysics, Geosystems, 16(5), 1307-1323.

Marn-Moreno, H., Giustiniani, M., & Tinivella, U. (2015). The potential response of the hydrate reservoir in the South Shetland Margin, Antarctic Peninsula, to ocean warming over the 21st century. Polar Research, 34(1), 27443.

Mathias, S. A., McElwaine, J. N.,& Gluyas, J. G. (2014). Heat transport and pressure buildup during carbon dioxide injection into depleted gas reservoirs. Journal of Fluid Mechanics, 756, 89-109.

McCarren, H., Thomas, E., Hasegawa, T., Rhl, U., & Zachos, J. C. (2008). Depth dependency of the Paleocene-Eocene carbon isotope excursion: Paired benthic and terrestrial biomarker records (Ocean Drilling Program Leg 208, Walvis Ridge). Geochemistry, Geophysics, Geosystems, 9(10).

McIver, R.D., 1981, Gas hydrates, in Meyer, R.F., and Olson, J.C., eds., Long-Term Energy Resources: Boston, Pitman, p. 713-726.

Mekala, P., Babu, P., Sangwai, J. S., & Linga, P. (2014). Formation and dissociation kinetics of methane hydrates in seawater and silica sand. Energy & Fuels, 28(4), 2708-2716.

Milkov, A. V. (2004). Global estimates of hydrate-bound gas in marine sediments: how much is really out there?. Earth-Science Reviews, 66(3-4), 183-197.

Minagawa, H., Ohmura, R., Kamata, Y., Nagao, J., Ebinuma, T., Narita, H., & Masuda, Y. (2009). Water permeability of porous media containing methane hydrate as controlled by the methane-hydrate growth process.

Minshull, T. A., MarnMoreno, H., Armstrong McKay, D. I., & Wilson, P. A. (2016). Mechanistic insights into a hydrate contribution to the PaleoceneEocene carbon cycle perturbation from coupled thermohydraulic simulations. Geophysical Research Letters, 43(16), 8637-8644.

Mohr, S. H., Wang, J., Ellem, G., Ward, J., & Giurco, D. (2015). Projection of world fossil fuels by country. Fuel, 141, 120-135.

Moridis, G. J. (2002, January). Numerical studies of gas production from methane hydrates. In SPE Gas Technology Symposium. Society of Petroleum Engineers.

Moridis, G. J. (2008). Toward production from gas hydrates: current status, assessment of resources, and simulation-based evaluation of technology and potential. Lawrence Berkeley National Laboratory.

Moridis, G. J. (2012). TOUGH+ HYDRATE v1. 2 User's manual: a code for the simulation of system behavior in hydrate-bearing geologic media.

Moss, R. H., Edmonds, J. A., Hibbard, K. A., Manning, M. R., Rose, S. K., Van Vuuren, D. P., ... & Meehl, G. A. (2010). The next generation of scenarios for climate change research and assessment. Nature, 463(7282), 747.

Müller, P. J., & Suess, E. (1979). Productivity, sedimentation rate, and sedimentary organic matter in the oceansI. Organic carbon preservation. Deep Sea Research Part A. Oceanographic Research Papers, 26(12), 1347-1362.

Nakayama, T., Sato, T., Ogasawara, K., Kiyono, F., & Yamasaki, A. (2007, January). Estimation of Surface Area of Methane Hydrate in Sediments. In Seventh ISOPE Ocean Mining Symposium. International Society of Offshore and Polar Engineers.

Nazridoust, K., & Ahmadi, G. (2007). Computational modeling of methane hydrate dissociation in a sandstone core. Chemical engineering science, 62(22), 6155-6177.

Nixon, M. F., & Grozic, J. L. (2007). Submarine slope failure due to gas hydrate dissociation: a preliminary quantification. Canadian Geotechnical Journal, 44(3), 314-325.

Orr, F. M. (2007). Theory of gas injection processes. Copenhagen: Tie-Line Publications.

Petrenko, V. V., Smith, A. M., Brook, E. J., Lowe, D., Riedel, K., Brailsford, G., ... & Etheridge, D. (2009). 14CH4 measurements in Greenland ice: investigating last glacial termination CH4 sources. Science, 324(5926), 506-508.

Piñero, E., M. Marquardt, C. Hensen, M. Haeckel, and K. Wallmann (2013), Estimation of the global inventory of methane hydrates in marine sediments using transfer functions, Biogeosciences, 10(2), 959975, doi:10.5194/bg-10-959-2013.

Priest, J. A., Rees, E. V., & Clayton, C. R. (2009). Influence of gas hydrate morphology on the seismic velocities of sands. Journal of Geophysical Research: Solid Earth, 114(B11).

Priestley, J., Versuche und Beobachtungen Uber Verrshiedene Gattungen der Lufth, Th. 1-3, 3:359-362. Wien-Leipzig

Press, W. H. (2007). Numerical recipes 3rd edition: The art of scientific computing. Cambridge university press.

Pruess, K., Oldenburg C. M., Moridis, G. J. (1999). TOUGH2 user's guide version 2 (No. LBNL-43134). Ernest Orlando Lawrence Berkeley National Laboratory, Berkeley, CA (US).

Reagan, M. T., & Moridis, G. J. (2008). Dynamic response of oceanic hydrate deposits to ocean temperature change. Journal of Geophysical Research: Oceans, 113(C12).

Reagan, M. T., & Moridis, G. J. (2009). Large-scale simulation of methane hydrate dissociation along the West Spitsbergen Margin. Geophysical Research Letters, 36(23).

Reagan, M. T., Moridis, G. J., Elliott, S. M., & Maltrud, M. (2011). Contribution of oceanic gas hydrate dissociation to the formation of Arctic Ocean methane plumes. Journal of Geophysical Research: Oceans, 116(C9).

Riedel, M., Collett, T., Malone, M., Akiba, F., Blanc-Valleron, M., Ellis, M., ... & Holland, M. (2006). Gas hydrate transect across northern Cascadia margin. Eos, Transactions American Geophysical Union, 87(33), 325-332.

Ruan, X., Song, Y., Liang, H., Yang, M., & Dou, B. (2012a). Numerical simulation of the gas production behavior of hydrate dissociation by depressurization in hydrate-bearing porous medium. Energy & Fuels, 26(3), 1681-1694.

Ruan, X., Yang, M., Song, Y., Liang, H., & Li, Y. (2012b). Numerical studies of hydrate dissociation and gas production behavior in porous media during depressurization process. Journal of Natural Gas Chemistry, 21(4), 381-392.

Ruppel, C. (2007). Tapping methane hydrates for unconventional natural gas. Elements, 3(3), 193-199.

Ruppel, C. D. (2011). Methane hydrates and contemporary climate change. Nature Education Knowledge, 3(10), 29.

Ruppel, C. (2014). Permafrost-associated gas hydrate: is it really approximately 1% of the global system?. Journal of Chemical & Engineering Data, 60(2), 429-436.

Ruppel, C., J. D. Kessler., (2017) The Interaction of Climate Change and Methane Hydrates *Reviews of Geophysics, Vol 55*

Schiesser, W. E. (2012). The numerical method of lines: integration of partial differential equations. Elsevier.

Sapir, S. H., Beniaminovich, A. F., (1973). Messoyakha gas hydrate field. Geol Oil Gas 6, 26

Sarkar, S., Berndt, C., Minshull, T. A., Westbrook, G. K., Klaeschen, D., Masson, D. G., ... & Thatcher, K. E. (2012). Seismic evidence for shallow gasescape features associated with a retreating gas hydrate zone offshore west Svalbard. Journal of Geophysical Research: Solid Earth, 117(B9).

Selim, M. S., & Sloan, E. D. (1989). Heat and mass transfer during the dissociation of hydrates in porous media. AIChE journal, 35(6), 1049-1052.

Schäfer, M. (2006). Computational engineering: Introduction to numerical methods. Berlin: Springer.

Shakhova, N., Semiletov, I., Leifer, I., Sergienko, V., Salyuk, A., Kosmach, D., ... & Gustafsson, . (2014). Ebullition and storm-induced methane release from the East Siberian Arctic Shelf. Nature Geoscience, 7(1), 64.

Shafiee, S., E. Topal., (2009) When will fossil fuel reserves be diminished? *Energy Policy, Vol 37* 181-189

Sharqawy, M. H., Lienhard, J. H., & Zubair, S. M. (2010). Thermophysical properties of seawater: a review of existing correlations and data. Desalination and water Treatment, 16(1-3), 354-380.

Shampine, L. F., & Reichelt, M. W. (1997). The matlab ode suite. SIAM journal on scientific computing, 18(1), 1-22.

Shampine, L. F., Gladwell, I., & Thompson, S. (2003). Solving ODEs with matlab. Cambridge University Press.

Shields, G. A. (2008). Palaeoclimate: Marinoan meltdown. Nature Geoscience, 1(6), 351.

Shi, J. Q., Xue, Z., & Durucan, S. (2011). Supercritical CO2 core flooding and imbibition in Berea sandstoneCT imaging and numerical simulation. Energy Procedia, 4, 5001-5008.

Shin, H. (2014). Development of a Numerical Simulator for Methane-hydrate Production. Journal of the Korean Geotechnical Society, 30(9), 67-75.

Skarke, A., Ruppel, C., Kodis, M., Brothers, D., & Lobecker, E. (2014). Widespread methane leakage from the sea floor on the northern US Atlantic margin. Nature Geoscience, 7(9), 657.

Sloan Jr, E. D., & Koh, C. (2007). Clathrate hydrates of natural gases. CRC press.

Sohl, L. E., Christie-Blick, N., & Kent, D. V. (1999). Paleomagnetic polarity reversals in Marinoan (ca. 600 Ma) glacial deposits of Australia: implications for the duration of low-latitude glaciation in Neoproterozoic time. Geological Society of America Bulletin, 111(8), 1120-1139.

Song, Y., Wang, J., Liu, Y., & Zhao, J. (2016). Analysis of heat transfer influences on gas production from methane hydrates using a combined method. International Journal of Heat and Mass Transfer, 92, 766-773.

Sowers, T. (2006). Late quaternary atmospheric CH4 isotope record suggests marine clathrates are stable. Science, 311(5762), 838-840.

Spangenberg, E., Kulenkampff, J., Naumann, R., & Erzinger, J. (2005). Pore space hydrate formation in a glass bead sample from methane dissolved in water. Geophysical Research Letters, 32(24).

Stocker, T.F., D. Qin, G.-K. Plattner, M. Tignor, S.K. Allen, J. Boschung, A. Nauels, Y. Xia, V. Bex and P.M. Midgley. (2013). IPCC 2013: Climate Change 2013: The Physical Science Basis. Contribution of Working Group I to the Fifth Assessment Report of the Intergovernmental Panel on Climate Change, Cambridge University Press, Cambridge, United Kingdom and New York, NY, USA, 1535 pp.

Stone, H. L. (1970). Probability model for estimating three-phase relative permeability. Journal of Petroleum Technology, 22(02), 214-218.

Stranne, C., O'Regan, M., Dickens, G. R., Crill, P., Miller, C., Preto, P., & Jakobsson, M. (2016). Dynamic simulations of potential methane release from East Siberian continental slope sediments. Geochemistry, Geophysics, Geosystems, 17(3), 872-886.

Stranne, C., O'Regan, M., & Jakobsson, M. (2016). Overestimating climate warming-induced methane gas escape from the seafloor by neglecting multiphase flow dynamics. Geophysical Research Letters, 43(16), 8703-8712.

Sun, X., Nanchary, N., & Mohanty, K. K. (2005). 1-D modeling of hydrate depressurization in porous media. Transport in Porous Media, 58(3), 315-338.

Sun, X.,& Mohanty, K. K. (2006). Kinetic simulation of methane hydrate formation and dissociation in porous media. Chemical Engineering Science, 61(11), 3476-3495.

Sun, S., Liu, C., Ye, Y., & Liu, Y. (2014). Pore capillary pressure and saturation of methane hydrate bearing sediments. Acta Oceanologica Sinica, 33(10), 30-36.

Thatcher, K. E., Westbrook, G. K., Sarkar, S., & Minshull, T. A. (2013). Methane release from warminginduced hydrate dissociation in the West Svalbard continental margin: Timing, rates, and geological controls. Journal of Geophysical Research: Solid Earth, 118(1), 22-38.

Thomas, D. J., Zachos, J. C., Bralower, T. J., Thomas, E., & Bohaty, S. (2002). Warming the fuel for the fire: Evidence for the thermal dissociation of methane hydrate during the Paleocene-Eocene thermal maximum. Geology, 30(12), 1067-1070.

Tryggvason, G. (2011, Spring). The Equations Governing Fluid Motion. Retrieved on 02/03/2018 : http://www.nd.edu/g̃tryggava/CFD-Course/2011-Lecture-4.pdf

Tsypkin, G. G. (2007). Analytical solution of the nonlinear problem of gas hydrate dissociation in a formation. Fluid Dynamics, 42(5), 798-806.

Turner, D. J., Cherry, R. S., & Sloan, E. D. (2005). Sensitivity of methane hydrate phase equilibria to sediment pore size. Fluid Phase Equilibria, 228, 505-510.

Uchida, T., Ebinuma, T., Takeya, S., Nagao, J., & Narita, H. (2002). Effects of pore sizes on dissociation temperatures and pressures of methane, carbon dioxide, and propane hydrates in porous media. The journal of physical chemistry B, 106(4), 820-826.

Van Genuchten, M. T. (1980). A closed-form equation for predicting the hydraulic conductivity of unsaturated soils 1. Soil science society of America journal, 44(5), 892-898.

Vasiliev, V. G., Makogon, Y. F., Trebin, F. A., Trofimuk, A. A., Cherski, N. V. (1970) Ability of natural gases to exist in the Earth crust in the solid state. USSR Register of discoveries (Otkrytiia v SSSR 19681969)." Moscow Nauka 10 (1970): 3-5.

Vielstädte, L., Karstens, J., Haeckel, M., Schmidt, M., Linke, P., Reimann, S., ... & Wallmann, K. (2015). Quantification of methane emissions at abandoned gas wells in the Central North Sea. Marine and Petroleum Geology, 68, 848-860.

Waite, W. F., W. J. Winters., D. H. Mason., (2004) Methane hydrate formation in partially water-saturated Ottawa sand *Am. Mineral., Vol 89, (8-9)* 1202-1207

Wallmann, K., E. Piñero, E. Burwicz, M. Haeckel, C. Hensen, A. Dale, and L. Ruepke (2012), The global inventory of methane hydrate in marine sediments: A theoretical approach, Energies, 5(12), 24492498, doi:10.3390/en5072449.

Wang, Y., Feng, J. C., Li, X. S., Zhang, Y., & Li, G. (2016). Large scale experimental evaluation to methane hydrate dissociation below quadruple point in sandy sediment. Applied Energy, 162, 372-381.

Wiesenburg, D. A., & Guinasso Jr, N. L. (1979). Equilibrium solubilities of methane, carbon monoxide, and hydrogen in water and sea water. Journal of Chemical and Engineering Data, 24(4), 356-360.

Weinstein, A., Navarrete, L., Ruppel, C., Weber, T. C., Leonte, M., Kellermann, M. Y., ... & Kessler, J. D. (2016). Determining the flux of methane into Hudson Canyon at the edge of methane clathrate hydrate stability. Geochemistry, Geophysics, Geosystems, 17(10), 3882-3892.

Westbrook, G. K., Thatcher, K. E., Rohling, E. J., Piotrowski, A. M., Pälike, H., Osborne, A. H., ... & Hühnerbach, V. (2009). Escape of methane gas from the seabed along the West Spitsbergen continental margin. Geophysical Research Letters, 36(15).

Wouwer, A. V., Saucez, P., Schiesser, W. E., & Thompson, S. (2005). A MATLAB implementation of upwind finite differences and adaptive grids in the method of lines. Journal of computational and applied mathematics, 183(2), 245-258.

Wright, J. F., Dallimore, S. R., & Nixon, F. M. (1999). Influence of grain size and salinity on pressure-temperaure thresholds for metane hydrate stability in JAPEX/JNOC/GSC Mallik 2L-38 gas hydrate research-well sediment. In Scientific Results from JAPEX/JNOC/GSC Mallik 2L-38 Gas Hydrate Research Well, Mackenzie Delta, Northwest Territories, Canada, (ed.) S.R. Dallimore, T. Uchida, and T.S. Collett; Geological Survey of Canada, Bulletin 544, p. 229-240.

Xu, W., Lowell, R. P., & Peltzer, E. T. (2001). Effect of seafloor temperature and pressure variations on methane flux from a gas hydrate layer: Comparison between current and late Paleocene climate conditions. Journal of Geophysical Research: Solid Earth, 106(B11), 26413-26423.

Yamamoto, K., Terao, Y., Fujii, T., Ikawa, T., Seki, M., Matsuzawa, M., & Kanno, T. (2014, May). Operational overview of the first offshore production test of methane

hydrates in the Eastern Nankai Trough. In Offshore Technology Conference. Offshore Technology Conference.

Yousif, M. H., Abass, H. H., Selim, M. S., & Sloan, E. D. (1991). Experimental and theoretical investigation of methane-gas-hydrate dissociation in porous media. SPE reservoir Engineering, 6(01), 69-76.

Zachos, J. C., Bohaty, S. M., John, C. M., McCarren, H., Kelly, D. C., & Nielsen, T. (2007). The PalaeoceneEocene carbon isotope excursion: constraints from individual shell planktonic foraminifer records. Philosophical Transactions of the Royal Society of London A: Mathematical, Physical and Engineering Sciences, 365(1856), 1829-1842.

Zatsepina, O. Y., & Buffett, B. A. (1998). Thermodynamic conditions for the stability of gas hydrate in the seafloor. Journal of Geophysical Research: Solid Earth, 103(B10), 24127-24139.

Zarr, R.R., Chavez, J.A., Lee, A.Y., Dalton, G., Young, S.L., (2017). NIST Heat Transmission Properties of Insulating and Building Materials, NIST Standard Reference Database Number 81, National Institute of Standards and Technology, Gaithersburg MD, 20899 ¡http://srdata.nist.gov/Insulation/¿ (retrieved [16/ 06/2017]).

Zeebe, R. E., Ridgwell, A., & Zachos, J. C. (2016). Anthropogenic carbon release rate unprecedented during the past 66 million years. Nature Geoscience, 9(4), 325-329.

Zhao, J. F., Ye, C. C., Song, Y. C., Liu, W. G., Cheng, C. X., Liu, Y., ... & Ruan, X. K. (2012). Numerical simulation and analysis of water phase effect on methane hydrate dissociation by depressurization. Industrial & Engineering Chemistry Research, 51(7), 3108-3118.

Zhao, J., Shi, D., & Zhao, Y. (2012). Mathematical model and simulation of gas hydrate reservoir decomposition by depressurization. Oil & Gas Science and TechnologyRevue dIFP Energies nouvelles, 67(3), 379-385.

Zhao, J., Liu, D., Yang, M., & Song, Y. (2014). Analysis of heat transfer effects on gas production from methane hydrate by depressurization. International Journal of Heat and Mass Transfer, 77, 529-541.

Zhao, J., Wang, J., Liu, W., & Song, Y. (2015). Analysis of heat transfer effects on gas

production from methane hydrate by thermal stimulation. International Journal of Heat and Mass Transfer, 87, 145-150.

Zhao, J., Fan, Z., Dong, H., Yang, Z., & Song, Y. (2016). Influence of reservoir permeability on methane hydrate dissociation by depressurization. International Journal of Heat and Mass Transfer, 103, 265-276.